DESIGN, DEVELOPMENT, AND VALIDATION OF A NOVEL OPTICAL IMAGING DEVICE FOR BIOMEDICAL APPLICATIONS

By

ASHLEY CHRISTINE DACY

Presented to the Faculty of the Graduate School of

The University of Texas at Arlington in Partial Fulfillment

of the Requirements

for the Degree of

DOCTOR OF PHILOSOPHY

THE UNIVERSITY OF TEXAS AT ARLINGTON

August 2019

Acknowledgements

I would like to take this opportunity to thank the many people that contributed to my growth as a researcher and scientist at the University of Texas at Arlington. First, I would like to thank my dissertation committee, Dr. Kytai Nguyen, Dr. Ashwin Nair, Dr. Baohong Yuan, Dr. Jon Senkowsky, and Dr. Liping Tang, for their guidance over the course of this work. I would like to express my further sincerest thanks to my advisor, Dr. Liping Tang, for sharing his knowledge in biomedical engineering and for his expert direction in this work and others.

I would also like to thank all the members of the Regenerative Bioimaging Lab group. I extend thanks to Dr. Jun Zhou for his mentorship in my early work and invaluable guidance in matters of material science. I would also like to thank YiHui Huang for her assistance in performing animal studies. I thank Amir Hakamivala for his advice regarding cell culture and a variety of technical issues over the course of my graduate career. I am also very grateful to Joyita Roy for her assistance in gathering the data presented in Chapter 4 of this work.

Most importantly, I thank God and my family, whose unfailing support has made this and many other endeavors possible. I would especially like to thank my mother, Jennifer Roy, for her constant encouragement and my grandmother, Carol Vacker, for always being a source of inspiration in her boundless faith, love, and compassion. Děkuji, a Bůh vám žehnej.

July 18, 2019

Abstract

DESIGN, DEVELOPMENT, AND VALIDATION OF A NOVEL OPTICAL IMAGING DEVICE FOR BIOMEDICAL APPLICATIONS

Ashley C Dacy

The University of Texas at Arlington, 2019

Supervising Professor: Dr. Liping Tang

Fluorescence and luminescence imaging are two promising optical techniques for diagnosing a variety of critical pathologies *in vivo*, including wound healing, inflammation, and vascular diseases. Despite this, there is a lack of imaging devices in research and commercially available that are capable of these imaging modalities in large animal applications. This work describes the progressive development of several optical imaging devices to fill this void, culminating in a final design with robust fluorescence and luminescence functionality designed for large animal and human applications. These devices are used to gather new data about various physical parameters in small and large animal models. First, a portable imager developed for real-time imaging of cutaneous wounds in research settings is described. The device is demonstrated to have competitive performance with a commercial animal imaging enclosure box setup in beam uniformity and sensitivity. Specifically, the device was used to visualize the bioluminescence associated with increased reactive oxygen species (ROS) activity during the

wound healing process in a cutaneous wound inflammation model. In addition, this device was employed to observe the fluorescence associated with the activity of matrix metalloproteinases (MMPs) in a mouse lipopolysaccharide (LPS)-induced infection model. Our results support the use of the portable imager design as a non-invasive and real-time imaging tool to assess the extent of wound inflammation and infection.

The second component of this work details the development and characterization of a portable luminescence imaging device for detecting inflammatory responses and infection in skin wounds. This imager was used to quantify in real time the extent of 2D reactive oxygen species (ROS) activity distribution using a porcine wound infection model. The imager was used to successfully visualize ROS-associated luminescent activities *in vitro* and *in vivo*. Using a pig full-thickness cutaneous wound model, the luminescence imager was further demonstrated to be capable of detecting the change of ROS activities and their relationship with vasculature in the wound environment. Finally, by analyzing ROS intensity and distribution, an imaging method was developed to distinguish infected from uninfected wounds. These results demonstrate the potential discovery of a distinct ROS pattern between bacteria-infected and control wounds corresponding to the microvasculature.

The final piece of this work describes the design, manufacture, and testing of several fluorescence imagers improving on the design developed in the first part of this work, as well as the development of a penultimate combination

fluorescence/luminescence imaging device. This device is compared against a robust industry-standard device and found to be suitable for large animal and potential clinical applications.

Table of Contents

List of Figures

List of Tables

Abbreviated Summary

This work details the development and characterization of a portable luminescence imaging device for imaging fluorescent and luminescent signals in large animals. Several design iterations of this device are described, including the results of characterization, *in vitro*, and *in vivo* testing. These results were compared with a commercially available *in vivo* imaging device to test the competitiveness of the new imagers. The devices were shown to be competitive in *in vitro* fluorescence and luminescence studies. They also demonstrated excellent performance in both small and large animal studies, with a unique design allowing the collection of new information in large animal wound models. The final design was found to be capable of both fluorescence and luminescence imaging with equivalent or improved functionality when compared with a commercial imaging device, paving the way for this device to be utilized to gather important new information in future clinical applications.

Chapter 1. Background

1.1. Introduction

The development of new optical systems to take advantage of developments in the field of fluorescence and luminescence biomedical imaging is a critical need in modern medicine. This chapter will summarize the importance of biomedical engineering in the development of medical imaging techniques and modalities. In addition, the imaging principles, design considerations, and unique utility of fluorescence and luminescence imaging will be explored. The wide variety of fluorescent and luminescent imaging probes developed recently to gather detailed molecular information about various biomarkers and disease states are also examined here. An overview of currently available portable imaging devices able to image fluorescence and luminescence will also be provided, along with their applications, benefits, and drawbacks. This background forms the foundation of the goal of this work: The development of novel, portable fluorescence and luminescence imaging devices able to be used to gather new information in large animal and human disease models.

1.2. Medical Imaging

Bioengineering is a diverse field that includes the development of scaffolds and engineered tissues for tissue and organ regeneration, the design and testing of biomechanical implants, and the development of molecular reporting probes for visualizing various pathologies. The development and application of novel imaging methods for diagnosis of various diseases is a critical component of

bioengineering. Almost all pathologies in modern medicine are diagnosed with one or more imaging techniques. Optical imaging, including imaging of fluorescence and luminescence, are two imaging modalities within this category that are notable for the simplicity of their instrumentation, versatility, and low cost. Despite this, there is a lack of accessible fluorescence and luminescence imaging devices for research and translational medical imaging.

1.3. Fluorescence and Luminescence in Biomedical Imaging

Over the past three decades, near-infrared (NIR) optical imaging has become a promising approach for non-invasive tissue characterization and imaging. NIR light between 750 - 900 nm is minimally absorbed and preferentially scattered, allowing deep tissue propagation.[1] NIR optical imaging technology has the ability to differentiate diseased tissues from healthy tissues on a molecular level, as well as the potential to provide complementary information to current clinical imaging techniques without harmful radiation, radioactive substances, or ungainly instrumentation.[2] Near-infrared spectroscopy and imaging (NIRS) techniques have used near-infrared light between 650 and 950 nm to non-invasively sense the concentration and oxygenation of hemoglobin in the brain, muscle and other tissues. A single NIRS measurement is sensitive to a volume of tissue that falls between the source of light entering the tissue and the detector receiving the light that diffuses out of the tissue. Near-infrared spectroscopy is possible with portable, inexpensive devices.

Luminescence refers to light emitted spontaneously through any of several processes, including chemical reactions and biological processes. Since this imaging modality relies on photons generated without an excitation light source, luminescence imaging equipment requires robust isolation from ambient light that could be interpreted by the camera as signal. The tissue depth at which this modality can be used is wavelength-dependent, with luminescent probes emitting higher-wavelength photons having higher penetration depth in tissue.[3] Luminescence imaging devices also have the potential to be extremely compact due to their lack of necessity for several components required for fluorescence imaging, such as excitation light sources and optical filters.

1.4. Fluorescent and Luminescent Probes for the Visualization of Molecular Markers of Various Pathologies

Many fluorescent imaging probes have been developed that allow molecular markers of many biological processes, including inflammatory reactions, cancer detection, and wound healing.[4,5] Genetic fluorescent tags have also been used to great effect. Fluorescence imaging has a strong precedent in wound healing research. In 2012, green fluorescent protein (GFP)-tagged mesenchymal stem cells (MSCs) were tracked using a commercial *in vivo* fluorescence imaging system in a murine burn wound model. MSCs were established to migrate to the wound bed over the course of 28 days, accumulating primarily at the edges of the wound.[6] Wound oxygenation in diabetic foot ulcers has been monitored over time using NIRS.[7] Additionally, a handheld NIRS scanning device has used 710 nm

wavelength light to use absorption contrast to differentiate between healing and chronic diabetic foot ulcers.[8]

Several biomaterials and imaging probes have been developed to detect molecular markers of various pathologies using luminescence *in vivo*.[9,10] However, the sensitivity and specificity of these materials/probes for ROS detection is limited. Our and other groups have shown that Lucigenin, luminol, and luminescent L-012 are prominent examples of luminescent ROS probes that have been used *in vivo*.[11] luminescent L-012 in particular is well-regarded for its high sensitivity and luminescent output.[12] Our group has previously used luminescent L-012 to detect inflammatory-response-associated ROS activity in acute mouse wounds over time.[13] In addition, luminescence imaging has been used for noninvasive detection of a wide variety of biomolecular parameters, including peroxynitrite, pH, and reactive nitrogen species.[14–16] MSCs expressing the luminescent tag firefly luciferase (Fluc) have been used to visualize MSC migration to wound sites *in vivo* over time with high resolution.[17] pH gradients in wound tissue have been visualized using the luminescent probe FITC conjugated to a sensor film.[15] Ratiometric luminescence imaging has also been used to correlate both pH and oxygen partial pressure distribution in diabetic ulcers to differentiate between healing and chronic wounds using the pH-sensitive luminescent probe FITC and the oxygen-sensing probe Pt-TPFPP.[18] Several probes have also been developed that luminesce upon contact with markers of wound healing, such as changing pH.[19,20] Luminescence can also be utilized to

visualize bioluminescence, such as that of the common bacteria *E. coli,* in applications studying biofilms and infection.[21] Despite luminescence imaging's strong precedence in biomedical research, there are currently no portable imagers described in research or on the market capable of performing luminescence imaging on large animals or human subjects.

1.5. Existing Portable Imaging Devices

To translate recent imaging probe technology advancements into clinical diagnosis potential, there is a need for portable imaging systems which can detect both luminescent and fluorescent signals *in vivo*. Although several optical imagers with this capacity are commercially available,[19] such devices are designed as large enclosed units for small animal research and cannot be used for large animals or human subjects. Several portable imager prototypes have been developed with the capability to visualize wounds. Several targets have been utilized.[22] For example, skin wounds in diabetic rats have been characterized using a simple fNIR (functional near-infrared spectroscopic) device consisting of a Teflon laser probe with one source and four detector fibers and diffuse optical tomography (DOT).[18,23] However, the relatively poor resolution that results from the high degree of light scatter in biological tissue limits their application.[24] An inexpensive camera with a polarizing filter was tested for the determination of wound area in 2010.[25] In 2011, an imaging device capable of measuring partial pressure of oxygen and pH in a 2D image was fabricated using a digital single-lens reflex (DSLR) camera and a 405 nm LED light source.[26] While these devices

are portable and easy to use, they lack the ability to visualize fluorescent signals due to the lack of proper light sources and emission filters. Therefore, there remains a need for low-cost portable imaging devices to visualize wide ranges of fluorescent and luminescent signals.

1.6. Overview of Work

To address these insufficiencies and the need for early diagnosis options in wound healing, infection, inflammation, and other common clinically relevant applications, the goal of the proposed work is to develop a portable, versatile fluorescence/luminescence imaging device for visualization of skin wounds, vascularization, and other pathologies in research and possible clinical translational applications.

In Chapter 2, I discuss the development of a compact tabletop fluorescence/luminescence imaging device and its validation *in vitro* and against an industry-standard optical imaging device. The devices are also compared in several small animal models, including models of wound healing and inflammation. Part of this work has been published previously.[27]

In Chapter 3, the device developed in Chapter 2 is further developed into a dedicated luminescence imaging device designed for large animal imaging. This device is tested *in vitro* to validate its functionality. It is also tested in small and large animal models, including a model of murine wound healing and a swine wound healing and infection study. Novel information is gathered with this new

device about the relationship between wound healing, vascularization, ROS gradients, and infection.

Chapter 4 of this work describes the development of the device presented in Chapter 2 into subsequently more sophisticated fluorescence imaging devices, culminating in the development of a first-of-its kind device capable of imaging in large animal and clinical scenarios. This device is tested and compared with an industry-standard device in a wide battery of key *in vitro* studies, displaying its potential to collect new information in future large animal and clinical applications. Part of the results listed in Chapter 3 and 4 are included in a pending publication.[28]

Chapter 2. Development and Validation of a Tabletop *in Vivo* Fluorescence/Luminescence Imaging Device

2.1 Introduction

2.1.1. Portable Imager Application Highlight: Wound Healing

Wound care represents one of the fastest-growing segments of the modern healthcare market.[29] In the United States, chronic wounds are estimated to cost $20 billion and affect over 6.5 million patients per year.[30] Chronic, non-healing wounds present complex treatment and diagnostic difficulties. It is well-established that inflammatory products, including reactive oxygen species (ROS), have critical influence over the healing process.[31–33] However, traditional wound healing measurements rely on wound size and volume measurements which have been found to have poor accuracy.[34,35] On the other hand, wound bacterial infection and infiltration (also called as bioburden) are well-established to delay wound healing[36] and wound infection diagnosis (typically via a swab culture) is time-consuming and requires access to a specialized facility.[37,38]

2.1.2. Wound Imaging Techniques

Cutaneous wounds represent a major segment of the medical imaging market, with a focus on distinguishing between acute and chronic wounds.[39] In a clinical setting, wounds have traditionally been monitored using low-tech methods, such as measurement of wound dimensions and clinician observation of changes in color, exudate, and patient pain levels.[34] Reliance on these qualitative techniques can lead to suboptimal treatment plans and poor patient outcomes.[35,40]

A wide range of techniques has been applied to gather more information about wound status. These include analysis of parameters such as wound color and dimensions using optical imaging.[35,41] These techniques provide a way to quantify visual parameters with greater precision than traditional methods. However, they provide no information about specific biological processes. Thermal imaging has been used to add thermal information in conjunction with these techniques to predict ulcer healing status.[42] Laser Doppler imaging has been used to monitor wound tissue blood perfusion, but does not provide biochemical information.[43,44] Hyperspectral imaging is capable of producing a 3-dimensional hypercube that provides information about how tissue interacts with many wavelengths of light. It has been utilized to collect information about wounds such as correlation of cell number and hemoglobin concentrations with wound healing status, but requires expensive instrumentation and cannot provide important molecular information.[45,46,47] Optical coherence tomography (OCT) uses backscattered light to generate cross-sectional images of tissue with a resolution of 1-15 μm. It has been used to characterize wound depth and microstructure change over time, but does not provide direct information about biological activities.[48,49] These imaging methods provide a depth of information about the status of a healing wound that is not accessible with lower-tech methods. However, there is a lack of techniques that provide detailed information about critical markers of the biochemical environment of a wound in a time-resolved, portable, and inexpensive manner.

2.1.3. Objectives of This Work

In this chapter I present the development of a portable imaging system which incorporates fluorescence and luminescence imaging modalities for real-time imaging. The portable imaging system is composed of a CCD camera, LED ring light source, and emission filters similar to many commercial systems.[20,26] To optimize portability, this device integrates all components into a small "black box" setup with interchangeable LED rings for different excitation wavelengths, eliminating the need for excitation filters. The LED ring makes the system compact without sacrificing performance. A rotatable filter wheel allows the selection of different emission wavelengths with ease for varying situations. The device is compact and portable, allowing easy transportation to different sites in a research setting. All necessary components are integrated into an easy-to-use external camera attachment. The entire system can be electronically controlled except the filter wheel, which has a manually controllable section accessible from outside the box. The versatility of this mount-and-play device permits its use for animal research and also displays potential for human wound diagnosis.

2.1. Design Objectives and Criteria

Due to the high efficiency of this optical approach and the robust principle of monitoring *in vivo* inflammatory responses using pH-sensing ratiometric fluorescence imaging probes, the *in vivo* imaging system was designed to be compact and portable. Table 2.1 shows the requirements and specifications for the

imaging system and their equivalence to the commercially available Kodak FX Pro.

Table 2.1. Comparison of the specifications of the Portable Imager and a Kodak In Vivo FX Pro imaging system.

	Specification	Portable Imager	Kodak In Vivo FX Pro
Detector	Pixel Size	5 ~ 10 µm	7.4 µm
	Dynamic Range	16 bit	16 bit
	Dark Current	< 0.001 e/pixel/s	0.003 e/pixel/s
	Read Noise	< 10 electrons (rms)	< 9 rms
Light Source	Type	LED	Xenon bulb
	Wavelengths	630nm or 740 nm	410 - 760 nm (excitation) 535 - 830 nm (emission)
Filter	Type	Thin-film coating	Thin-film coatings
	Transmission	> 60%	> 60%
Zoom Lens	Angle of View	> 28°	33°
Dimensions	Size (L xW xH)	22 x 22 x 25 cm	104 x 61 x 96.5 cm
	Weight	5.8 kg	142 kg

The imager has four major components, including a CCD camera, filter wheel, LED rings, computer and LED driver (Figure 2.1).

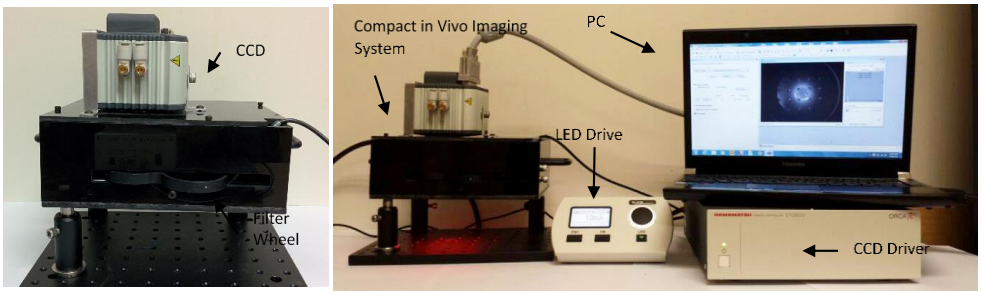

Figure 2.1. Near-infrared wound imager setup, including the CCD, rotating filter wheel, LED driver, and PC running WoundView™ software.

The system is covered by a black plastic box with a window in the user-facing side of to access a manually controlled filter wheel. This allows emission filters to be changed without disturbing the measurement process. The electronically controlled LED ring also allows the intensity of the excitation light to be changed with an external dial.

An LED ring was chosen as the light source, a circular array of LEDs with an empty interior. This allows the system to be completely vertical, since the light is first produced from the LED ring downwards to the objective, then emitted back up through its center to be collected by the CCD camera. Due to the divergence angle of LEDs, the LED ring can give uniform light over a short range of distances. However, this limits the selection of different light wavelengths. Thus, this device uses manually exchangeable single wavelength excitation. The portable imager setup and a schematic of its light path is compared with the light path of a commercial black-box imager in Figure 2.2.

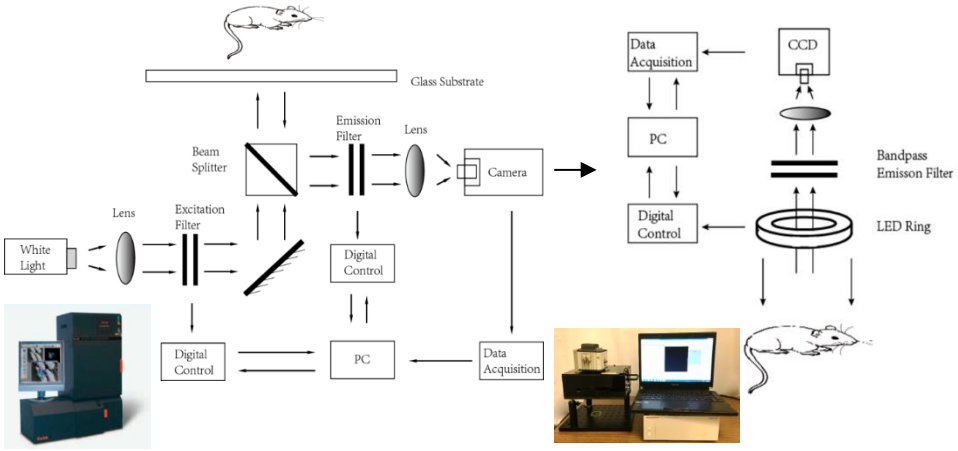

Figure 2.2. Simplified light path of the proposed in vivo imager design compared with the Kodak FX Pro.

The excitation light passes through the center opening of the LED ring and is collected by the CCD camera through a bandpass filter. A manually controlled filter wheel is incorporated to exchange bandpass filters to remove light outside the emission spectrum of the fluorophore from the light path. The complete optical imaging system is mounted inside a black polycarbonate casing which can efficiently block ambient light. White light images were generated by taking images through a blank filter wheel slot with excitation by ambient room lighting. This was found to produce clear and high-resolution images. For luminescence studies, the light source can be turned off with the filter wheel set to an empty position to detect spontaneously emitted bio- or chemiluminescence. The combination of the LED ring and bandpass filter wheel exchange system allows the device to be much smaller than the majority of commercial *in vivo* imaging devices.

2.2. Image Processing Software

An in-house image processing software platform (WoundView™) allows the user to make manual, semi-automatic, or fully automatic regions of interest (ROIs). WoundView™ generates statistical information from the ROIs and allows the user to superimpose up to three images at a time. For studies involving multiple time points, this allows images to be overlaid and ROIs to be automatically extrapolated to place ROIs over the same area measured in the initial ROI. The manual ROI generation tool allows the user to draw freehand or use an adjustable ellipse. The semi-automatic tool allows the user to adjust an intensity threshold within the ROI. The fully automatic tool allows the user to select an intensity hotspot of interest based on which the algorithm will generate a ROI from a user specified iso-intensity level. WoundView™ utilizes a Matlab- (Mathworks, Inc.) based interface with object-oriented C++ wrapped functions (Microsoft Visual Studios) for computational efficiency. Figure 2.3 shows a representative background white light image with a superimposed intensity image using the generated ROIs.

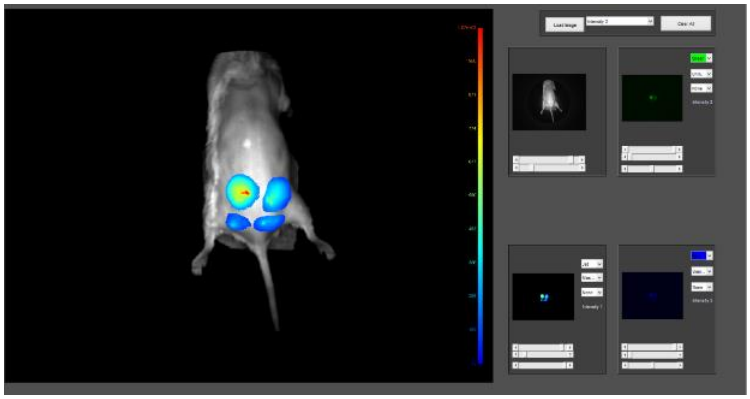

Figure 2.3. WoundView™ working environment with four different semi-automatic ROIs superimposed on a white light image. Iso-intensity lines are displayed ranging from blue (10% maximum intensity) to red (90% maximum intensity).

ROIs for the areas of interest were manually selected using a freeform drawing tool. The same threshold (70%) was applied for each ROI. Average intensities were calculated for each ROI using WoundView™ software. Three ROIs were measured to give each average and their standard deviations.

2.3. Materials and Methods

2.3.1. Materials

An ORCA-R2 CCD camera (C10600) was obtained from Hamamatsu. A 5 mm focal length f/1.4 lens (MVL5M23), a LED driver (DCZ100), and a 60 mm cage system filter wheel (LCFW5) were obtained from Thorlabs. Two-inch diameter thin-film 700±2 nm and 810±2 nm near-infrared filters (67-905, 67-916) were obtained from Edmund Optics. A 630±10 nm and a 740±10 nm LED ring light were obtained from ProPhotonix (RF2-630-VXF100). The portable imager housing was constructed using in-house laser-cut 5 mm thickness black polycarbonate.

2.3.2 Device Characterization

In order to demonstrate the efficacy of the proposed imaging setup, a commercial product (Kodak i*n vivo* FX Pro) and a spot-LED excitation model was chosen to compare with the final one-wavelength LED ring excitation design to determine feasibility. A diagram of the spot-LED excitation setup is shown in Figure 2.4.

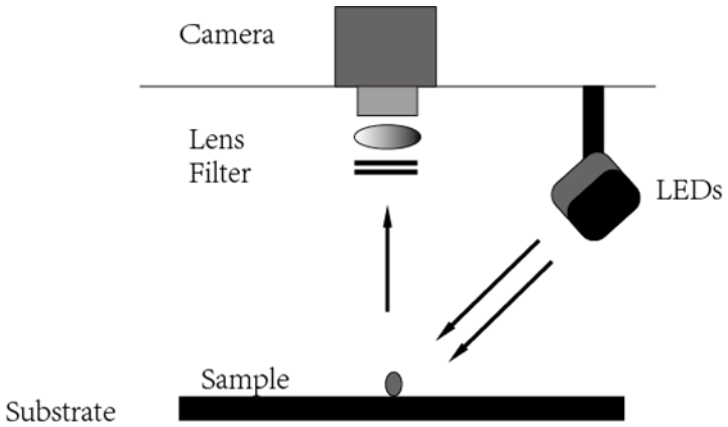

Figure 2.4. Schematic illustrating the spot LED excitation setup.

2.3.3.1. Beam Uniformity Comparison

Light uniformity plays a vital role in imaging systems. If the light is not uniform, signal at different positions in the field of view may vary due to lack of excitation light uniformity instead of signal variation. Beam uniformity was compared for all three imaging systems.[26] White paper was used as the test medium. Light sources were operated at 630 nm and light was kept consistent at 22.5 μW/cm^2.

2.3.3.2. Working Distance

Optimal working distance was determined by taking beam uniformity measurements at increasing distances. LED rings have divergence angles that alter uniformity with distance, making it necessary to calibrate the optimal

working distance. Working distance here is defined as the length from the sample surface to the base of the lens attachment. The manufacturer's recommended working distance of the selected LED ring is 4 cm. To confirm this, distances from 3 to 6 cm were analyzed. A 640 nm LED ring light was illuminated and shone onto the paper at these distances. The most uniform distance was defined as the distance with the widest area of illumination with a uniformity greater than 0.9. Uniformity index is defined here in Equation 2.1.[50]

Equation 2.1

$$Uniformity = \frac{Average\ Intensity}{Max\ Intensity}$$

The uniformity indices were calculated using average intensities at increasing radial distances. Three images were acquired, and the averages and standard deviations were calculated. An unpaired two-tailed student's t-test was used to test for significant differences in uniformity at each distance. We hypothesized that the LED ring will have a uniform imaging area of 2 x 2 cm and a working distance of 4 cm according to the manufacturer's claims.

2.3.3.3. Beam Intensity

Light source intensity was measured using a thermal power meter. The intensity of the newly designed imager was compared with the intensity of the Kodak. Light sources were operated at 640 nm and maximum power with the thermal power meter sensor placed directly in the center of the device. We hypothesized that the new imager would produce a higher maximum light intensity due to the direct nature of its illumination compared to the diffusivity of the Kodak.

2.3.3. In Vitro Models

2.3.3.1: Fluorescence Sensitivity and Limit of Detection: Cy5 Calibration Curve

The relationship between dye concentration and fluorescent intensity was compared between the portable imager and the Kodak imaging system using a calibration curve technique as previously described.[51] Six concentrations of NIR Cy5 dye (131.26, 65.6, 32.8, 16.4, 8.2, and 4.1 μM, three replicates, 200μL/each) were excited with 630 nm light. The averages and standard deviations of fluorescent intensities from both imagers were quantified. The limit of detection and sensitivity of the imager were compared with a commercial black-box imager (Kodak In Vivo Pro). Limit of detection (LOD) was defined as the lowest concentration of the specific dye being tested each machine is capable of detecting and was calculated using Equation 2.2.[52]

Equation 2.2

$$LOD = \frac{3\sigma}{k}$$

Where σ = the standard deviation of the control and κ = the slope of the linear curve.

Sensitivity was defined as the change in intensity units corresponding to one unit of concentration change for the specific dye in question. Sensitivity was determined by the slope of the linear line of best fit (LOBF) of the standard curve, as previously defined.[53,54] Strength of correlation was determined by calculating the coefficient of determination (R^2). Statistical differences between the two imagers were determined with a paired 2-way Student's t-test, with differences

deemed significant when $P \leq 0.05$.[55] We predicted that the new imager would have similar limit of detection and sensitivity to the Kodak imager.

2.3.3.2. Luminescence Sensitivity and Limit of Detection: L-012 Calibration Curve

A calibration curve was used to determine if the portable imager can detect ROS *in vitro*.[56] The luminescent, ROS-sensitive probe L-012 was used with the ROS-producing compound H_2O_2 as described in literature.[12] Twenty μL of luminescent L-012 (15 mg/mL) was mixed with 200 μL of H_2O_2 in aqueous solution (0 to 0.5 mM) in the wells of a 96-well plate in triplicate for each concentration. Luminescence intensities were recorded using the portable imager with an exposure time of 20 min. This study was repeated with the Kodak imager for comparison. Statistical analyses were carried out as described in Section 2.3.3.1. We predicted an increasing intensity with ROS concentration, as shown in previous studies.[56] It was also predicted that the portable imager would have a similar limit of detection and sensitivity to the portable imager.

2.3.4. In Vivo Models

2.3.4.1. In Vivo *Cy5 Calibration Curve*

To determine the ability of the portable imaging device to visualize fluorescent signals in *in vivo* applications, a subcutaneous dye injection model was used similar to a previously described method.[57] Four concentrations of the NIR dye Cy5 dispersed in sterile PBS was injected under the skin of the dorsal area of a mouse (7.50, 3.75, 1.88, and 0.94 mM). An untreated area of skin was used as a

control. Intensity and dye concentration were correlated, and averages and standard deviations were calculated. Sensitivity and resolution were compared between the portable imager and Kodak. Statistical analysis was carried out as described in Section 2.3.3.1. We predicted that the novel imaging device would be capable of detecting changes in concentration *in vivo* with similar sensitivity to the Kodak. All animal models were approved by the University of Texas at Arlington Institutional Animal Care and Use Committee (IACUC).

2.3.4.2. Murine Subcutaneous Infection Model

The utility of the portable imaging device in a murine model of subcutaneous infection was investigated. The bacterial toxin lipopolysaccharide (LPS) was injected under the skin in the dorsal area of mice as previously described.[27] Twenty μL of LPS (3.61 mM) or PBS buffer (50 mM, control) mixed with 100 μL of 2 nM MMP-sensitive NIR fluorescent probe MMPSense750 FAST was injected subcutaneously on the dorsal area of mice. Thirty minutes after injection, fluorescent images of the animals were taken with a 740-nm LED ring and 810-nm emission filter with an exposure time of 20 s under isoflurane anesthesia. Averages and standard deviations were calculated for each group with n number of animals based on the results of a power analysis with 85% power as described previously.[58] Statistical significance of difference between LPS-treated skin and control areas were determined with an unpaired one-tailed t-test. We predicted that the portable imager would be able to detect a significantly higher MMP-

associated fluorescence for LPS- vs. PBS-treated areas as suggested in previous literature.[59,60]

2.3.4.3. Murine Wound Healing Model

To confirm the ability of the device to detect luminescence *in vivo*, a mouse excisional wound model was used.[61] The luminescent probe L-012 was be used to detect ROS-associated luminescence in wounds of different ages.[62] One full-thickness excisional wound was created on the first day of the study. On Day 6 of the study, a second wound was created. Ten μL of 15 mg/mL luminescent L-012 was then applied to each wound, with healthy skin acting as a control. The difference between wounds of different ages was examined by imaging with the portable imaging device for 20 minutes. Statistical analyses were carried out as described in Section 2.3.4.2. It was hypothesized that the portable imaging device would successfully correlate significantly higher ROS-associated luminescent signal with acute inflammatory phase (Day 1) wounds than older wounds and healthy skin.[33]

2.4. Results

2.4.1. Device Characterization

2.4.1.1. Beam Uniformity Comparison

Beam uniformity was compared for the 625nm spot LED, 630nm LED ring, and white light 175W Xenon bulb in the Kodak imager. White paper was used as the test medium and light beams were characterized when they arrived at the samples. To compare two systems, the experimental conditions were kept consistent with a

maximum light intensity of 22.5 μW/cm^2 (determined using a thermal power meter). The relative light intensity to the maximal light intensity was calculated and present as normalized intensities of the spot LED (Fig. 2.5a), LED ring (Figure 2.5b), and Xenon bulb (Figure 2.5c).

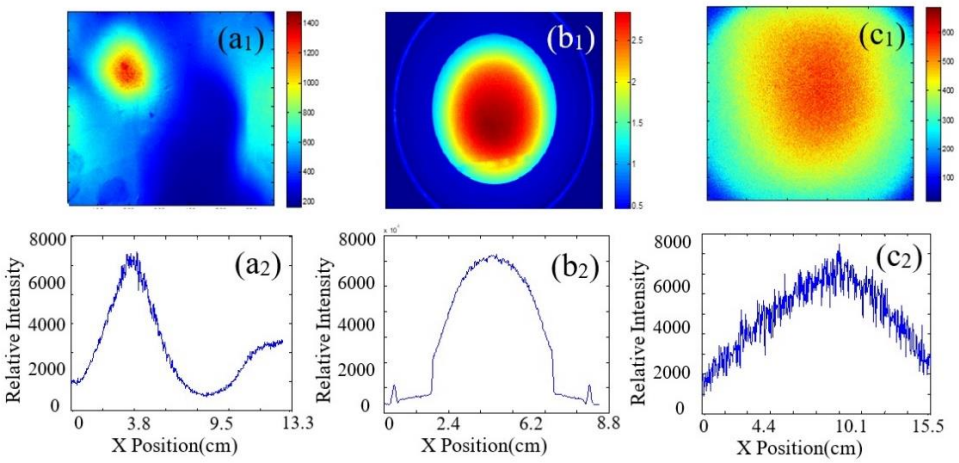

Figure 2.5. Beam uniformity was compared for spot LED excitation (an), LED ring excitation (bn), and xenon blub illumination (cn). The spot LED demonstrates poor beam uniformity, while the Kodak displays excellent uniformity. The LED ring model displays a good combination of beam uniformity and low noise.

For the spot LED, the incident angle and position focus the beam to a small point. This limits the effective area and reduces the uniformity of the field of view. Due to this, the spot LED was discounted for use in further studies due to its inherently poor uniformity. The LED ring forms an almost perfect circular area with a more uniform beam. A comparison of homogeneous view areas is shown in Figure 2.6.

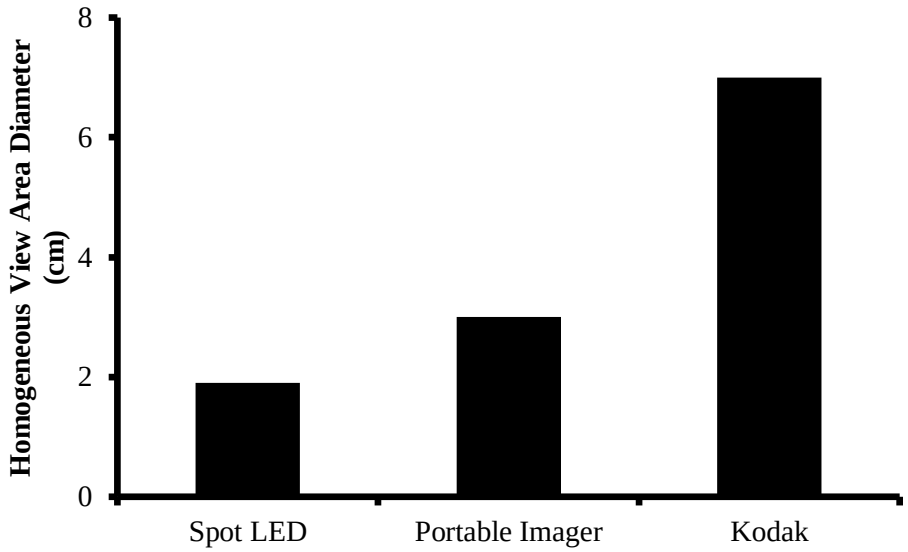

Figure 2.6. A comparison of homogeneous view areas for all imagers is shown. The spot LED was disregarded for its low homogeneity, while the portable imager and Kodak had practical circular view areas at 80% homogeneity with diameters of 3 and 7 cm respectively.

The spot LED was found to have a uniform beam area of 1.9 cm. The portable imager was found to be capable of illuminating a view area with a diameter of 3 cm while maintaining 80% beam uniformity. The Kodak's beam uniformity is the largest of the three, with an 80% homogeneous view area with a diameter of 7 cm. However, this also comes with the addition of significant noise.

While the smaller detection area of the portable imager could restrict the potential of application on large wounds diagnosis, the portable and open design could allow for diagnosis of larger areas. Holding the device to scan large surface areas from different angles could also provide better accuracy and flexibility in clinical practice. Although confined, bulky devices represented by the Kodak are able to observe large areas, they are also limited practically in their use on

patients. However, increasing the view area of the device remained a primary goal for the rest of this work.

2.4.1.2. Working Distance

The individual LEDs that make up the LED ring light source have divergence angles that alter uniformity with distance, making it necessary to calibrate the optimal working distance. Working distance was defined as the length from the sample surface to bottom surface of the device casing. This value has the capacity to be easily adjusted for various applications.

The manufacturer's recommended working distance of the LED ring is 4 cm. After calibration (Figure 2.7), 4 - 5 cm was determined to give the most uniform light. The field of view is 8.8 cm (W) x 8.8 cm (L), and the beam size above 80% of peak value part is 2.8 cm (W) x 3.5 cm (L). Uniformity here is defined as light greater than or equal to 80%.

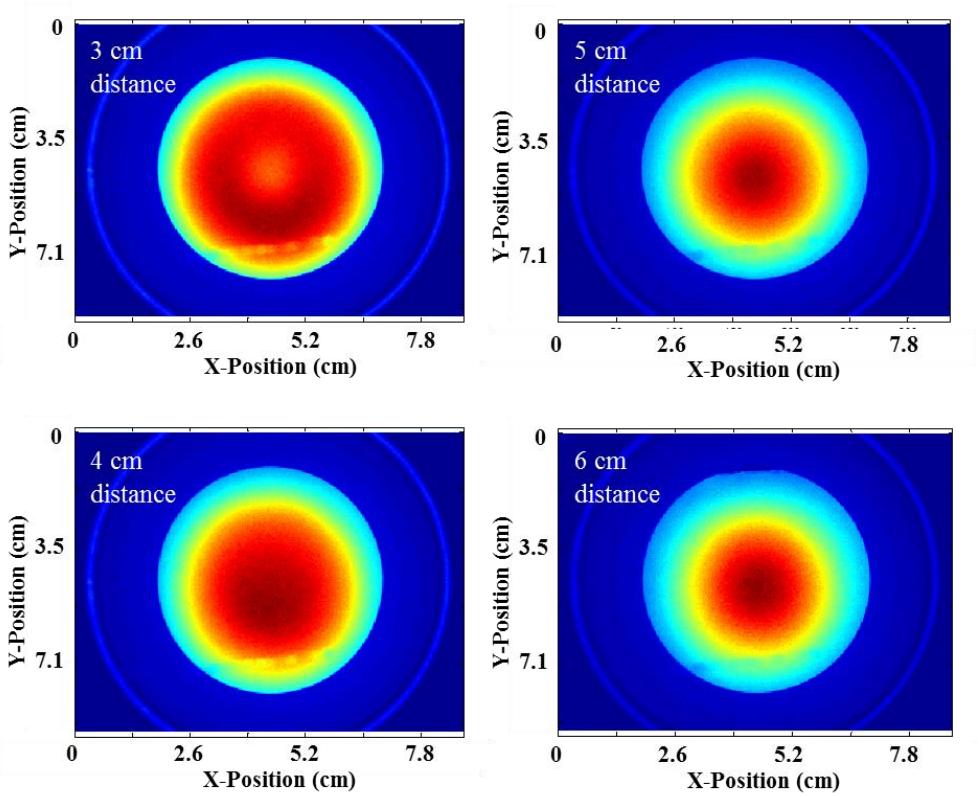

Figure 2.7. Working distance of the portable imager was calibrated by comparing beam uniformity at different distances (3, 4, 5 and 6 cm). Optimal beam uniformity was obtained at 4 cm.

For a working distance of 3 cm, the intensity of light at the center is much weaker than edge, which means the beams from each LED do not overlap in the center. But for 4, 5 and 6 cm, the intensity of light at the center is a stronger than at the edge, where it decreases with distance. Based on the homogeneity of the light intensity, 4 cm was chosen as the optimal working distance.

2.4.1.3. Beam Intensity

Maximum light intensity was determined using a thermal power meter. The 640 nm LED ring light source was compared with the Kodak's Xenon bulb fitted with a 640 nm emission filter (Figure 2.8).

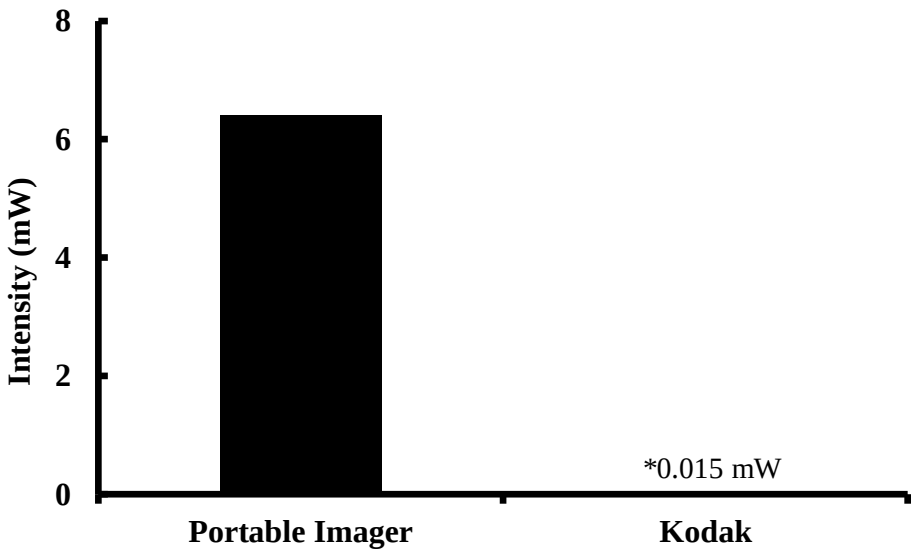

Figure 2.8. Maximum intensities for the portable imager and Kodak imaging system were compared at 640 nm. The portable imager's LED ring was found to have an intensity approximately 400 times higher than the Kodak.

The LED ring was found to achieve intensities up to 6.4 mW, almost 430 times higher than the Kodak machine's maximum of 0.15 mW. This allows for much shorter exposure times, which is especially critical for *in vivo* studies in a laboratory environment.

2.4.2. In Vitro Models

2.4.2.1. Fluorescence Sensitivity and Limit of Detection: Cy5 Calibration Curve

The relationship between dye concentrations and fluorescent intensity was determined and compared between the portable imager and a Kodak imaging system. Specifically, five concentrations of NIR Cy5 dye (65.6, 32.8, 16.4, 8.2, 4.1, and 0 μM) were excited with 640 nm light. The fluorescent intensities were quantified using both imagers and then statistically analyzed. In general, the

relative intensity values for the portable imager were found to be lower than for the Kodak system (Figure 2.9).

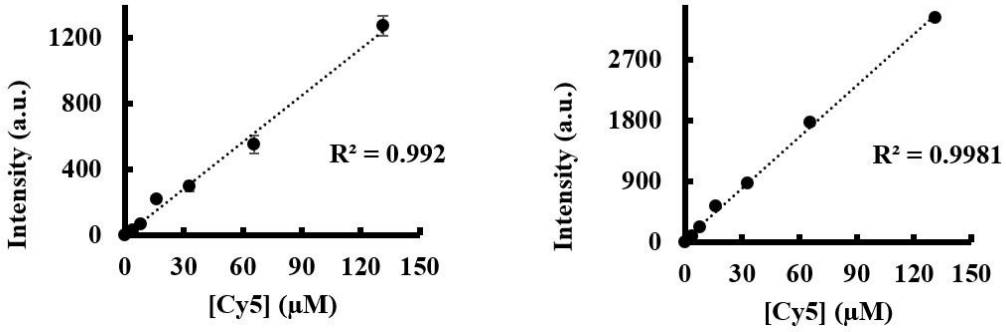

Figure 2.9. Concentrations of NIR Cy5 dye were correlated with fluorescent intensities with excitation wavelength of 630 nm using both (left) the portable imager and (right) the Kodak system.

However, both systems show excellent linear relationships between dye concentrations and fluorescent intensity. In addition, sensitivities for both imagers were comparable, with the portable imager producing a sensitivity of 9.5 ± 0.4 $\frac{a.u.}{\mu M}$ and the Kodak measuring 25.4 ± 0.6 $\frac{a.u.}{\mu M}$. Although this difference is non-trivial, accounting for the difference in camera bit depth between the two devices clarifies the reason for the discrepancy. The Kodak has a 16-bit camera, which translates to a maximum number of gray values of 65,535 compared to the portable imager's 4,095 for its 12-bit camera. To assess the extent of this parameter on the sensitivity difference, the data was normalized to 12-bit for both imagers and reanalyzed (Figure 2.10).

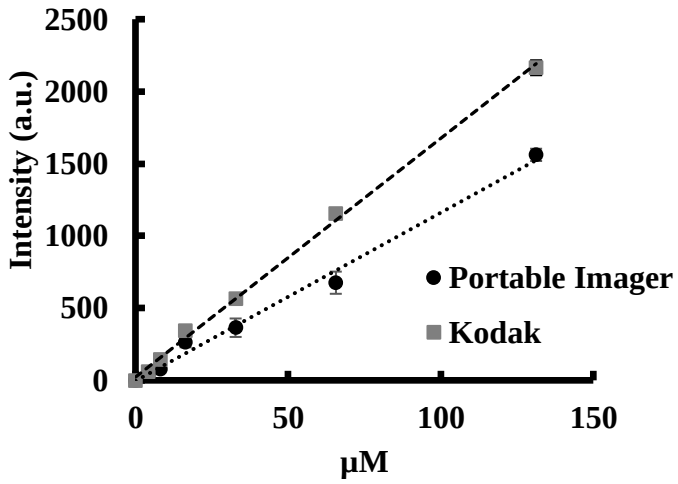

Figure 2.10. NIR Cy5 calibration curve normalized to 12-bit values for both imagers. This transformation indicates that the majority of sensitivity difference is due to the difference in the cameras' bit depths and can be accounted for by normalization for more accurate comparison.

Upon normalization of the intensity values, the sensitivities of the two imagers become 11.65 ± 0.33 $\frac{a.u.}{\mu M}$ for the portable imager and 16.53 ± 0.92 $\frac{a.u.}{\mu M}$. This analysis displays that approximately 50% of the difference in fluorescence sensitivity between the two imagers is due to the difference in bit depth between the two cameras.

The two devices were also found to have similar limits of detection, with the portable imager able to detect NIR Cy5 concentrations as low as 3 µM compared to the Kodak's 2.7 µM. These results support that both imagers are capable of measuring and quantifying fluorescent intensities *in vitro*.

2.4.2.2. Luminescence Sensitivity and Limit of Detection: L-012 Calibration Curve

To test the response of the new device to luminescent signals, a standard curve for the ROS-sensitive probe luminescent L-012 was constructed. Twenty μL of luminescent L-012 (15 mg/mL) was mixed with 200 μL of H_2O_2 in aqueous solution (0 to 0.5 mM) in the wells of a 96-well plate in triplicate for each concentration. Luminescence intensities were recorded using the portable imager with an exposure time of 20 min. This study was repeated with the Kodak imager for comparison (Figure 2.11).

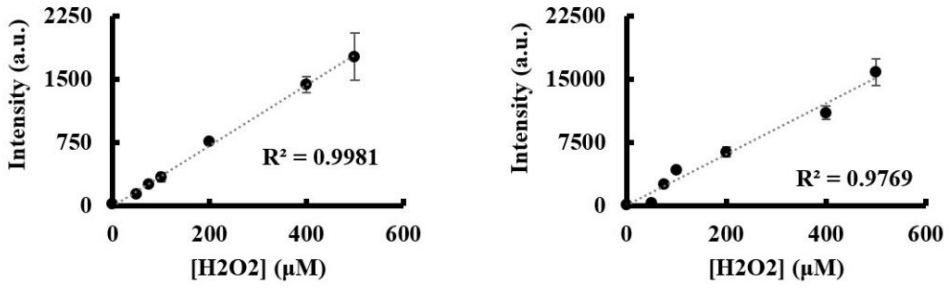

Figure 2.11. Standard curve for luminescent L-012 ROS detection with an exposure time of 20 minutes for the portable imager (left) and Kodak (right).

An increase in luminescence intensities was observed with increasing H_2O_2 concentrations. Analysis showed a strong linear relationship between luminescent intensities and H_2O_2 concentrations for both imagers (R^2 = 0.998 and 0.9769 for the portable imager and Kodak respectively). The limit of detection of the devices was found to be 3.98 ± 0.09 $\frac{a.u.}{\mu M}$ for the portable imager and 30.5 ± 1.18 $\frac{a.u.}{\mu M}$ for the Kodak. Similar to the previous study, it should be noted that the majority of this discrepancy in performance stems from the bit depth difference of

the CCD cameras. When both sets of data are normalized to 12-bit values, the difference in sensitivity is reduced (Figure 2.12).

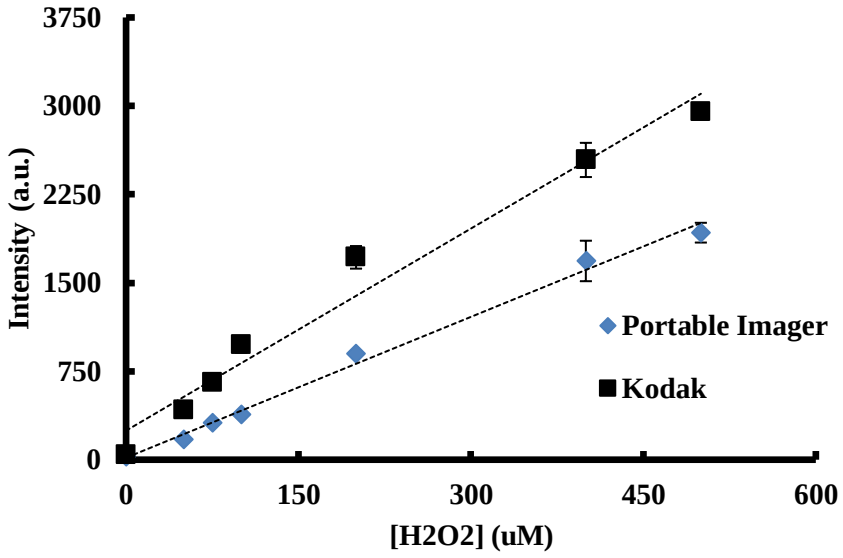

Figure 2.12. luminescent L-012 calibration curve normalized to 12-bit values for both imagers. This normalization reduces discrepancy between sensitivity values is reduced to less than double.

Upon normalization of the intensity values, the sensitivities of the two imagers become 3.98 ± 0.09 $\frac{a.u.}{\mu M}$ for the portable imager and 5.71 ± 0.22 $\frac{a.u.}{\mu M}$. This analysis displays that, similarly to the fluorescence calibration curve, the majority of the difference in luminescence sensitivity between the two imagers is due to the difference in bit depth between the two cameras.

The limit of detection for the portable imager was found to be 0.88 uM compared to the 0.70 uM of the Kodak, suggesting the ability to detect similarly low concentrations of ROS. These results show that the portable imager can

detect H_2O_2-associated luminescent signals and quantify H_2O_2 concentration *in vitro*.

2.4.3. In Vivo Models

2.4.3.1. In Vivo Fluorescence Calibration Curve

The *in vivo* sensitivity of the imagers was tested using a mouse subcutaneous injection model. Twofold serial dilutions of NIR Cy5 dye (7.50, 3.75, 1.88, and 0.94 mM) were injected under the skin in discrete locations on the dorsal area of deceased mice. Images were then taken immediately using both the Kodak and portable imagers and the fluorescent intensities were quantified (Figure 2.13).

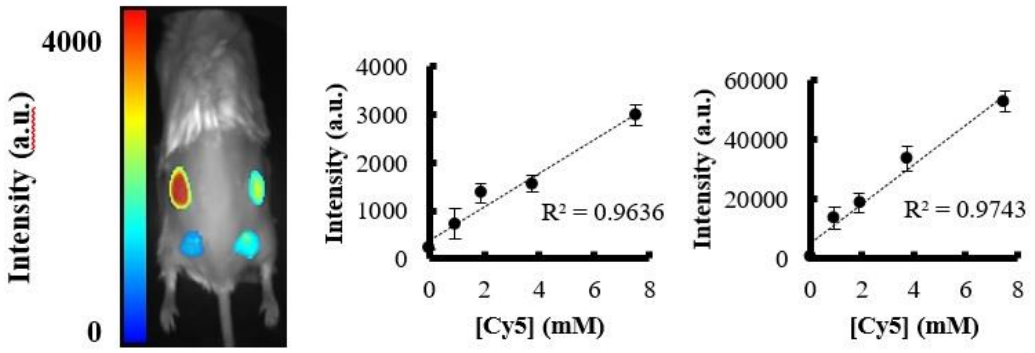

Figure 2.13. In vivo fluorescent imaging of NIR Cy5 dyes in different concentrations in mice. (Left) Representative fluorescent image of Cy5 dye in different concentrations imaged using the imagers. Linear relationships between dye concentrations and fluorescent intensities were determined based on imaging results obtained from (Middle) the portable imager and (Right) the Kodak system.

In a biological setting, the limits of detection for the portable imager and the Kodak imager were found to be 102 μM and 53 μM respectively. The sensitivity of the portable imager was calculated as 356.5 ± 14.9 $\frac{a.u.}{\mu M}$, while the Kodak

produced a sensitivity of 6650 ± 534.34 $\frac{a.u.}{\mu M}$. The data for both imagers was then scaled similarly to the *in vitro* version of this study to produce 12-bit data for each imager (Figure 2.14).

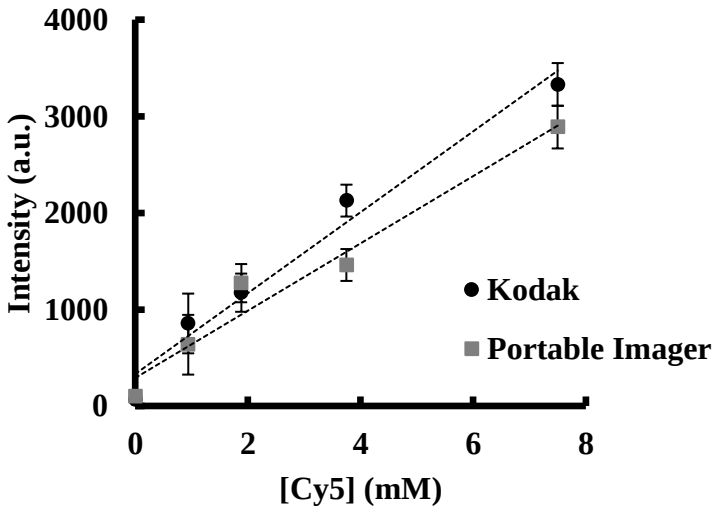

Figure 2.14. luminescent L-012 calibration curve normalized to 12-bit values for both imagers. This normalization reduces discrepancy between sensitivity values is reduced to less than double.

After calibration to 12-bit values, the sensitivity values were calculated as 356.5 ± 14.9 $\frac{a.u.}{\mu M}$ and 418.9 ± 33.6 $\frac{a.u.}{\mu M}$ for the portable imager and Kodak respectively, reducing the difference in sensitivity between the two imagers from almost two orders of magnitude to only 17%. These results suggest that the portable imager produces similar sensitivity responses to near-infrared fluorescent dye and has similar limits of detection to the Kodak *in vivo*.

2.4.3.2. Murine Wound Healing Model

In vivo imaging was conducted using a mouse excisional wound model to evaluate the ability of the portable imager to detect ROS-associated luminescent

signals in skin wounds. The portable imager was able to measure ROS in wounds at different stages (Figure 2.15c & d).

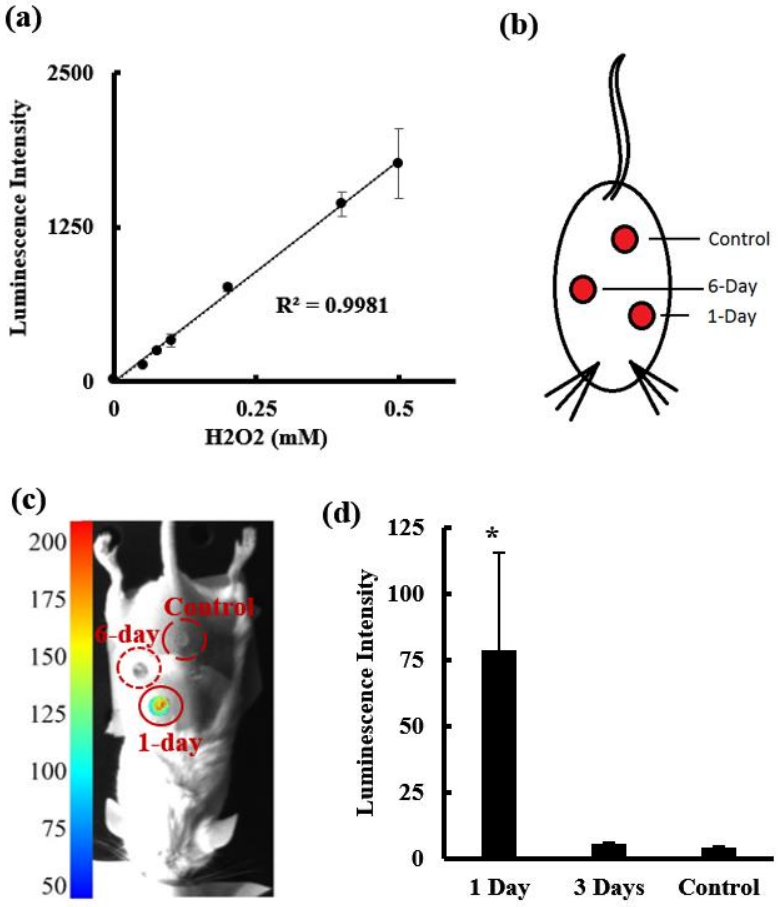

Figure 2.15. Luminescent imaging of ROS activities both *in vitro* and *in vivo*. (a) There is a linear relationship between ROS-producing H2O2 concentration and luminescent intensity *in vitro*. (b) An illustration of excision wound animal model with different wounds and healthy skin control. (c) Overlay image shows newer wounds display higher ROS activity. (d) The ROS activities in 1-day and 6-day wounds and controls were quantified and statistically analyzed.

Significantly stronger ROS signal was observed in 1-day wounds, which are known to have increased inflammatory cell responses and maximal ROS activities associated with the acute wound healing phase (Figure 2.15c). ROS activities were significantly lower in 6-day wounds and in control skin than 1-day

wound (Figure 2.15d). These observations are in agreement with previous findings.[33]

2.4.3.3. Murine Skin Inflammation Model

Previous studies have demonstrated that matrix metalloproteinases (MMPs) participate in infectious diseases' inflammatory responses and can be upregulated in response to the presence of bacteria toxin.[59,60,63] Using a subcutaneous mice skin infection model (as illustrated in Figure 2.16a) and a commercially available MMP-sensitive fluorescent probe (MMPSense750, PerkinElmer, Inc.), the ability of the portable imager to measure the production and release of MMPs was determined.

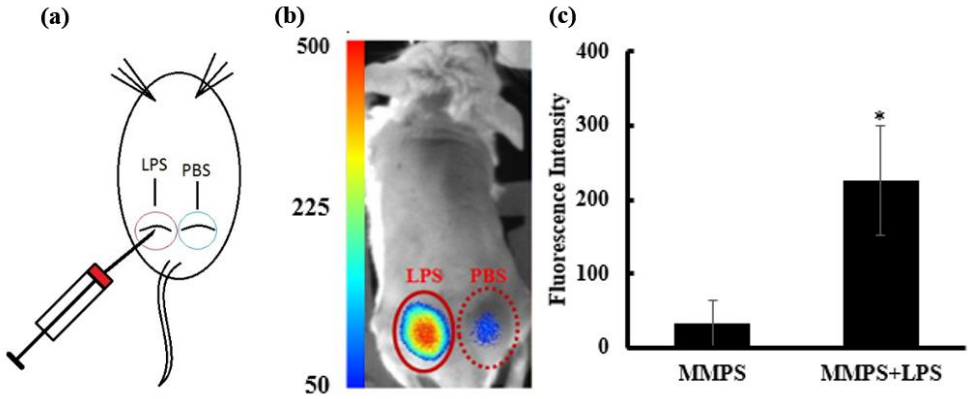

Figure 2.16. Quantification of MMPs activities in vivo using portable imager. (a) An illustration of skin infection model with the subcutaneous injection of LPS and PBS as control. (b) Fluorescent MMP signal was shown to be higher at LPS site. (c) Quantification of fluorescent intensities demonstrate that LPS treatment significantly increases MMPs activity in vivo.

An increase of significant fluorescent signal at the LPS treatment site was observed. Quantification analysis showed an approximately 8 times higher

fluorescent intensity in the LPS-treated area than in the PBS-treated area (Figure 2.16c). These results are in agreement with previous studies.[24,25]

2.5. Discussion

Many NIR and luminescent probes have been developed to detect inflammatory response and infection in wounds.[12,64–66] However, these exciting research advancements can only currently affect small animal studies, for which several commercial imagers are available for the detection of fluorescent and luminescent signals. Since all commercial imagers use an enclosed black box design, they cannot be converted for disease detection or diagnosis for human patients in a clinical setting. To overcome this limitation, an open and portable imager was developed in this aim. To assess its sensitivity, accuracy, and practicality *in vitro* and *in vivo*, the portable imager was evaluated and compared with a commercial small animal imaging system – the Kodak *In Vivo* FX Pro. It is well-established that Kodak system, like many other commercial products, has industry standard detection sensitivity and accuracy.

The portable imager design uses a LED ring/CCD setup which eliminates the need for black box enclosure, excitation filters, allows the system to image open surface without the issues with ambient light. The imager has a compact and flexible design, removing the need for bulky equipment that restrict the usage based on the subject size and geometry. The entire system can easily be transported to allow imaging of a subject in the most convenient location. It is also inexpensive compared to conventional *in vivo* wound imaging methods. The

portable imager can be further condensed into an external camera attachment and utilizes MATLAB-based software that is reliably user-friendly and gives the user extensive options for image analysis.

When compared with a commercially available *in vivo* imaging system from Kodak, this new imager design is highly competitive. The LED ring design produces an impressively uniform, symmetrical beam upon exposure to a sample. Although the Kodak imager produced a wider Gaussian peak, it displayed more noise over the "uniform" area. The imager was able to detect very low concentrations of dye despite inherent limitations from reduced biosensors and quantum efficiency, proving its feasibility for use in *in vivo* imaging applications. In short, although the Kodak system was shown to have better sensitivity and a larger view area, this design displayed significant potential to improve upon current imaging technology with further improvements, which will include developing a custom light source for a wider uniform illumination area.

The newly fabricated imager was shown to capably monitor wound environment and conditions using commercially available luminescent and fluorescent probes. In a wound inflammation model,[33] the new device was able to measure luminescence signals emitted from a ROS-detecting probe in acute wounds, providing proof-of-concept for the suitability of this setup for wound visualization applications. In addition, by quantifying fluorescent signals emitted from MMP sensitive fluorescent probes in a wound infection model, our studies have shown that the portable imager has the ability to detect wound infection in

mice.[59] Together, these studies give strong support that the portable imager is capable of providing sensitive and quantitative measurement of luminescent and fluorescent signals in real time and *in vivo*.

However, the results of these studies also point to needs to make significant improvements to the design. First, to be practical for use in large animal or clinical settings, the device needed to be transitioned from a tabletop to a handheld platform. This necessitated both a reduction in weight and a change in form factor. Secondly, since this revision of the device required total darkness to image luminescent signals, the device required the addition of a light isolation mechanism to open the possibility of luminescence imaging in pre-clinical and clinical scenarios. Additionally, an increase in homogeneous view area was desired to introduce the possibility of imaging larger surfaces, such as skin wounds on large animals or abdominal ulcers on humans.

The next chapter of this work focuses on the first two improvements and their application in a large animal pre-clinical wound healing study.

Chapter 3. Design of a Handheld Luminescence Imaging Device and Application in a Large Animal Wound Healing Model

3.1. Introduction

3.1.1. Luminescence Imaging Devices in Animal Research

Luminescence imaging shares many characteristics with fluorescence imaging but is distinct due to its lack of an excitation light source. Instead, luminescence imaging relies on probes or native biological molecules (chemi- or bioluminescence) that undergo chemical reactions to produce broad-spectrum white light. This property eliminates the need for an excitation light filter; however, all light entering the imaging environment is recognized by the sensor as signal. While this allows instrumentation for luminescence imaging applications to be simplified by the elimination of an excitation light source and emission filters, it also presents the unique challenge of ensuring the area between the sample and detector is free from light pollution.

Currently, *in vivo* luminescence imaging is typically carried out with a large, completely enclosed "black box" imager.[21,67,68] While these devices provide low noise and high resolution, they are expensive, immovable, and difficult to translate to human or large animal models due to their enclosed design. Several compact luminescence imaging devices have been recently developed to characterize wounds. In 2013, a simple smartphone-based system was developed for burn wound analysis.[69] This system was easy to use and widely available, but was unable to detect luminescence *in vivo* due to the camera's low sensitivity and

lack of a light shield. Near the same time, a ratiometric luminescent lifetime imaging device was fabricated to measure tissue hypoxia consisting of a simple RGB sensor.[70] This system was inexpensive and able to detect physiological hypoxia in a non-invasive manner, but required supplementary fluorescent data and a darkened room to function due to the lack of a light shield. In 2015, a consumer-grade camera was utilized to visualize human chronic wound bioburden using autofluorescent bacteria.[71] This system was portable and non-invasive but had several downfalls, namely requirement of a light shield, inability to detect luminescence signal due to low camera sensitivity, and reliance on biofluorescent strains of bacteria. There is a need for portable, light-isolated devices capable of imaging luminescence in a wide range of situations. Since luminescent imaging relies on light emitted directly from a probe or bioluminescent tissue, it does not require an excitation light source such as that required for fluorescence imaging. This allows the size and complexity of luminescence imagers to be reduced, which was a general goal of this imager design.

3.1.3. Role of ROS in Wound Healing

ROS plays a pivotal role in the orchestration of wound healing responses. Specifically, ROS and their associated radicals have been implicated as important intracellular second messengers at low concentrations, mediating responses such as ATP production.[72] ROS gradients also interact with platelets to facilitate thrombus formation after wounding.[24] In addition, ROS is a key factor in triggering cell division and migration in fibroblasts, keratinocytes, and endothelial

cells.[73,74] Critically, ROS is also produced by migrating inflammatory cells. It has been shown that vascularity has a strong connection with inflammation, inflammatory cell infiltration, and wound ROS levels. Specifically, inflammatory cells migrate along the endothelial surface and through post-capillary venules (25-50 μm diameter[75]) into the wound.[76] These cells release a large amount of ROS into phagosomes to kill engulfed bacteria as part of the inflammatory healing phase.[33,77,78] Macrophages recruited approximately 2 days post-wounding have also been shown to produce ROS.[79] In chronic wounds, excessive ROS released in wounds can delay healing and cause tissue damage.[24,31,80,81] Reducing ROS levels in chronic mouse wounds using antioxidants has been shown to move wounds out of the chronic cycle and into a healthy healing process.[82] ROS has been found to modulate angiogenesis by inducing expression of the pro-angiogenic growth factor VEGF in keratinocytes and macrophages.[33,83] Studies have also shown that ROS is a key regulator of vasorelaxation and inflammatory cell adhesion in blood vessel walls.[84] ROS gradients have been suggested to promote endothelial cell growth and migration at concentrations as low as 100 μM.[24,85] ROS also plays a critical role in wound infection and bacteria detection. Equally important, ROS levels may be increased by an order of magnitude in an infected wound.[86] Treatment of infected wounds with ROS-reducing antioxidants has been shown to significantly decrease wound bacterial bioburden.[82] Due to its many roles in healing, vascularization, and correlation to infection and chronicity in wounds,

there is a need to develop imaging methods that can visualize ROS distribution in wounds and their relationship to the vascular bed and infection.

3.1.4. Relationship Between Wound Healing, ROS, and Vascularization

Vascularization has a strong connection with inflammation, inflammatory cell infiltration, and wound ROS levels. Within the first 36 hours after initial injury, neutrophils are recruited from nearby blood vessels.[79,87] Specifically, these cells migrate along the endothelial surface and through post-capillary venules (25-50 μm diameter[75]) into the wound.[76] These produce burst ROS in order to kill engulfed bacteria as part of the inflammatory healing phase.[33,77,78] ROS levels have been found to increase by an order of magnitude in an infected wound.[86] Macrophages recruited approximately 2 days post-wounding have also been shown to produce ROS.[79] In chronic wounds, high levels of ROS produced during this phase of healing can delay healing and cause tissue damage.[24,31,80,81] Reducing ROS levels in chronic mouse wounds using antioxidants has been shown to move wounds out of the chronic cycle and into a healthy healing process.[82] ROS has also been found to modulate angiogenesis by inducing expression of the pro-angiogenic growth factor VEGF in keratinocytes and macrophages.[33,83] ROS gradients have also been suggested to promote endothelial cell growth and migration at concentrations as low as 100 μM.[24,85] Due to its many roles in healing and correlation to chronicity in wounds, there is a need for imaging methods that can visualize distribution of ROS over time in wounds and

correlate it with vascularization to gather new information about the wound healing process.

3.1.5. Objectives of This Work

This work was focused on optimizing the portable luminescence imager from Chapter 2 for luminescence imaging. Several facets of the device were modified or outright eliminated, such as excitation LEDs and optical filters, an unnecessarily large and heavy frame, the necessity for long exposure times (≥10 minutes), and inability to image in a lit room due to light isolation difficulties. The simple laser-cut acrylic frame was substituted with a complex CAD-designed, 3D-printed integration chamber. This casing was customized to provide switchable white light/luminescent imaging capabilities for *in vitro* studies as well as small and large animal wound models. To our knowledge, no portable, light-isolated device has previously been reported for use in large animal cutaneous wound models. The utility of the device was demonstrated both in *in vitro* ROS-detecting material characterization studies as well as in small and large animal wound models. The ability of the device to correlate visual discernment of blood vessel location with 2D ROS distribution in healing wounds in a large animal full-thickness cutaneous wound healing model was also displayed.

In this chapter, I summarize the development of a portable imager to significantly modify my previous imaging device (Generation I), which is only capable of imaging fluorescence and luminescence signals on small animals, but not on humans or large animals.[88] To overcome these drawbacks, a portable

imaging device was fabricated specifically for infection/bioburden detection on large animals via luminescence imaging. We accomplished this by significantly changing the design in several ways, notably substituting the simple laser-cut acrylic frame for a complex computer aided design (CAD)-designed, 3D-printed imaging chamber. This casing was customized to provide switchable white light/luminescence imaging capabilities for *in vitro* studies as well as large animal wound models. We demonstrate the utility of the device in a porcine model with full-thickness excision wounds incubated with *Psedomonas aeruginosa*. I display the ability of the device to correlate visual discernment of vascularity and ROS activities. Most importantly, these results reveal that wound bioburden can be diagnosed by observing the unique distribution pattern of ROS activity in wounds.

3.2. Design Objectives and Criteria

To meet the needs described above, the work in this chapter is focused on optimizing the tabletop fluorescence/luminescence imager from Chapter 2 into a handheld device for luminescence imaging in large animal applications. This shift in application for the revised device is shown below in Figure 3.1.

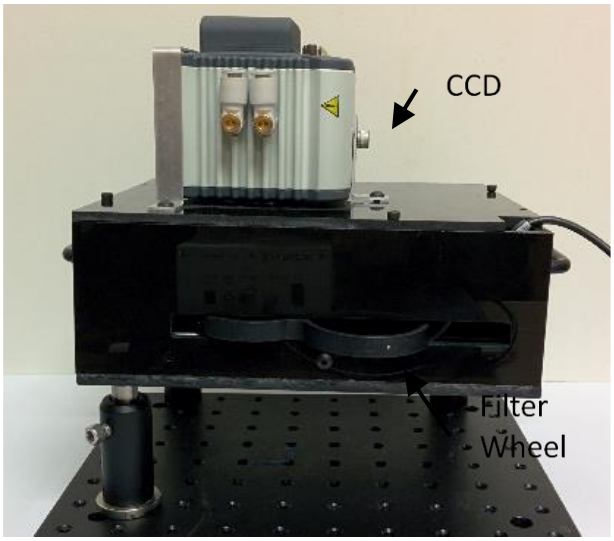

Tabletop Fluorescence/Luminescence Imager

↓

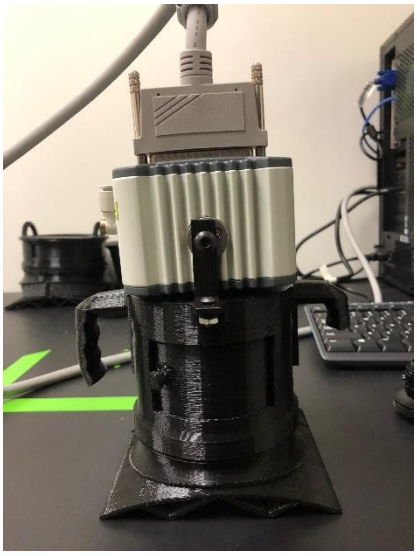

Handheld Luminescence Imager

Figure 3.1. The new luminescence imager developed from the initial tabletop imager in Chapter 2 is shown. This device is the first described that is capable of unenclosed large animal luminescence imaging.

The new portable luminescence imager was designed to image wounds on large animal models in a room with low ambient light. Key design parameters for

the portable luminescence imager included minimal size, high luminescence sensitivity, versatility between different imaging scenarios, and complete isolation from ambient light. The device has three major components: A CCD camera, an optical lens, and a custom-designed imaging chamber. A diagram of the imager and its components is shown in Figure 3.2.

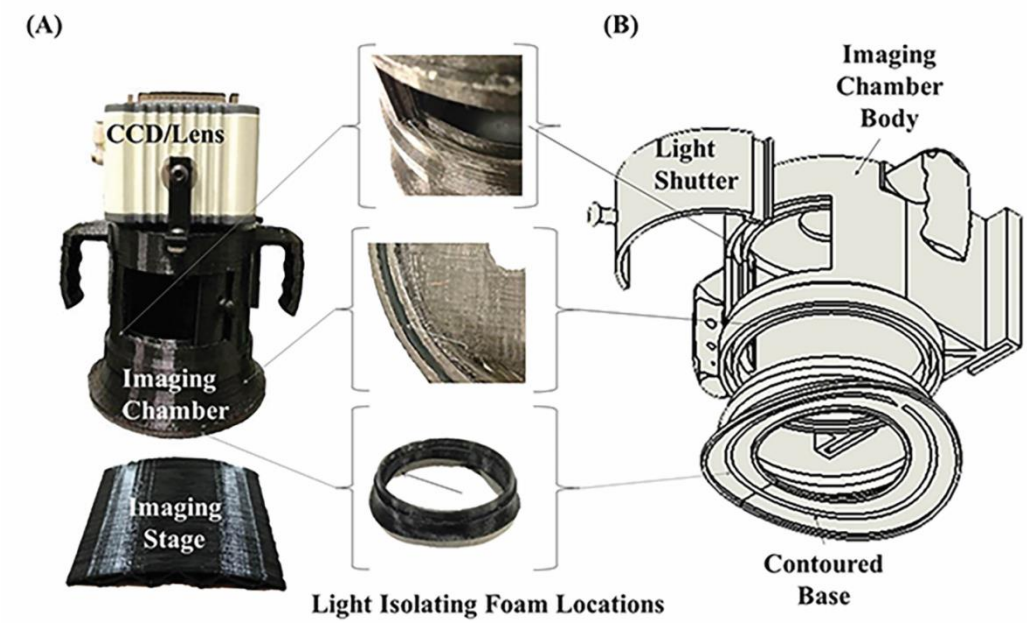

Figure 3.2. A breakdown of the components of the new imaging device is shown here. A) The device utilizes a multipart design consisting of a central section, an insertable sliding white light portal, and interchangeable bases. Luminescence and white light imaging can be switched between with the adjustable light portal. B) A drawing depicts the setup of various components associated with the imaging chamber.

The imaging chamber was designed in SolidWorks and 3D printed for ease-of-use in large animal imaging scenarios. The chamber consists of four main parts, including the main body of the device, a sliding white light shutter, a detachable base designed to contour to the surface of the animal being imaged,

and compressible light-isolating foam gaskets. The main body of the imaging device mounts to the camera and detachable base. It also contains integrated handles and an on-board standard Video Electronics Standards Association mount to allow for attachment to an articulating arm for hands-free use. The luminescence imager could also easily be removed from the arm and positioned by hand using the integrated handles. Its enclosed design also allows for the addition of Velcro straps to secure it to an animal for longer exposure times. An example of various large animal imaging scenarios is shown below in Figure 3.3.

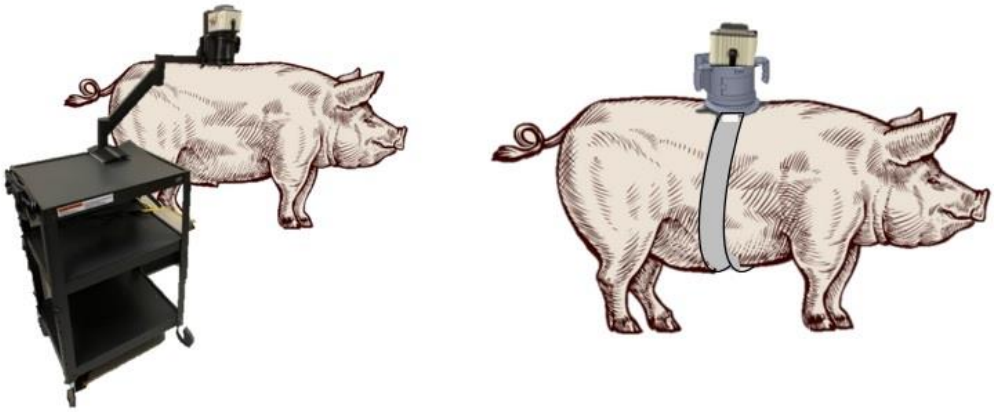

Figure 3.3. Large animal studies can be conducted using the portable luminescence imager with the cart/articulating arm option. It can also be affixed to the animal directly using Velcro straps or hand positioning via the integrated handles.

The white light shutter allows for rapid exchange between white light and luminescence imaging scenarios with minimal user interaction.

Several facets of the device developed in Chapter 2 were modified or outright eliminated in the new luminescence imager. The changes made according

the requirements of large animal and clinical luminescence imaging are summarized below.

3.2.1. Size and Weight Reduction

Since luminescence imaging relies on light emitted spontaneously by the subject, no excitation light source is necessary in a luminescence imager design. This allows the elimination of the LED light used in Generation 1 of the portable imager, as well as its associated driver, for a significant reduction in size and weight. Additionally, the emission filter and its rotating wavelength exchange mechanism were removed, further reducing the size of the device. Finally, the included adjustable legs and imaging objective were removed to transition the design from tabletop to handheld functionality. These changes resulted in a reduction of the size of the device from 22 x 22 x 22 cm to 17 x 13 x 17 cm and an 800g weight reduction.

3.2.2. Field of View Adjustability

In order to image objectives of different sizes, such as a wound on the hand vs. an abdominal ulcer, it was necessary to have a wide field of view range. This was solved by creating a complex, modular device with exchangeable bases of varying heights and widths. Through the addition of lenses of different focal lengths, a wide range of imaging options for different scenarios is possible. For proof-of-concept, two devices utilizing the same platform were designed for imaging at two distances (Figure 3.4).

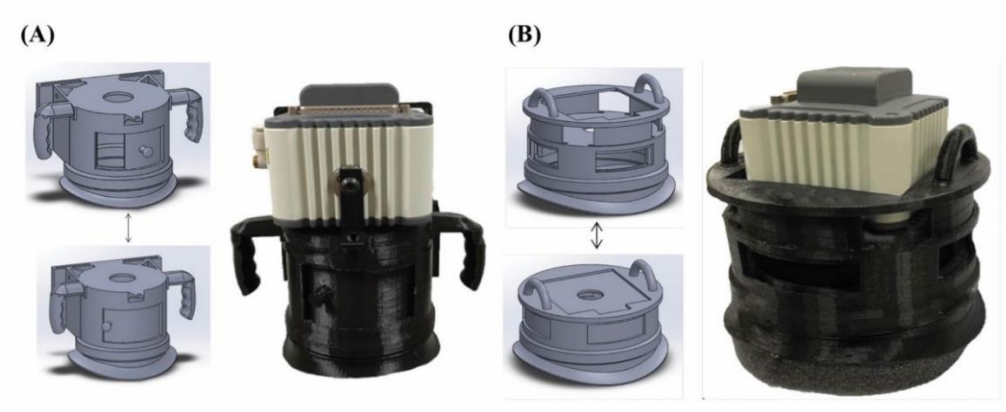

Figure 3.4. Two designs of a luminescent imager with different working distances and light shutter form factors. The device can be positioned on the region of interest using a pair of handles or mounted to an articulating arm. (A) An imager for imaging larger wounds (>3 cm diameter) has a 12 cm working distance while (B) an imager for imaging smaller wounds (< 3 cm diameter) has a 3 cm working distance.

These two revisions of the device were designed with lenses of different working distances to showcase the device's utility in different large animal imaging scenarios. The devices allowed different view areas to be captured: 5.14 x 4 cm (Figure 3.4A) and 4.75 x 3.5 cm (Figure 3.4B) for a zoomed-in or zoomed-out view as desired.

3.2.3. Tunable Light Isolation

The simple laser-cut polycarbonate frame was substituted with a complex CAD-designed, 3D-printed integration chamber. This casing was customized to provide switchable white light/luminescent imaging capabilities for *in vitro* studies as well as small and large animal wound models. This was accomplished by integrating recessed areas into the design for the integration of custom-fit light-isolating foam gaskets. The location of these fixtures is shown in Figure 3.5.

Figure 3.5 The locations of lightproofing gaskets that ensure light isolation during luminescence imaging is shown. These are integrated along the sliding white light shutter (upper left), where the top of the chamber connects to the exchangeable base (lower left), and along the bottom of the bases at the interface between the base and sample (right). These measures ensured complete light isolation during imaging.

It was also necessary to ensure ambient light was allowed to enter the chamber during the acquisition of white light images to orient the location of luminescent signals on the subject. To accomplish this, a sliding white light shutter was integrated. This feature is able to be manually open and closed by the operator. To our knowledge, no portable, light-isolated device has previously been reported for use in large animal cutaneous wound models.

3.2.4. *In Vivo* Imaging Considerations

In large animal and clinical *in vivo* imaging, tissue surfaces are rarely flat. Due to this, several modular bases were designed with different levels of curvature to match that of the required anatomical surface for a light-tight seal between it and the imager. The detachable base of the design is contoured to interface directly

with the surface of the animal being imaged. Several bases with different contours are shown in Figure 3.6.

Figure 3.6. Detachable bases designed to account for anatomical curvature of a swine's dorsal area are shown.

For both designs, bases matching the contour of a pig's back were created. For *in vitro* studies of the effect of animal curvature on imaging, a curved imaging stage with the same contour was also designed and 3D printed. Finally, compressible PU or PE foam gaskets are placed at interfaces to block ambient light. The foam gaskets form the base contours to shield the camera from ambient light for the porcine wound study.

To account for cross-contamination and sterility concerns, foam gaskets at the base of the imager were exchanged between imaging different subjects.

3.3. Materials and Methods

3.3.1. Materials

A CCD camera was used for image acquisition (C10600, Hamamatsu) with a F1.4/12 mm lens (HR961NCN, Navitar). These components were integrated into a novel light-insulated luminescence imager that was designed using Solidworks CAD software and 3D printed on a commercially available large-format 3D printer (gMax 1.5+, gCreate) using black polylactic acid (PLA, Hatchbox). Several imager designs were produced for applications ranging from *in vitro* to large animal studies. Light isolation was accomplished using shaped compressible polyurethane (PU) and polyethylene (PE) foam (McMaster-Carr).

3.3.2. Device Characterization

3.3.2.1. Confirmation of Light Isolation

The goals of developing the portable imaging device in Chapter 2 did not include ensuring total light isolation. Therefore, it was necessary to perfect the light-isolation strategy to allow for luminescence imaging in large animal models. Several strategies were attempted. These included the use of compressible light-isolation foam, blackout foils, and light-isolation fabric. Similar to the development of the initial device, these solutions were tested by applying the light-isolation technique and taking a 20-minute exposure (the maximum length of a typical imaging session) on a flat imaging surface. Background was then determined using WoundView™ software. Background is here defined as signal without the presence of a luminescent probe due to light leakage into the imaging

chamber. Ultimately, a combination of these strategies was implemented. Images taken using the same exposure parameters in total darkness were used as a control. This study was repeated 3 times for each light-isolation strategy. Average readings and standard deviations were calculated. The endpoint of this study was the development of a strategy in which imaging in an ambiently-lit room is statistically indistinguishable from imaging in complete darkness when a one-tailed unpaired t-test is applied. It should be noted that due to the novelty of this application, the method described above is novel.

3.3.2.2. Effect of Objective curvature on Light Isolation

It was critical to confirm that the light-isolation strategy was effective on surfaces of different contours *in vitro* before moving to large animal applications. To test this functionality, imaging stages of different contours simulating the curvature of different sections of the dorsal area of a juvenile swine were designed in Solidworks and 3D printed. Study 3.3.2.1 was then repeated. Stages of different contours simulating the curvature of different sections of the dorsal area of a juvenile swine were designed in Solidworks and 3D printed (Figure 3.7). Level of curvature was defined as the inscribed circular diameter of best fit of the contoured base.

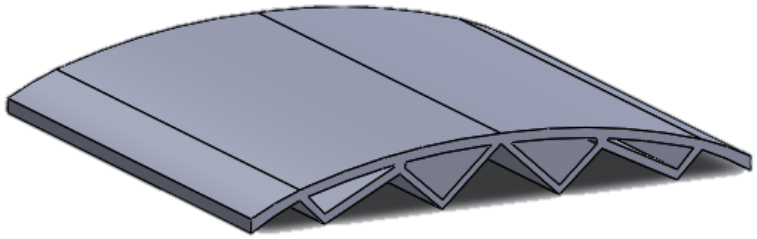

Figure 3.7. A custom stage designed to approximate the dorsal contours of a swine for testing the light isolation of the portable imager on a non-uniform surface.

Average readings and standard deviations were calculated. The endpoint of this study was the development of a strategy in which imaging in an ambiently-lit room is statistically indistinguishable from imaging in complete darkness when a one-tailed unpaired t-test is applied for any surface.

3.3.2.3. Curvature Effect on Luminescence Homogeneity

Homogeneity was determined on surfaces of different curvatures by arranging consistent droplets of H_2O_2 (100 mM, 20 μL) in a matrix pattern on the imaging stage and injecting luminescent L-012 in each droplet directly prior to imaging (5 μL, 48.3 mM). Luminescent signals were acquired for 12 minutes at 8x8 binning and consistency at the center and edges of the stage was quantified. Homogeneity was defined as a lack of statistically significant difference between the luminescent signals produced by droplets at the center and edges of the objective upon application of an unpaired one-tailed Student's *t*-test with an α of 0.05.

3.3.3. In Vitro Studies

3.3.3.1. ROS-Sensing Film Calibration Curve

ROS-associated chemiluminescent signals produced by the luminescent probe L-012 are typically low due to the low concentrations of ROS in wound environments. In order to reduce exposure times, instead of using only luminescent L-012 directly on wounds, a novel sensing film was developed by Progenitec. This film was used in all *in vivo* studies with the new imager.

The sensitivity and resolution of the film in response to difference concentration of ROS was characterized by applying 6 different concentrations of H_2O_2 to the films (50 uL, 0, 1, 5, 10, 25, 50, and 100 uM) with water as a control. Replicates of 3 were used. Intensity and ROS concentration were correlated and averages and standard deviations for each concentration were calculated. Sensitivity and limits of detection were determined and compared with unconjugated luminescent L-012 as described in Section 2.3.3.1. Statistically significant differences were determined with a paired 2-way Student's t-test, with differences deemed significant when $P \leq 0.05$. It was hypothesized that the new film would provide a longer luminescence lifetime and a significantly higher signal.[89]

3.3.4. Small Animal Models

3.3.4.1. Murine Wound Healing Model

The ability of the imaging modality to detect ROS in wounds *in vivo* was examined in a murine wound healing model.[61] All animal protocols in this chapter were approved and all animals cared for according to the standard guidelines approved by Animal Care and Use Committee (IACUC) at the University of Texas at Arlington and the University of Texas at Southwestern Medical Center at Dallas in accordance with the Animal Welfare Act and Guide for the Care and Use of Laboratory Animals.

Mouse wounds were imaged by placing the animal within the imaging device under isoflurane anesthesia (2 min, 8x8 binning). ROS probes were applied onto wounds immediately prior to imaging. Luminescent ROS signals were quantified using WoundView software. Analysis was completed by calculating average intensity in each wound over time for comparison with control skin. The ability of the imaging system to differentiate between acute wounds and healthy skin was investigated. Luminescent signals from each wound and control skin were averaged and their standard deviations were calculated. An unpaired 2-way Student's *t*-test was used to calculate significant difference. It was hypothesized that the imaging device and ROS-sensing film system would detect a significantly higher ROS signal in wounds compared to healthy skin.[31]

3.3.5. Pig Wound Healing Model

The ability of the new luminescence imaging device to detect ROS in wounds *in vivo* was examined a porcine wound model.[37,90] Swine were chosen for this model due to the physiological similarity of pig and human skin, including dermal thickness and adherence to subdermal fascia.[91,92] Vascularization was observed under white light illumination and ROS observed using luminescence. An established excisional wound model was used.[90] Briefly, female pigs with a weight between 90 and 120 pounds were used in this investigation. Aseptic technique was used to create 6 full-thickness wounds (3 cm diameter, 2 wounds per treatment group per animal) on the dorsolateral surface of each animal. After wounding, two wounds per animal were inoculated with approximately 2,000 colony-forming units (CFUs) of *Pseudomonas aeruginosa* (American Type Culture Collection 27853) per wound. All wounds were packed with gauze and covered with Tegaderm (3M). Dressings were changed at days 3, 7, 10, 14, 17, and 21. Before dressing changes, a circular section of ROS-sensing film was applied to the wound prior to wound imaging. The imager was then positioned over the wound and the light portal was moved to the open position. A white light image was then acquired for blood vessel visualization. Finally, the light portal was moved to the closed position and a luminescence image was acquired. Wounds were imaged and analyzed using WoundView™ software as described above. The relationship between blood vessel location and ROS distribution was investigated. Additionally, the change in average intensity over time was

compared between infected and uninfected wounds. Finally, the difference in infected versus uninfected wound ROS cluster number and average integrated density (defined as the sum of cluster intensity values divided by cluster area) was analyzed.

3.3.5.1. Relationship between ROS Gradients and Vasculature Distribution

The portable luminescent imager's ability to visualize both vascularization and ROS distribution in healing wounds was analyzed using a porcine wound healing model. Vascularization was observed under white light illumination and ROS observed using luminescence.

From these images, the relationship between blood vessel location and ROS distribution was investigated. In this novel analysis, ROS-associated luminescence patterns were compared with white light images showing vasculature location. For each wound, the average intensity adjacent to visible vessels was compared with average intensity in the rest of the wound bed as measured using ImageJ image processing software. The intensities were then normalized based on the maximum luminescence intensity for each image to account for variance between wounds. A paired two-tailed t-test was then performed comparing normalized intensity near large blood vessels with that in other areas of the wound over the course of the study. Finally, a z-transform test was conducted as previously described to determine if, cumulatively, intensities over large blood vessels are lower than intensities in other areas of the wound.[93]

Briefly, a test statistic (Z_s) was calculated from transformed P-values (Z_i) from *k* paired, one-tailed t-tests computed for each wound according to Equation 3.1:

Equation 3.1

$$Z_s = \frac{\sum_i^k Z_i}{\sqrt{k}}, \quad Z_i = tanh^{-1}\mathrm{P}_i$$

This value was then compared to Z_{crit} values for a 95% confidence interval (± 1.96). It was hypothesized that the ROS-associated luminescent intensity would be higher over capillaries than large blood vessels due to their role in ROS-producing inflammatory cell migration into the wound bed.[24,76,77,79]

3.3.5.2. ROS Levels in Infected and Uninfected Wounds over Time

In the pig wound healing study described above, the trend of ROS intensity over time was analyzed and compared for infected and uninfected treatment groups. For each wound, average and maximum intensities was calculated. The trend of these intensities was analyzed over the course of the 28-day study. The difference between these trends of the treatment groups was analyzed using a paired two-tailed t-test. It was predicted that ROS intensity would increase during the acute inflammatory phase of wound healing (Days 1-4), peaking at Days 4-7 and decreasing for the duration of the study.[76,78,87] It was also hypothesized that infected wounds would peak at higher intensity levels and decrease more slowly than uninfected wounds for the duration of the study due to increased ROS-producing inflammatory cell presence in response to bacteria.[31,76,79]

3.3.5.3. Difference in ROS Distribution of Infected and Uninfected Wounds

The difference in ROS patterns of distribution was compared between infected and uninfected wound treatment groups. For each wound image, the uniformity of each wound image will be analyzed in a novel method as described in Section 3.3.5.4. Uniformity was quantified as clusters per wound area and average cluster integrated density.[94,95] The statistical difference between these two groups will then be determined using a paired two-tailed t-test. It is hypothesized that infected wounds will have a significantly higher number of clusters and lower uniformity due to the clustering behavior of bacteria and the upregulation of inflammatory cell-produced ROS in response to bacterial load.[76,77,96]

3.3.5.4. MATLAB Analysis

Image segmentation for Study 3.3.5.3 was completed using a custom MATLAB script. Briefly, this program takes inputs of two sets of a user-defined number of infected and uninfected images. The operator then sets a segmentation threshold as a percentage of maximum intensity and transforms the images to filter out all signal below the specified threshold. The program then automatically segments the image into defined clusters and calculates values for clusters per square centimeter and average cluster integrated density. Surface plots are also generated for all images for visual comparison. This data is then exported as an Excel file for generation of graphs and charts for presentation. An image of an infected and uninfected wound before and after processing is shown in Figure 3.8.

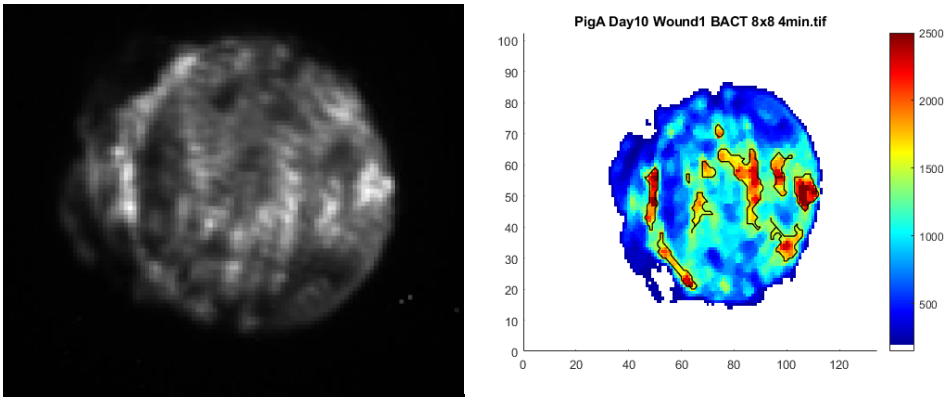

Figure 3.8. Example of a wound image processed in MATLAB to precisely determine the number and intensity of ROS clusters.

3.4. Results

3.4.1. Device Characterization

3.4.1.1. Efficiency of Different Light Isolation Strategies

Luminescence imaging was found to be greatly affected by ambient lighting conditions. Luminescence imaging does not utilize an excitation light source or emission filter but relies on light emitted from a sample. Any ambient light that enters this light path is recognized by a camera as signal. Longer exposures are also usually necessary for luminescence imaging, allowing more time for light pollution to obscure a signal. To ensure total light isolation of the new design, background was measured using a 20-minute exposure time with the fabric light shield used for fluorescence imaging, shown in Figure 3.9.

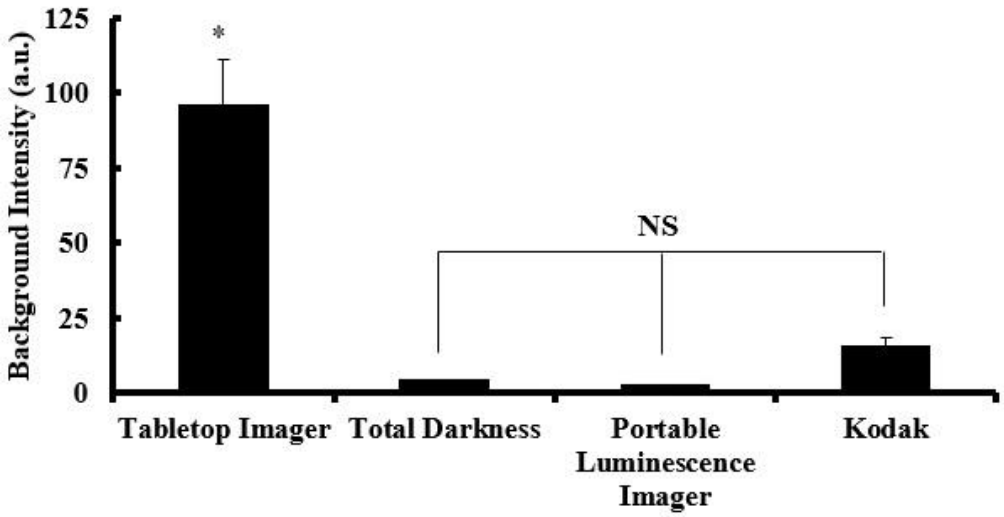

Figure 3.9. Compared with the background signal experienced by the portable imager designed in Chapter 2, the new luminescence imager has a significantly lower background. The background of the new imager is indistinguishable from imaging in total darkness or imaging with the Kodak.

With full ambient lighting, such as the conditions that would be found in a patient's room or clinic, background was found to be unacceptably high in the tabletop portable imager developed in Chapter 2. With the integration of the light isolation strategies discussed above, the new device was found to completely eliminate even bright ambient light from the imaging area over long exposure times and allow for imaging of even weak luminescent signals. Imaging with the revised design was found to be indistinguishable from imaging in total darkness ($P = 0.141$) and imaging with the Kodak ($P = 0.057$).

3.4.1.2. Curvature Effect on Light Isolation

The ability of the novel imager to isolate the imaging environment from ambient light in a lit room was compared to the light isolation solution from the previous fluorescent/luminescent imaging device (blackout fabric). Several adapters were

used with varying curvatures (flat vs. curved with radius of 20 or 15 cm) to assess the effect of a curved stage interface on light isolation. Images were taken at exposure times of 4 minutes and 8x8 binning in a lit room and background signal was quantified (Figure 3.10).

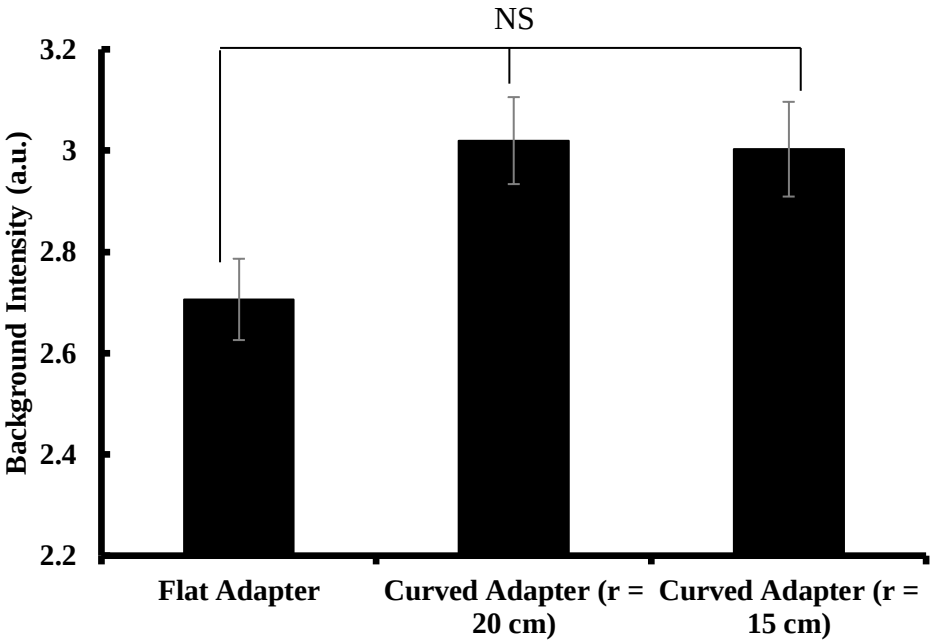

Figure 3.10. Comparison of light proofing efficiency between different imagers and contoured imager base designs. Images were taken under ambient light with the following imaging conditions: 8.8 binning, 4 minutes exposure. All bases were found to have acceptable background levels (below 10 a.u.) and represent a significant improvement over the previous imager's background levels.

The new luminescence imager was shown to be light-tight even in a lit procedure room for both flat and contoured surfaces, with background values statistically equivalent to total darkness in the imaging room. This was a background intensity reduction of ~30 times from the imager designed for both

luminescence and fluorescence, which enabled the detection of even weak luminescence signals without interference in the new device.

3.4.1.3. Curvature Effect on Luminescent Homogeneity

The homogeneity of luminescent signals on surfaces with varying degrees of curvature was investigated to identify any significant decrease or variation in intensity with a consistent ROS signal across the field of view. Curvature was defined as the inscribed circular radius of the base. Droplets of H_2O_2 (100 mM, 20 μL) were arranged in a matrix pattern on the imaging surface. Before imaging, luminescent L-012 (5 μL, 48.3 mM) was added to each droplet. It was determined that there is no significant difference of luminescent intensities detected by imagers with flat and curved bases. In addition, the extent of curvature has no significant influence on luminescent intensity at different regions from the center of the imaging area to the edge (Figure 3.11).

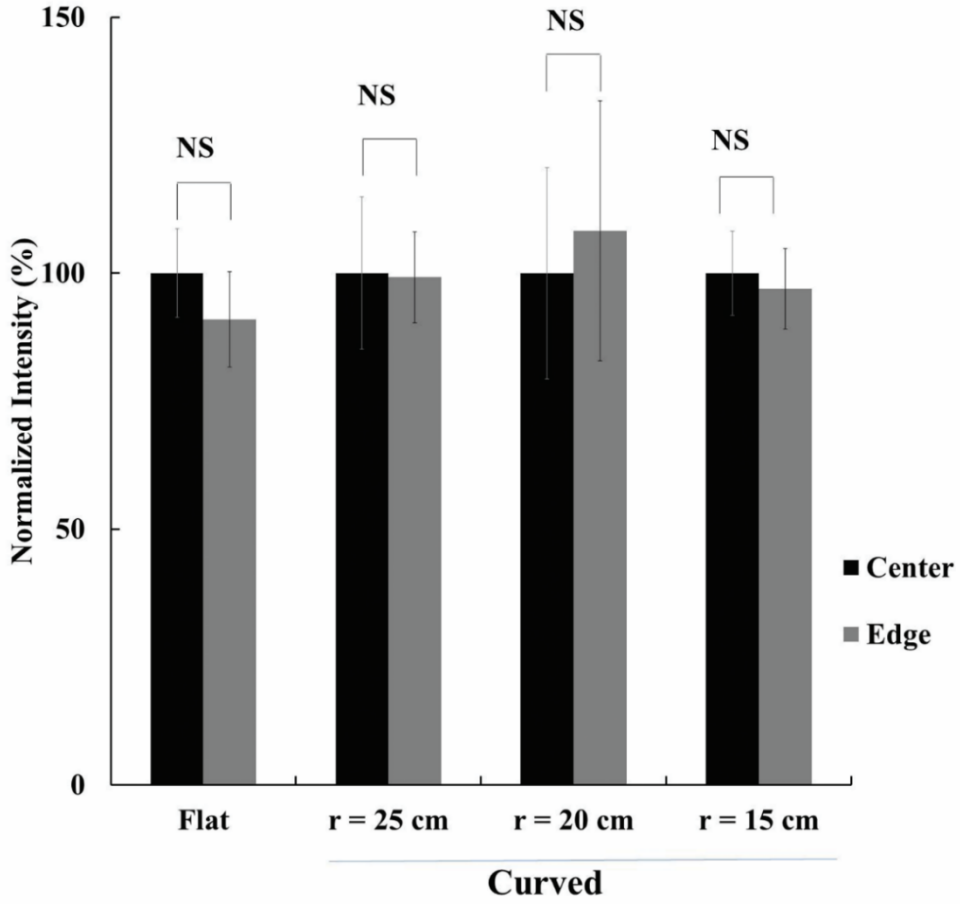

Figure 3.11. The effect of base contours on luminescence homogeneity was assessed by quantifying a matrix of H2O2 mixed with the luminescent ROS probe luminescent L-012 arrayed over the view area of each stage with various curvatures. We statistically analyzed the luminescent intensities between edge and center (calibrated as 100%) on different platform. We find that curvature has no statistically significant influence on the luminescence readings by comparing the readings at the center and edge of the base plate

These results support that the imager with curved bases can be used for imaging curved objectives such as a porcine back or human torso without the necessity to perform additional intensity calibration.

3.4.2. In Vitro Studies

3.4.2.1. ROS-Sensing Film Calibration Curve

The sensitivity and resolution of the relationship between ROS concentration and ROS-sensing film luminescence was characterized *in vitro* (Figure 3.12). Several concentrations of H_2O_2 within the physiologically relevant range (5 μL; 0, 1, 5, 10, 25, 50, and 100 μM) were applied to luminescing ROS-sensing film or treated with the luminescent probe luminescent L-012. Exposures were taken immediately after treatment.

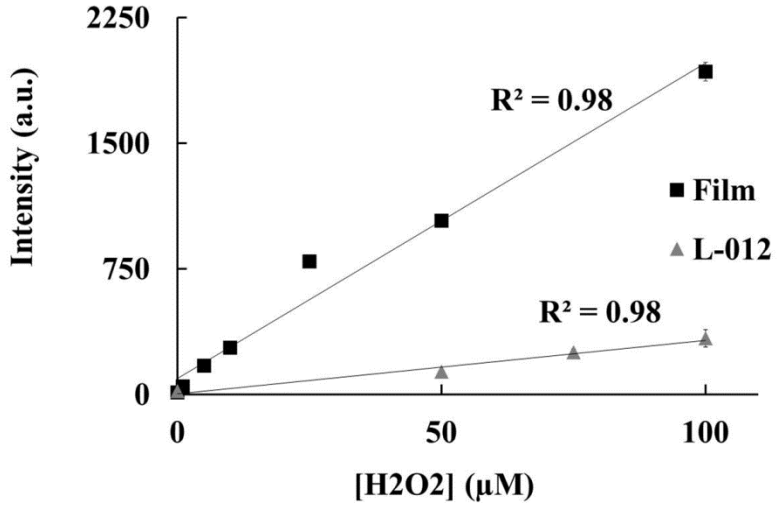

Figure 3.12. The ability of the luminescence imager to quantify ROS was tested in vitro using ROS-sensing film or the probe luminescent L-012. The imager was found to be capable of detecting physiologically relevant concentrations of ROS (less than 5 μM). ROS-sensing film was found to have significantly lower LOD and higher sensitivity than luminescent L-012.

The imager was found to correlate luminescent signal and ROS concentration with a robust linear relationship for both the ROS sensing film and luminescent L-012 (R^2 = 0.98). The imaging system also showed high sensitivity

(k_{film} = 18.9 ± 0.4 $\frac{a.u.}{\mu M}$, $k_{luminescent\ L\text{-}012}$ = 3.2 ± 0.2 $\frac{a.u.}{\mu M}$) and was able to detect low concentrations (LOD_{film} = 0.11 uM, $LOD_{luminescent\ L\text{-}012}$ = 1.2 uM). The results support that the imager has excellent luminescence sensing properties sufficient for *in vivo* imaging.

3.4.3. Small Animal Models

3.4.3.1. Murine Wound Healing Model

The ability of the imager to detect ROS in wounds was evaluated using a murine full-thickness excisional wound model. Mice were anaesthetized and placed inside the luminescence imager. A diagram of the experimental design and the difference in average luminescence intensity between wounds and healthy skin is shown (Figure 3.13).

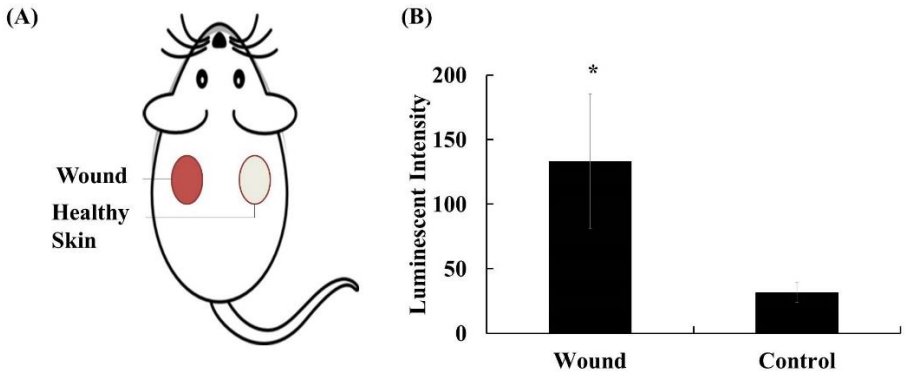

Figure 3.13. The portable imager was used to assess ROS activities in a mouse cutaneous wound model. (A) A diagram of the experimental setup is shown. (B) ROS activity was successfully detected and quantified on acute wounds with high intensity at an exposure time of 120 seconds. This signal was used to successfully differentiate between the wound and healthy skin.

The luminescence imaging system was found to be able to detect significant ROS signal *in vivo*. The system was able to reliably differentiate between healthy skin and wound tissue, showing greater than a 3-fold difference in signal with a P of 0.029. These results are in agreement with our previous results as well as independent studies.[27,33] This study confirms the adequate sensitivity and stability of the luminescence imager for *in vivo* wound healing studies.

3.4.4. Pig Wound Healing Model

3.4.4.1. Relationship between ROS Gradients and Vasculature Distribution

The ability of the portable imaging device to correlate ROS distribution via luminescence and blood vessel location via white-light imaging was investigated. Luminescent and white light imaging pairs were used to create overlaid images of ROS levels and blood vessel distribution. Wounds with clearly visible blood vessels at Day 1 were analyzed over the 21-day study (n = 7). As shown in the representative image (Figure 3.14A) and graphical comparison (Figure 3.14B) of the change in intensity in wound areas, we find the majority of ROS activities are found at the area nearby capillaries and far away from large visible vessels (0.5 mm diameter). Large vessels were enhanced in red for increased visibility.

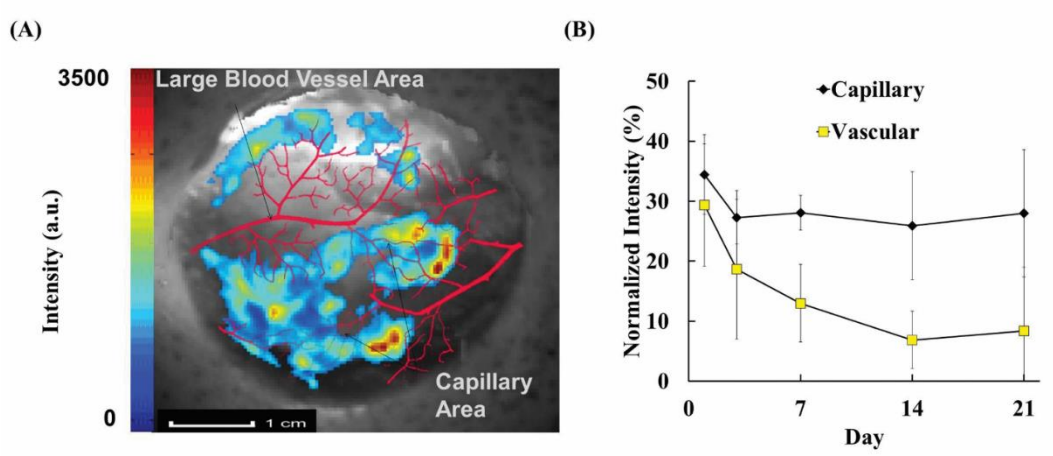

Figure 3.14. Luminescence (ROS) and white light (blood vessels) images were captured for each wound. The spatial relations between ROS activity and vasculature are shown in a representative wound. (A) Luminescent ROS images were overlaid on white light images of the wound bed to reveal the relationship between ROS activity and vasculature (shown enhanced in red). (B) Higher intensity was found to inversely correlate with large blood vessel location. This trend was found to be stable over time and statistically, with ROS intensity in capillary-associated areas of the wound roughly double than areas associated with large vessels on average.

By analyzing the luminescent intensity and vasculature distribution (Figure 3.14B), we find that ROS intensity is significantly higher in areas of the wound ≥ 2.5 mm away from large visible blood vessels ($Z_s = 0.44$, $Z_{crit} = \pm 1.96$). The results support that ROS activity is highest in capillary-dense areas of the wound bed, rather than in the vicinity of larger, visible vessels. This is consistent with expectations and current understanding of ROS production in healing wounds.[75,80,89]

3.4.4.2. ROS Levels in Infected and Uninfected Wounds over Time

The luminescent signals between infected and uninfected wounds over 21 days was compared. A representative image panel showing uninfected and infected wound ROS levels at 1, 3, and 7 days is shown in Figure 3.15A.

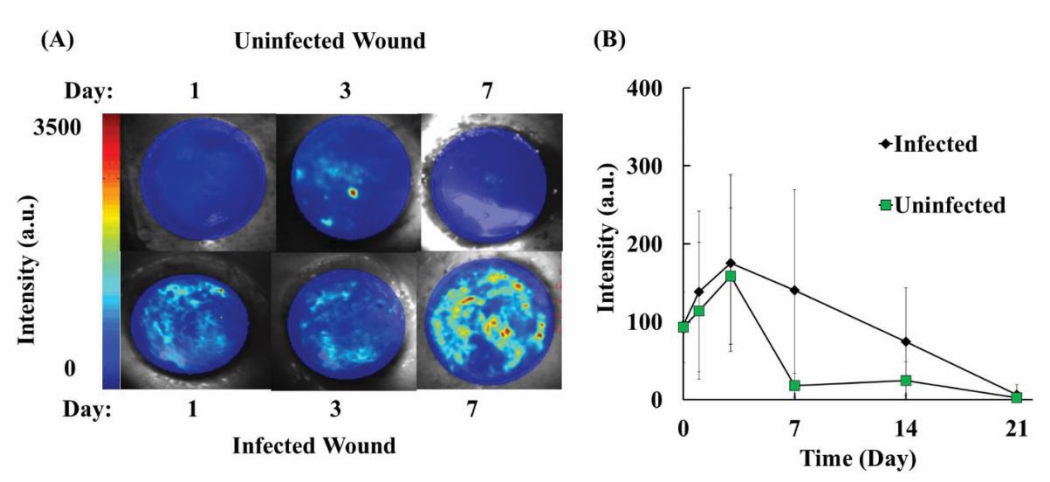

Figure 3.15. The change in luminescent intensity of infected and uninfected wounds was documented for 21 days with the luminescent imaging system. (A) A representative panel of overlaid luminescence/white light images of infected and uninfected wounds over the first seven days is shown. (B) The line graph of average wound ROS-associated intensity changes over time shows that there are significantly higher ROS levels in infected wounds over the duration of the study, especially on Days 7 and 14, than in control wounds (P = 0.019).

Wounds with high bioburden were found to maintain high ROS levels longer than uninfected wounds (P = 0.019). This effect was most prominent from Days 3 to Day 21, with much of the ROS intensity for uninfected wounds remaining very low after 1 week (Figure 3.15B). ROS levels in infected wounds were found to peak between Day 3 and Day 10, while uninfected wounds declined quickly after day 3. This finding supports established knowledge of ROS responses in normal and infected wound healing in a new two-dimensional model.

3.4.4.3. Difference in ROS Distribution of Infected and Uninfected Wounds

In addition to increased ROS activity, it was also observed that infected wounds have more clustered high-intensity ROS areas (Figure 3.16). ROS distribution patterns between infected and uninfected wounds were compared, selecting one time point with the maximum ROS signal for each wound for consistency. To visualize this, surface plots were generated to compare peak height and size between infected and uninfected wounds (Figure 3.16A). In MATLAB, intensity clusters above a 70% maximum intensity threshold were detected and quantified for infected and uninfected wounds. The number of clusters in the wound area was then defined and compared between the two treatment groups (Figure 3.16B). In addition, average integrated density was compared between the two treatment groups (Figure 3.16C).

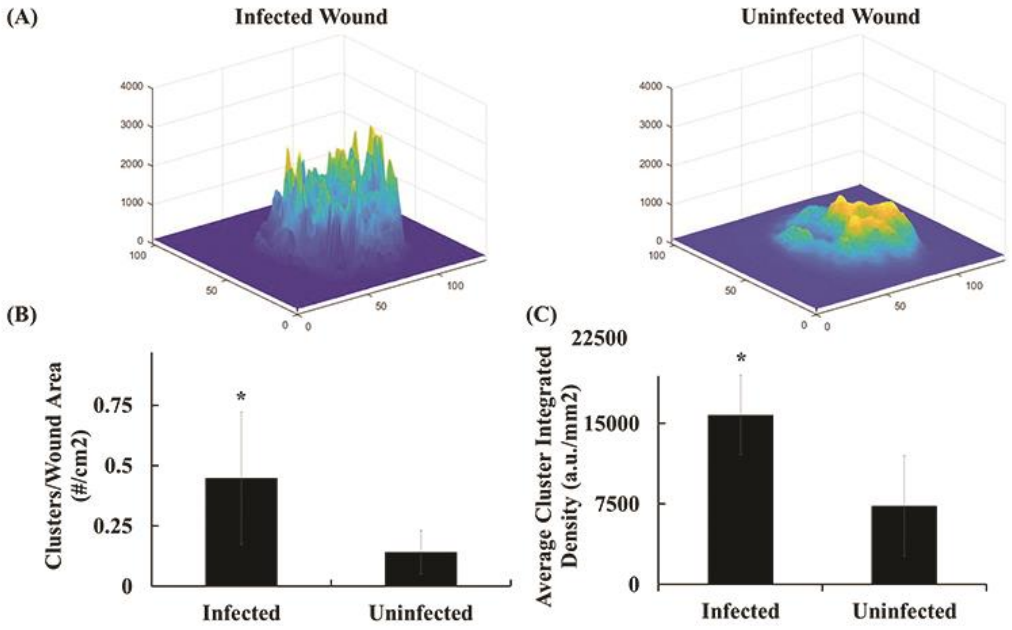

Figure 3.16. ROS distributions in infected and control wounds were compared. (A) Wound images for infected and non-infected wounds were analyzed in MATLAB and surface plots were generated. Representative surface plots for both wound categories are shown here, displaying more numerous and sharper peaks in infected vs. uninfected wounds. (B) By comparing both groups of wounds, we find that infected wounds have larger numbers of high-intensity ROS activity clusters than control wounds (P = 0.04). (C) ROS cluster areas were observed to have higher integrated density per square millimeter in infected wounds than in uninfected wounds, supporting the observed sharper ROS intensity peaks in infected wounds (P = 0.014).

The imaging system discovered a more clustered distribution of ROS over the wound bed in infected than in uninfected wounds, with approximately 3 times the number of peaks occurring per cm^2 in infected wounds (Figure 3.16B, P = 0.04). It was also observed that cluster peaks of infected wounds were significantly steeper and sharper compared to the lower, broader peaks of uninfected wounds. Finally, by comparing the average integrated densities of cluster areas, it was observed that infected wounds have significantly higher

cumulative intensity signals in ROS cluster areas than non-infected wounds (P = 0.014). These results suggest a good relationship between ROS activity distribution, specifically cluster number and area-averaged integrated density, and bacterial colonization in wounds. These findings point to a less homogeneous and "patchier" ROS distribution in wounds with a high bacterial bioburden. Overall results suggest that the "patchier" ROS distribution can be used as a potential imaging signature for wound bioburden diagnosis.

3.5. Discussion

There is a robust demand for imaging modalities that can visualize molecular parameters of wound healing in a real-time, noninvasive manner. While many imaging methods have been developed with the capability to image wounds, many of them are too large to transport easily and require expensive instrumentation. In addition, imaging devices designed for *in vivo* measurement of luminescent signals are completely enclosed to prevent light contamination, which prevents the imaging of large animals and precludes interacting with the subject over the course of imaging. This report describes the refinement of our Generation 1 imager design into a portable imager optimized for detecting luminescence, particularly associated with ROS in skin wounds. Similar to the previously described imager design, this luminescence imager has many advantages over large commercial imagers, including increased portability, decreased size, and ability to image in a much wider range of scenarios due to its open design. The device is extremely lightweight and portable, allowing it to be

transported between imaging locations and positioned by one of several mounting options or by hand with ease. This presents significant advantages over commercially available black-box imagers, especially in niche applications such as rural clinic or battlefield medical imaging. A two-part design allows the sample-interfacing lower portion of the imaging device to be swapped with differently contoured parts for imaging in a wide range of scenarios, ranging from *in vitro* imaging on a tabletop to imaging the uneven surface of a large animal in a lit procedure room. The device has drastically reduced many issues associated with the early prototype, such as limited mechanical strength, a lack of adjustability, and inconsistencies in white light illumination.

Our results support that the new imager is able to detect ROS activity and bacterial bioburden in large animal wounds. Neutrophils have been found to be the major cell type responsible for ROS production.[12] Furthermore, ROS distribution and, perhaps, activated neutrophils, were found to accumulate more prominently at capillary-infused areas of wounds rather than areas adjacent to large vessels. This phenomenon is supported by the fact that the primary cellular producers of ROS in wounds, neutrophils and other inflammatory cells, migrate into the wound through post-capillary venules.[76] This trend was also consistent over the course of the study, with areas of the wound not populated with large visible vessels consistently expressing almost double the intensity of areas near these vessels. This represents the first visual observation of the relationship between ROS and blood vessel distribution in wound healing with the support of

many previous biological findings in inflammatory cell recruitment and associated redox responses.[75,80,97]

Wound bioburden, the result of bacterial colonization in wounds, has significant impact on wound healing and care. Wound bioburden/infection is typically diagnosed with visual observation and confirmed by laboratory culture, both methods with many drawbacks.[35,40] Briefly, visual observation may not be accurate for detecting bioburden/infection and laboratory culture is time consuming. Our study has shown that the combination of the developed luminescent imager and ROS probes can be used for real-time wound bioburden/infection detection. Using our imaging system, we find that infected wounds have significantly more clustered distributions of ROS than uninfected wounds. This is consistent with previous findings that show that ROS is highly correlated with local presence of bacteria.[76,77] The previously described clustering behavior of bacteria likely also contributes to this phenomenon.[96] This finding represents the first known association of 2D ROS distribution and wound bioburden/infection status *in vivo* and may pave the way for new methods of diagnosing bioburden/infection in clinical settings.

The ability of this device to visualize vascular distribution in conjunction with inflammatory markers makes it a strong fit for imaging and diagnosis of cardiovascular pathologies. For example, it is well established that capillaries are responsible for gas, fluids and cellular transport.[1,76,98] By conjugating biomolecules or cells with luminescent probes, we will be able to assess the

capillary function and activity under any physiological and disease condition using the imaging system developed here. In addition, this new imaging system has a strong potential for future research applications in both wound and cardiovascular inflammation and bioburden/infection imaging. Finally, and equally important, this portable imager permits the use of the luminescence imaging modality to investigate wound healing processes and vascular disease in humans.

Chapter 4. Design and Applications of Several Fluorescent Imagers and a Combination Fluorescence/Luminescence Imager for Various *in Vivo* Imaging Scenarios

4.1. Introduction

Although optical imaging is a burgeoning field of research in biomedical engineering, several important application gaps still exist. Current examples of portable fluorescence imaging devices in literature were mentioned above in Chapter 2. Notably, none of these examples were designed to image large surfaces, such as in a large animal study. There is a need for large-format fluorescence imagers to fill this need. In addition, there is a lack of imaging devices in literature capable of visualizing both fluorescent and luminescent signals. The goal of this work was the further development of the tabletop portable imaging device developed in Chapter 2 into a design capable of imaging in large animal and clinical applications, with the ultimate objective of merging an improved fluorescence imager with the large animal luminescence imager for a robust combination device capable of collecting new biological information in large animal and human clinical and research applications.

4.2. Design Objectives and Criteria

To meet the needs described above, this chapter focuses on optimizing the tabletop portable imager developed in Chapter 2 into a fluorescence imaging device that addresses the shortcomings of the original design. A diagram and 3D printed of the large format fluorescence imager is shown in Figure 4.1.

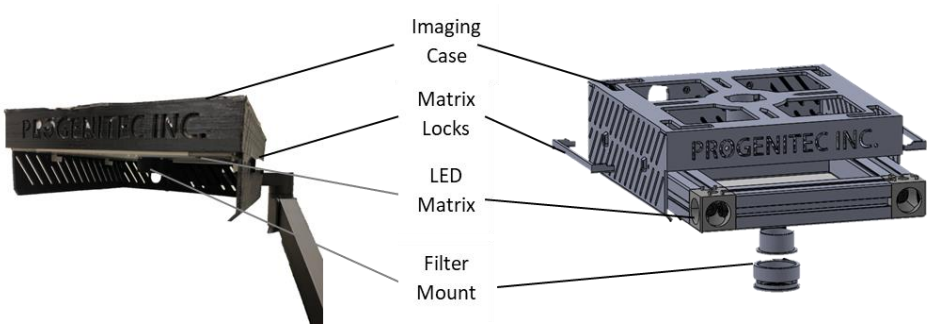

Figure 4.1. A manufactured large-format fluorescence imager is shown (left) along with the corresponding CAD model (right). The major components of this device are the 3D-printed imaging case, LED matrix and associated locking mechanisms, and filter mount containing the bandpass emission filters.

4.2.1. Case Design

The initial design consisted of the C-mount lens attached directly to the camera body, with the filter wheel and LED ring aligned beneath it by hardware mounting in a black box for imaging. While this setup was acceptable for single-wavelength imaging, it effectively prevented dual-wavelength imaging with its light source impossible to access without dismantling the device. The four-legged design also made changing the distance from the imaging objective difficult. The large drivers for the camera and LED ring were also discrete from the imaging components, making transportation difficult. This preliminary design is shown below in Figure 4.2.

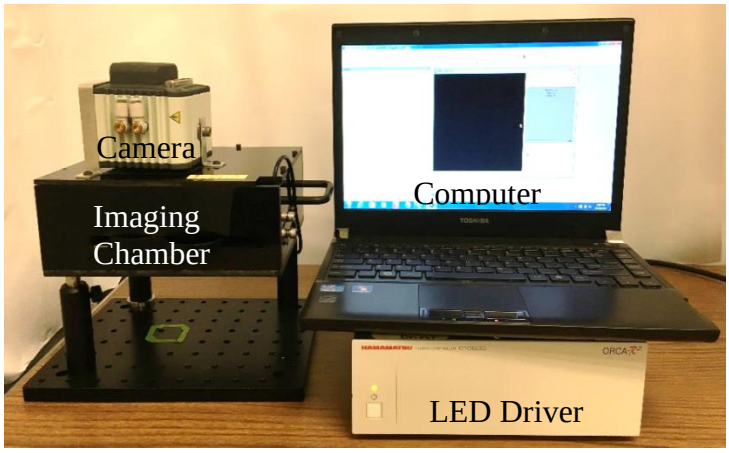

Figure 4.2. Initial black-box portable imager design.

To address these difficulties, a stand-mounted solution was designed and constructed. This allowed an LED ring to be mounted to a sliding fixture and easily slid into place on the bottom of the device. It also utilized a telescopic stand design for easier height change and increased access to the area between the imaging device and objective. Finally, all drivers and external devices were integrated into the body of the device, making the entire design compact and portable. This intermediate design is shown below in Figure 4.3.

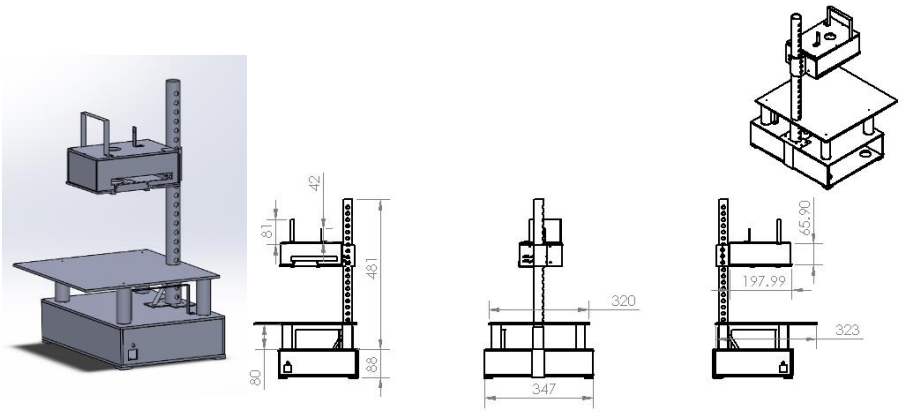

Figure 4.3. CAD rendering (left) and technical drawing (right) of the intermediate tabletop portable imager redesign.

Although this redesign represented a significant improvement, modifying the light source required additional changes. To incorporate the new LED matrix, it was determined that a more portable design with wider applicability for different imaging situations was the most suitable design route. To achieve this, an updated modular design was developed. This design is shown below in Figure 4.4.

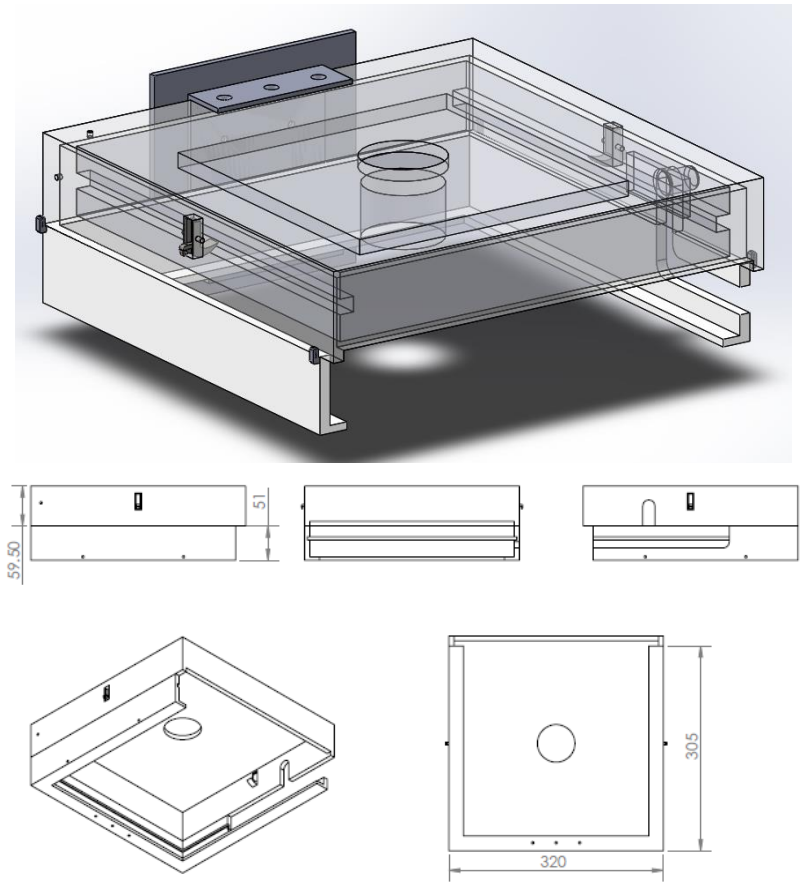

Figure 4.4. CAD rendering (top) and technical drawing (bottom) of the R3 intermediate portable imager redesign.

This intermediate imager design incorporated several new features for better portability and ease-of-use. Light sources could be loaded into the chamber and snapped into place, while a clamp system allows for easy release and exchange of excitation wavelengths with accessible cable port access. The camera and lens were mounted directly to the matrix casing. The device additionally incorporated a custom mounting solution for easy mounting to a cart-mounted articulating arm for the widest range of portability and range of motion.

This design was further refined into a tabletop design that could easily be 3D printed as a single part for enhanced durability, decreased cost of production, and faster rapid prototyping (Figure 4.5).

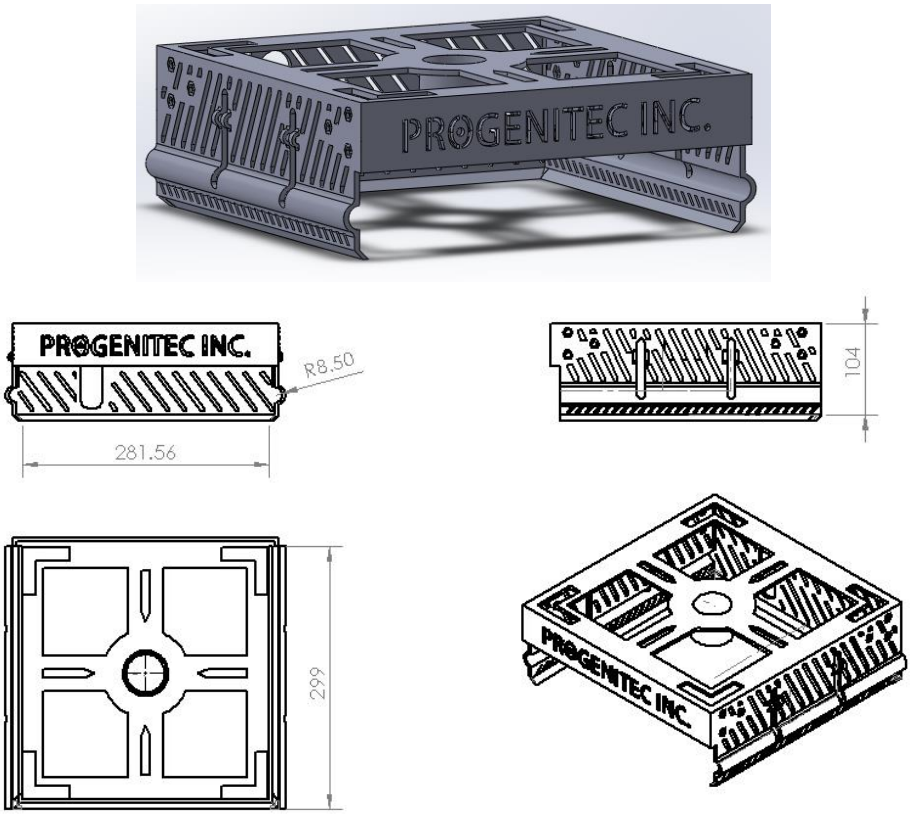

Figure 4.5. CAD rendering of R3 tabletop portable fluorescence imager (top) and technical drawing (bottom).

A mounting solution for the new bandpass filter holder was also integrated into the new design. Technical issues with the spring-loaded mounting mechanism of the initial matrix-oriented portable imager led to the development of an alternative: The LED matrices were modified with drop locks and set screws that were held in place in the imaging case with a 3D printed locking mechanism (Figure 4.6). A combination of rails and slots were integrated into the design to

allow the matrix to be loaded and unloaded. A vertically adjustable stand was designed and constructed from 8020 aluminum extrusions and fixtures.

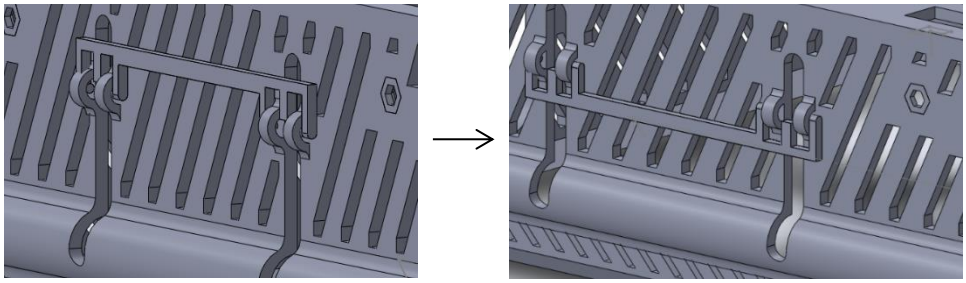

Figure 4.6. Updated locking mechanism for R3 of the tabletop portable fluorescence imager.

Several small changes were made to achieve the final portable imager design (Figure 4.7).

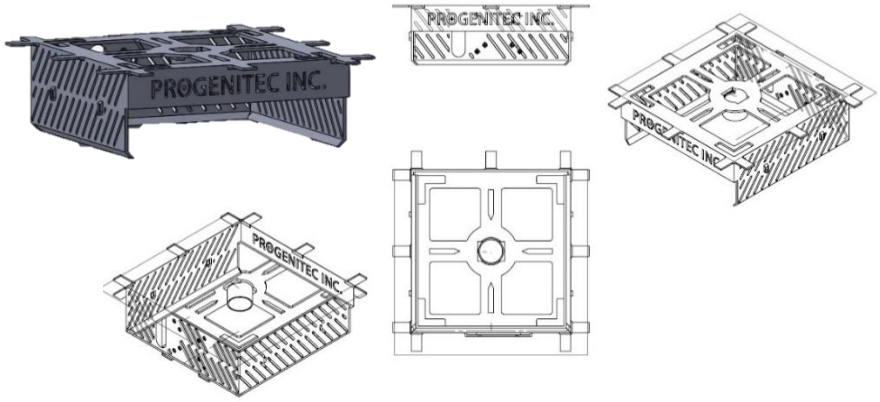

Figure 4.7. CAD rendering of R4 of the portable fluorescence imager design (top left) and technical drawing.

Most notable was the locking mechanism, which was adjusted to be more robust. This locking mechanism removed the need for aftermarket modifications to the LED matrix and interfaces directly with the frame of the light source (Figure 4.8).

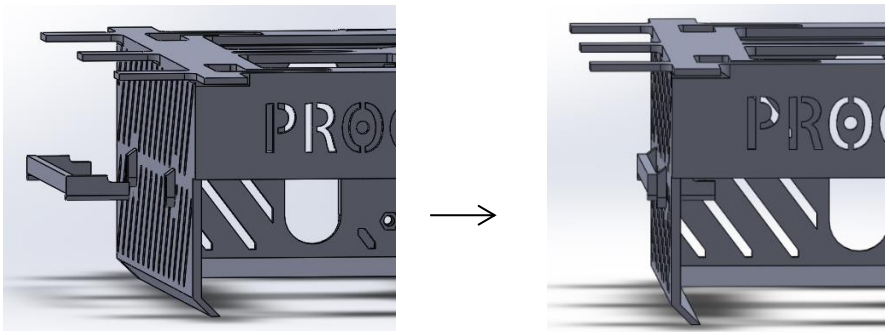

Figure 4.8. Illustration of R4 case design with slotting matrix locking mechanism.

In addition, a versatile camera mounting solution was included to allow the attachment of either a CCD or CMOS camera. A VESA mount was integrated into the design for mounting directly to any standard articulating arm. Finally, tabs were added to the top of the device to provide a greater surface area during 3D printing and decrease warping.

4.2.2. Filter Criteria

The initial imager design incorporated three 2-inch bandpass filters mounted in a manually rotatable filter wheel (Thorlabs LCFW5, Figure 4.9). A variety of bandpass filter wavelengths (Edmund Optics, 560, 710, and 810 nm) were used for use with different fluorescent dyes.

Figure 4.9. Initial filter mount solution (©Thorlabs).

While this design allowed for filters to be exchanged with relative ease, the weight and size of the design prevented this from being a viable option. The planned solution to these issues was the introduction of a motorized version of the original filter wheel design. After further investigation, it was determined that this change would not meet the two primary goals of weight and size reduction. Such an addition would also significantly increase the cost of the device. After considering several options, it was determined that a modular, easily switchable filter could be custom designed in-house to best fit the portable imager's design requirements. The CAD file for the intermediate iteration of this design is shown below in Figure 4.10.

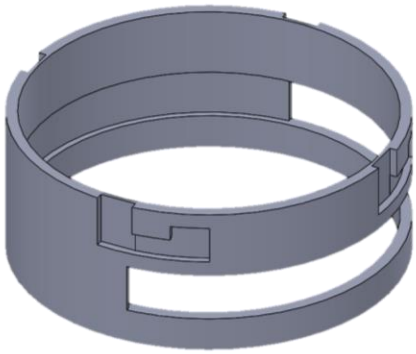

Figure 4.10. CAD model of the Preliminary R3 filter holder design.

The initial iteration of this design was found to be more advantageous in terms of size and ease of use than the initial filter ring. It interfaced directly with the revised LED ring using a simple, robust twist-locking mechanism and allowed filters to easily be exchanged in seconds (Figure 4.11).

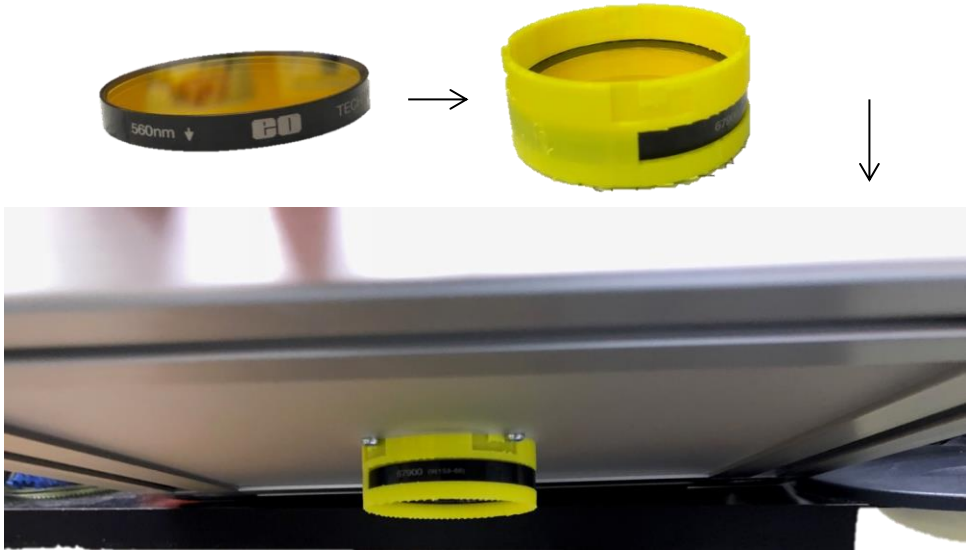

Figure 4.11. Preliminary R3 filter holder operation.

Its minimized design also allowed this component to contribute only negligible size and weight to the overall device. However, further testing revealed that it was difficult to create a perfectly closed light path with a filter inserted, allowing light leakage to occur.

To remedy this problem, the filter holder and imager case were redesigned to create a closed light path. This design allows even easier filter switching, with each filter assigned to its own enclosed case and able to be swapped in one motion without any possibility for user error in filter positioning. It is pressure-fitted in one motion into a slot on the imager and can be easily removed for exchange with another emission wavelength (Figure 4.12). It also has a capacity of up to 2 stacked filters for background reduction.

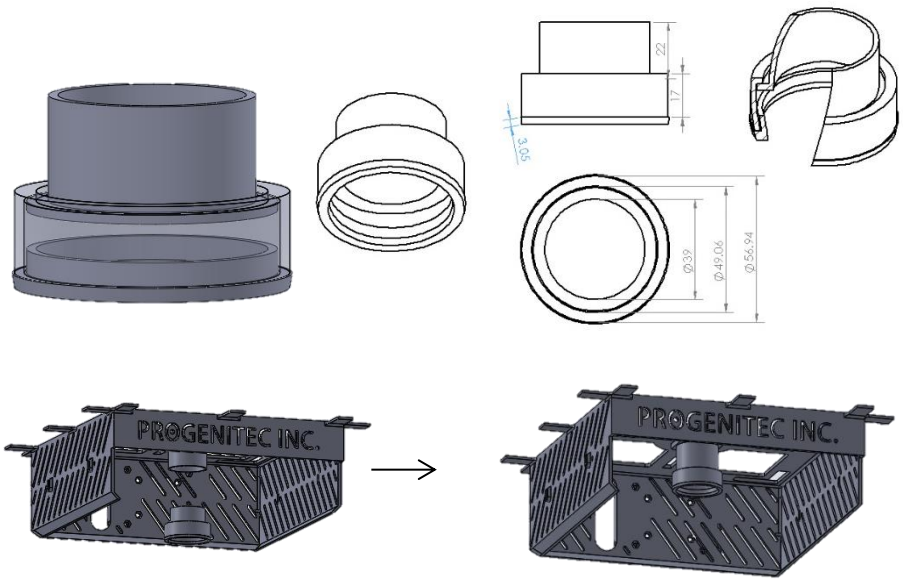

Figure 4.12. A CAD rendering and technical drawing of the final filter holder design (top). The interface of this revised filter holder design is shown interfacing in a pressure-fit mechanism with the R4 imager design.

A detailed breakdown of the operation of the final filter tube device is shown below in Figure 4.13 with final 3D printed parts.

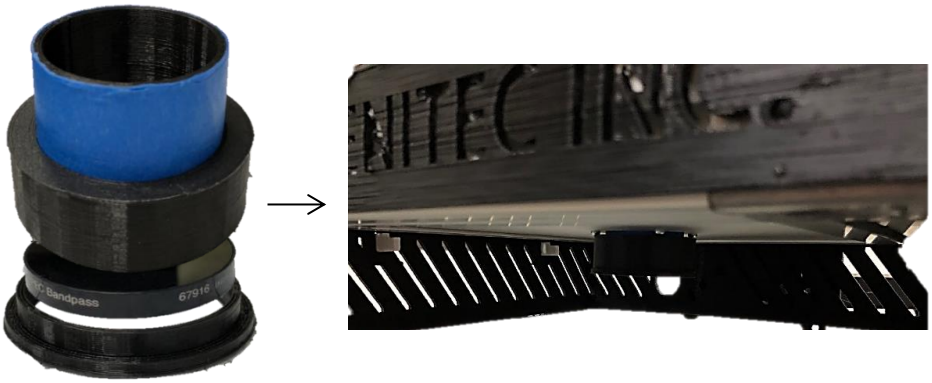

Figure 4.13. Components and installation of the final R4 filter holder design.

4.2.3. Light Source Requirements

The LED ring used as a light source in the original design of the portable imager (Figure 4.14, ProPhotonix RF2-xxx-VXF100, with xxx = 640 or 710 nm) was effective for applications requiring small fields of view, but had several drawbacks.

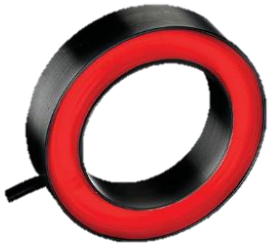

Figure 4.14. An LED ring light was the initial illumination method.

Primarily, the working distance was fixed at 4 cm due to the divergence angle of the individual LEDs. This prevented the imaging of surface areas greater

than 4 x 4 cm, preventing the study of larger samples. Collimation was initially explored for an alternative to the fixed-angle LED ring design, but it was determined that even this solution would not allow imaging of large areas (> 10 x 10 cm) with high uniformity using a LED ring setup. The maximum incident intensity was also relatively low, at 5 mW for the 630 nm excitation wavelength model. To solve these problems, several matrix designs were tested. Ultimately, a large LED matrix with a clearance port for the camera lens was selected (SmartVision RL200, Figure 4.15).

Figure 4.15. A 640 nm excitation wavelength version of the final LED matrix (© SmartVision).

This setup was found to produce high incident light intensity, high light uniformity when measured using a thermal power meter, and flexible working distance and field of view range.

4.2.4. Combination Fluorescence/Luminescence Imager

The optimized fluorescence imager was combined with the large animal luminescence imager developed in Chapter 3 to produce a handheld device capable of simultaneously imaging fluorescence and luminescence in large animal and human applications. A diagram of this design along with its CAD model is shown in Figure 4.16.

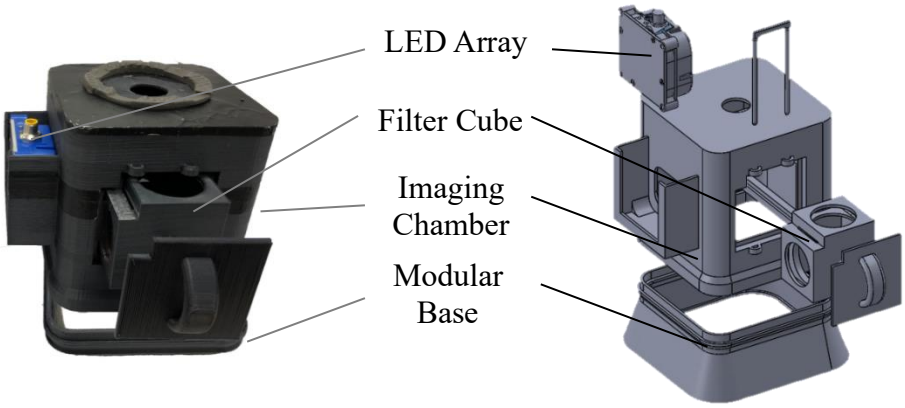

Figure 4.16. A manufactured combination fluorescence/luminescence imager is shown (left) with the corresponding CAD model (right). The major components of this device are the 3D-printed imaging chamber, LED array, and filter cube containing the emission, excitation, and dichroic filters.

4.2.4.1. Case Design

To integrate fluorescence and luminescence functionality into an open case design capable of imaging in large animals and humans, a total overhaul of the R4 case was required. In order to allow light source excitation wavelength exchange during imaging without moving the device, the light source had to be mounted outside the imaging case where it would be easily accessible. Due to the concurrent need to maintain the light isolation of the imaging chamber, on-axis

lighting (with the light source oriented parallel to the objective) would not be possible. Due to this, an external slot with a portal to the interior of the device was designed from which the light source could be inserted and removed during imaging.

Due to the off-axis nature of the lighting, it was necessary to incorporate a wider range of optical filters into the light path. To account for this, sliding guide rails were incorporated into the body of the device on which the filter cube could rest upon to hold it in place while inserted. A small locking mechanism holds the filter cube in place when inserted.

Modular bases of different heights were designed to interface with the main body of the design similar to the luminescence imager designed in Chapter 3.

4.2.4.2. Filter & Light Source Criteria

Because the new lighting scheme involves light pointed perpendicularly to the sample instead of directly at it, it was necessary to incorporate several new optical filters. This lighting reorientation also provided the opportunity to solve a problem encountered during characterization of the R4 imager: High fluorescence background. It was observed that nonspecific fluorescent signals were observed during imaging, particularly with reflective surfaces. These artifacts would commonly take the form of bright spots caused by the highly intense, direct LEDs of the LED matrix. The possible causes identified for this phenomenon were

determined to be light within the bandpass filter's range entering the bandpass filter (nonspecific light in the imaging chamber), light bypassing the bandpass filter and entering the CCD directly, and the highly direct nature of the on-axis LED matrix. All of these issues were addressed with the new filter selection, including a bandpass filter, a dichroic longpass filter, and a shortpass filter. These filters are integrated into a 3D-printed filter cube that slides via rails into the imaging chamber and is fixed in place with a locking mechanism. A diagram of the new filter placements inside the filter cube is shown in Figure 4.17.

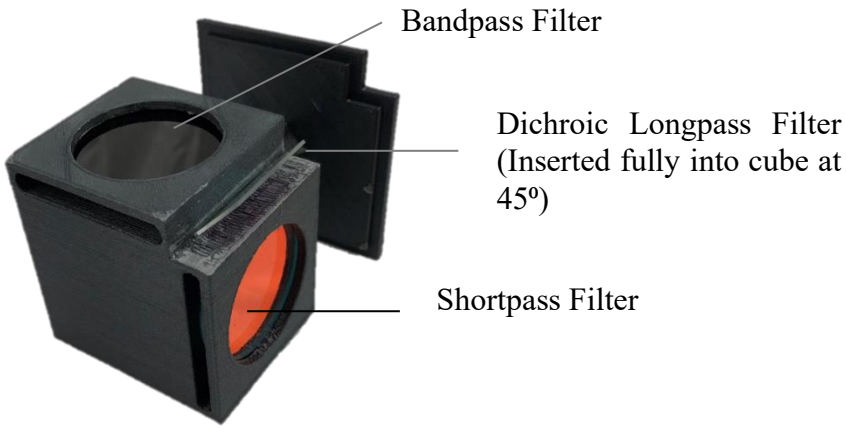

Figure 4.17. A filter cube is shown loaded with all optical components: The shortpass filter, the dichroic longpass filter, and the bandpass filter. The filter cube is loaded into the imaging chamber.

To prevent light not emitted from the sample within the bandpass filter's range from contacting the bandpass filter, a shortpass filter was fitted between the LED light source and the entrance to the imaging chamber in the filter cube. Shortpass filters only transmit light below their cutoff wavelength, preventing

higher wavelengths in the bandpass filter's range from entering the chamber and bypassing the bandpass filter.

Redirection of the light onto the sample was accomplished with dichroic longpass filters. These filters sit at a 45º angle of incidence to the excitation light beam. Light above their transmission wavelength is transmitted at 0º, while light below the transmission wavelength is reflected down at 90º to excite the sample. The higher-wavelength photons emitted from the sample are then passed back through the dichroic filter to pass through the bandpass filter and to the camera. These filters serve the dual purpose of redirecting light and removing any nonspecific (high wavelength) light in the light path away from the bandpass filter.

Two filter cubes were constructed for imaging at two separate excitation wavelengths: 640 nm and 470 nm. The 640 nm wavelength filter cube was used for NIR Cy5 imaging and consisted of a 700 nm bandpass emission filter, a 525 nm cut-off wavelength shortpass filter, and two 650 nm dichroic longpass filters. For a 470 nm excitation wavelength, a 570 nm bandpass emission filter was used in conjunction with a 675 nm cut-off wavelength shortpass filter and two 500 nm dichroic longpass filters.

For white light imaging, a filter cube loaded with only a 2- x 2-inch cold mirror was used. Cold mirrors act as dichroic mirrors described above but

transmit near infrared light and reflect visible light to illuminate the sample with white light.

The new light path setup of the Combination Imager removed the need to mount the light source around the lens of the camera, which allowed the selection of a light source without a central hole. Due to the smaller size of the new device, it was also necessary to choose a smaller light source. Finally, due to the bright spot artifacts observed when using the high-intensity, direct illumination of the LED matrix used in imager R4, a more diffuse, uniform light source was desired. These requirements were met with a small, highly diffuse, but still intense LED matrix (Figure 4.18).

Figure 4.18. The SB75, a highly diffuse 6-LED array produced by Smart Vision Lights, was used in the Combination Imager.

This LED light source was found to meet the requirements of high light intensity and uniformity while also matching the size needed for the new device.

4.2.4.3. Light Isolation

In order to isolate the imaging chamber from ambient light during luminescence imaging, compressible foam gaskets were used similarly to the imager described in Chapter 3. These gaskets were placed at all locations light could enter the chamber, including between the camera and the body of the chamber, between the chamber and the filter cube door, between the bottom of the imager and the detachable bases, and between the bases and the imaging objectives.

4.3. Design Progression

4.3.2. Fluorescence Tabletop Imager: R2

The initial black-box imager design (R1) was replaced with a similar prototype fabricated by an in-house machine shop (R2, Figure 4.19).

Figure 4.19. The second revision (R2) of the tabletop fluorescence imager is shown.

This required a variety of machining processes on polycarbonate and aluminum sheets and tubing and incurred a high manufacturing cost. To mitigate this, it was determined that 3D printing would be a viable prototyping method.

In addition, a primary goal of redesigning the initial tabletop imager design was adding new functionality. The revised design added the critical ability to exchange excitation light sources during imaging for multi-wavelength studies. It also allowed a wider range of z-axis adjustability due to the exchange of 4 enclosing legs for one adjustable stand. Because the drivers for the revised device are integrated into the black box under the imaging stage, the device also features enhanced portability.

However, several parameters remained to be optimized to further increase the imaging functionality of the fluorescence imager. First, retaining the LED ring from R1 as the light source continued to limit both the field of view of the device to 2 x 2 cm and the limits of z-axis adjustability to 3-4 cm due to the divergence angle of the LEDs discussed in Chapter 2. Also, the continued use of the large filter wheel to exchange the bandpass filters represented an unnecessary amount of size and weight and proved difficult to retain while changing the excitation light source. Further redesign of the fluorescence imager was pursued to improve upon these parameters.

4.3.2.2. Fluorescence Tabletop Imager: R3

To prototype the R3 stand-mounted portable imager design, a scaled model of the mechanical housing was 3D printed. A 2:5 version was successfully printed and assembled, shown below in Figure 4.20.

Figure 4.20. A 2:5 prototype of the R3 portable imager mechanical housing showing the slotting mechanism of the new LED light source.

A full-scale prototype of the intermediate tabletop portable fluorescence imager design was printed and assembled on a large format 3D printer. An aluminum frame was also assembled from purchased 80/20 extrusions and fixtures (Figure 4.21).

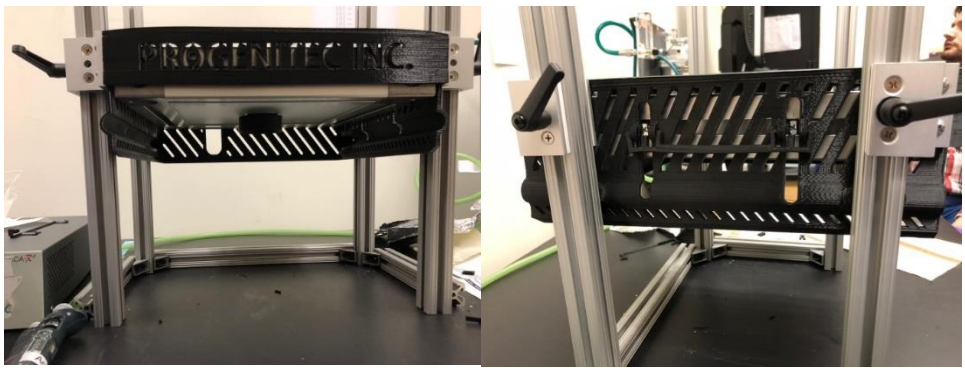

Figure 4.21. Revision 3 of the tabletop portable imager design with adjustable aluminum frame.

The transition to a larger excitation light source represented an improvement in the field of view that could be imaged. The novel locking mechanism, consisting of 3-D printed retaining clips that interfaced with bolts

affixed to the T-slotted aluminum body of the light source, allowed even the larger light source to be exchanged during imaging easily. In addition, the large filter wheel was exchanged for a custom 3D-printed bandpass filter holder that interfaced directly with the excitation light source, allowing both the light source and emission filter to be exchanged simultaneously during dual-wavelength studies. Due to the increased size of the new light source, the field of view of the revised device was also increased.

Some usability issues remained with this revision of the imager design. The locking mechanism was difficult to operate with only one person, as both clips had to be removed at the same time while also supporting the LED matrix to prevent it from disengaging prematurely. It was also determined that a "floating" design mounted on an articulating arm would make the device more practical for animal studies. These improvements were addressed in the final revision of the fluorescence imager.

4.3.2.3. Fluorescence Tabletop Imager: R4

The final portable fluorescence imager design (R4) was 3D printed as one component and mounted on an articulating arm (Figure 4.22).

Figure 4.22. The R4 version of the 3D printed portable fluorescence imager design with CMOS camera and LED matrix mounted on an articulating arm.

The 3D-printed case integrates all necessary imaging components into a compact package. The revised design also allows the LED matrix to be exchanged by one person with the revised clip system that interfaces directly with the LED matrix. Additionally, the final revision of the fluorescence imager is cart-mounted to allow easy transport of the devices with a laptop for image acquisition and processing. While a tripod design was initially proposed, the large footprint, lack of stability, and necessity for a counterweight to offset top-heavy imaging components made a wheeled cart a more practical option. An example of this setup is shown below in Figure 4.23.

Figure 4.23. Example of the cart mounted R4 fluorescent (left) and luminescent (right) imaging devices. The articulating arm is fingertip-adjustable for ease of positioning.

This cart-mounted design allows for increased versatility when compared with a tabletop imager. In large animal studies, the cart and articulating arm can be used to both easily transport all imaging equipment to the animal procedure room and to quickly place the imager in the necessary position for image acquisition.

This design added much of the desired functionality lacking in the first revision of the tabletop imager described in Chapter 2. However, the ultimate goal of the work described here was the development of a combination optical imaging device capable of imaging both fluorescence and luminescence robustly in a clinical or large animal setting. It was determined that accomplishing this would necessitate combining the luminescence imaging light isolation strategy developed in Chapter 3 with the fluorescence imagers described above. This combination device is described below.

4.3.2.4. Final Combined Luminescence/Fluorescence Imager Design

The final imager developed in this work is a combination luminescence/fluorescence imaging device (Combination Imager) combining key characteristics of the luminescence and fluorescence imagers described previously. An image of the assembled device is shown in Figure 4.24.

Figure 4.24. The fully assembled final combination luminescence/fluorescence imager is shown.

The optical components of fluorescence imaging, including a high-intensity LED matrix and several optical filters, are combined with the foam gasket light insulation strategy of the luminescence imager described in Chapter 3. While this device is capable of *in vitro* and small animal imaging, its primary accomplishment is its ability to integrate these two powerful optical imaging modalities into a portable imaging chamber that can be used in large animal and

clinical imaging. A table summarizing the optical functionality of these devices compared to the Kodak imager is shown in Table 4.1. Comparison of imaging functionality of the commercial standard with the imaging devices developed in this work..

Table 4.1. Comparison of imaging functionality of the commercial standard with the imaging devices developed in this work.

Imaging Specification	**Kodak Imager**	**Fluorescence/ Luminescence Imager: Revision 1**	**Luminescence Imager**	**Combination Imager**
View Area	7 x 7 cm	2 x 2 cm	10 x 10 cm	7 x 7 cm
Dual Wavelength Functionality	Full	Partial	None	Full
Portability	Low	Medium	High	High
Level of Enclosure	Total	Partial	Open	Open
Large Animal Imaging Functionality	No	No	Yes	Yes
Luminescence Functionality	Yes	Darkness Only	Yes	Yes
Fluorescence Functionality	Yes	Yes	None	Yes
Size	104 × 61 × 96.5 cm	22 × 22 × 25 cm	22 x 18 x 13 cm	25 x 19 x 15 cm
Weight	142 kg	5.8 kg	2.7 kg	4.2 kg

4.4. Materials and Methods

4.4.1. Materials

A CCD camera was used for image acquisition (C10600, Hamamatsu) with a F1.4/12 mm lens (HR961NCN, Navitar). A CMOS camera (Manta G-145B NIR, Allied Vision) was exchanged for the CCD camera for select fluorescence studies. For Revision 2 of the tabletop fluorescence imager (R2), the several components were retained from Revision 1. These included the LED driver (DCZ100) and 60 mm cage system filter wheel (LCFW5) purchased from Thorlabs. Two-inch diameter thin-film 700±2 nm and 810±2 nm near-infrared filters (67-905, 67-916) obtained from Edmund Optics were loaded into the filter wheel. The 630±10 nm and 740±10 nm LED ring lights obtained from ProPhotonix were also used (RF2-630-VXF100). The portable imager housing was constructed using in-house laser-cut 5 mm thickness black polycarbonate, 1-inch diameter aluminum pipe with 0.5 cm holes drilled every cm for z-axis adjustability, and a welded aluminum plate that both supports the base of the polycarbonate and interfaces with the z-axis via heavy-duty bolts. All machining was provided by the Mechanical and Aerospace Engineering Machine Shop at the University of Texas at Arlington.

To construct Revision 3 of the tabletop imager (R3), the manufacturing method was changed from utilizing traditional machine shop facilities to rapid prototyping using 3D printing. The imaging case was designed in Solidworks CAD and 3D printed on a commercially available large-format 3D printer (gMax 1.5+, gCreate) using black polylactic acid (PLA, Hatchbox). Z-axis adjustability

was accomplished by constructing a stand with using aluminum extrusions and sliding fixtures procured from 80/20 Inc. A new light source format was also used, with large 625 and 730 nm wavelength LED matrices procured from Smart Vision Lights (RL200-625, RL200-730).

Revision 4 (R4) of the fluorescence imager design was manufactured using 3D printing in a similar way to R3. Instead of mounting the imaging case on a tabletop stand, however, this design was designed to be mounted onto an articulating arm (IOP136 800-104-FM, Human Solution) integrated into a wheeled cart (WB113116, Global Industrial).

The final combined fluorescence/luminescence imager was also manufactured using 3D printing, but 30% carbon-fiber reinforced PLA was used as the material (PLA-1.75-C-B, ZIRO). In addition, several optical components were added. The large-format LED matrices from R3 and R4 were exchanged for more compact matrices in 625 and 470 nm wavelengths (SB75-625 & SB75-470, Smart Vision Lights). Shortpass and dichroic longpass filters were also added to the bandpass filters previously described for each wavelength. For a 625 nm excitation wavelength, a two-inch diameter thin-film 700±2 nm bandpass emission filter was used in conjunction with a 2-inch 525 nm cut-off wavelength shortpass filter and two 650 nm dichroic longpass filters (67-905, 64-613, & 69-902, Edmund Optics). For a 470 nm excitation wavelength, a two-inch diameter thin-film 570±10 nm bandpass emission filter was used in conjunction with a 2-inch 675 nm cut-off wavelength shortpass filter and two 500 nm dichroic longpass

filters (57-901, 64-610, & 69-899, Edmund Optics). For white light imaging, a 2-x 2-inch cold mirror was used instead of the dichroic mirrors (20CMS-45, Newport). In a similar way to the luminescence imager described in Chapter 3, compressible polyurethane (PU) and polyethylene (PE) foam were used for light isolation in luminescence studies (McMaster-Carr).

4.4.2. Device Characterization: R4

4.4.2.1. Light Source Intensity

The maximum intensity of a large LED matrix's illumination was characterized using a thermal power meter. The results were compared with the maximum reading of the LED ring used in Generation 1 as well as the Kodak.

4.4.2.2. Beam Uniformity

The homogeneity of light distribution at different distances from the central maximum was quantified as described using a thermal power meter. The power meter was placed at increasing radial locations from the center of the field of view and the intensity was recorded. Homogeneous field of illumination (FOI) was defined as the area within which uniformity is > 0.9 as described in Section 2.4.1.1. This was repeated at different distances to determine the minimum and maximum FOI and optimum working distance.

4.4.2.3. Camera Sensor Format

Cameras with two different sensor platforms were investigated: CCD (charge coupled device) and CMOS (complementary metal oxide semiconductor). These

technologies have several important differences; most notably, CMOS's elimination of bloom and smear artifacts due to more complex noise elimination architecture and lower cost than CCD, and the CCD's capacity for higher exposure times.[99] To investigate the suitability of each device for both luminescence and fluorescence imaging, Study 2.3.5.1 was repeated using each camera according to the protocol described in the above section. The goal of this study was to use the CMOS camera in further fluorescence imaging if it was demonstrated to have equivalent limits of detection and sensitivity in fluorescence imaging to the CCD camera. It was hypothesized that the CMOS camera would produce statistically indistinguishable limits of detection and sensitivities in fluorescence studies when the values produced by both imagers were compared with a two-tailed Student's t-test.[100]

4.4.2.4. Light Isolation

Elimination of ambient light is critical in avoiding background noise. In the initial portable imager design, a blackout fabric light shield could be attached via integrated clips. The light shield could also be easily detached from the front of the device for subject positioning, light source exchange, or readjustment. This design was tested for practicality in fluorescence studies. Study 2.3.5.1 was repeated for differ ambient lighting conditions: Full ambient light, with light shielding using a full blackout fabric light shield enclosure (10% ambient light), partial light shield enclosure (50% ambient light), and in a completely dark room. It was hypothesized that the developed light shield would produce statistically

undistinguishable results from imaging in darkness when the studies were compared with a two-tailed Student's t-test.

4.4.3: Device Characterization: Combined Luminescence/Fluorescence Imager

4.4.3.1. Light Source Intensity

The maximum intensity of the Combination Imager's light source was characterized using a thermal power meter at 640 and 470 nm wavelengths. These values were compared with the R4 design's large LED and the Kodak.

4.4.3.2. Fluorescence Background

Fluorescence background during fluorescence imaging was analyzed. During testing with the R4 imager, it was determined that nonspecific fluorescent signals were recognized by the camera. To confirm that this issue had been resolved with the Combination Imager, Study 2.3.5.1 was repeated with the new imaging device and background signals were quantified using 2-fold serial dilutions of NIR Cy5 (0.5, 0.25 0.125, 0.0625, 0.03125, 0.015625, 0 ug/mL). To confirm that other wavelengths would also not produce high backgrounds, a study similar to Study 2.3.5.1 was conducted with the fluorescent dye Fluorescein isothiocyanate (FITC). Briefly, a stock solution of FITC was prepared in acetone at a concentration of 1 mg/mL. Two-fold serial dilutions were then made down to 0.015625 mg/mL (1, 0.5, 0.25 0.125, 0.0625, 0.03125, 0.015625, 0 mg/mL FITC). Two hundred µL of each concentration in triplicate was then added to wells of a 96-well plate and imaged using the FITC filter cube and excitation light source. Background signals were then quantified. It was hypothesized that both

wavelengths would produce a background reading significantly lower than the R4 imager and statistically undistinguishable from the Kodak imager at corresponding wavelengths upon analysis with a two-tailed t-test.

4.4.3.3. White Light Resolution

The white light image resolution of the Combination Imager was compared with the Kodak. To quantify this, matrices of text with font sizes ranging from 7.84 to 0.35 mm were printed on white paper. Images were acquired of the text matrix using the Combination Imager and Kodak with their white light settings. The images were then processed in ImageJ by applying a threshold of 96 ± 3% and identifying the smallest legible text. Resolution was defined as the smallest possible text that each imager could quantify.

4.4.3.4. MATLAB Image Processing

In preliminary tests with the Combination Imager, a gradient in excitation light was observed. Since this was only observed in studies including dichroic filters, it was determined that the 45º angle of incidence of excitation light on the dichroic longpass filter was responsible. Since this gradient was observed to be consistent across different distances for each light wavelength, an image processing filter was developed in MATLAB to correct for the gradient. The image processing code allows the user to select an image and applies a correcting filter in the x- and y-directions. The resulting image is then saved as a .tif file for further analysis in ImageJ and Excel. An example of NIR Cy5 calibration curves produced according

to Section 2.3.3.1 analyzed before and after the correction is shown in Figure 4.25.

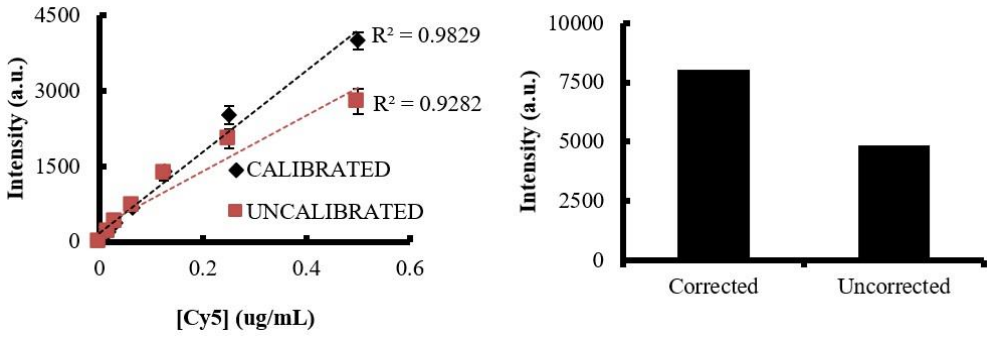

Figure 4.25. NIR Cy5 calibration curves were analyzed before and after image processing in MATLAB. It was determined that filtering in MATLAB was able to correct for the intensity gradient produced by the 45º angle of the dichroic longpass filters, increasing both the linearity and sensitivity values produced by the curve.

This method of image processing was found to produce significantly more homogeneous light coverage and highly linear calibration curves. All results presented below were produced from images analyzed using this method.

4.4.3.5. Beam Uniformity

Beam uniformity of the Combination Imager was analyzed at both 640 and 470 nm. For 640 nm, 30 mL of 5 ug/mL NIR Cy5 in DI water was poured into a flat, clear 115 x 130 mm container. Images were then acquired using the NIR Cy5 filter cube and light source on the Combination Imager. This study was repeated at different distances. To determine the uniformity of the Combination Imager at 470 nm, the previous steps were repeated with 1 mg/mL FITC in 80% acetone. For both wavelengths, the uniform area at each distance was quantified,

determined as the largest continuous area with the highest uniformity (defined as percentage of maximum intensity value).

4.4.3.6. Working Distance Optimization

To determine the optimum working distance of the Combination Imager, calibration curves for NIR Cy5 and fluorescent FITC dye were constructed and imaged as described in Study 4.3.4.3 and repeated for each distance setting of the imager. The distance that produced the highest sensitivity and lowest limit of detection as described in Section 2.3.3.1 was selected as the optimum distance for each wavelength and was used in subsequent studies.

4.4.3.7. Light Isolation

Similar to the luminescence imaging device developed in Chapter 3, it was necessary to prove the light isolation of the Combination Imager in an ambiently lit room. Study 3.3.2.1 was repeated with the new imaging device. The new imaging device was compared with the device developed in Chapter 3, as well as with the Kodak imager and complete darkness. It was hypothesized that the new imager would produce statistically indistinguishable results from the Kodak and imaging in total darkness when an unpaired 2-tailed t-test was applied.

4.4.4. In Vitro Studies

4.4.4.1. Beam Homogeneity Imager Comparison: 640 nm

Beam uniformity of the Combination Imager was compared with the R4 and Kodak imagers. The protocol described in Section 4.4.3.5 for NIR Cy5 was

repeated for each imaging device. It was hypothesized that the Combination Imager would produce a homogeneous FOV of approximately the same size and uniformity of the Kodak imager and greater than the R4 imager.

4.4.4.2. Beam Homogeneity Imager Comparison: 470 nm

Beam uniformity of the Combination Imager was compared with the R4 and Kodak imagers. The protocol described in 4.4.3.5 for FITC was repeated for each imaging device. It was hypothesized that the Combination Imager would produce a homogeneous FOV of approximately the same size and uniformity of the Kodak imager and greater than the R4 imager.

4.4.4.3. Fluorescence Limit of Detection and Sensitivity Imager Comparison: Cy5

The sensitivity and limit of detection of the Combination Imager's ability to detect NIR Cy5 dye *in vitro* was compared to the R4 imager and the Kodak. A NIR Cy5 calibration curve was constructed and imaged according to the protocol in Section 2.3.3.1. Sensitivity and limit of detection were compared for all imaging devices. To determine if the new imaging device could produce a statistically comparable curve to the Kodak imager, the Kodak's 16-bit values were scaled to 12-bit values as described in Section 2.3.3.1 for comparison with the Combination Imager and a paired 2-tailed t-test was used to compare calibration curve values. It was hypothesized that the new imager would produce statistically similar results to the Kodak imager.

4.4.4.4. Fluorescence Limit of Detection and Sensitivity Imager Comparison: FITC

The sensitivity and limit of detection of the Combination Imager's ability to detect FITC *in vitro* was compared to the R4 imager and the Kodak. A FITC calibration curve was constructed and quantified according to the protocol in Study 4.3.4.3. Sensitivity and limit of detection were compared across the imaging devices. To determine if the new imaging device could produce a statistically comparable curve to the Kodak imager, the Kodak's 16-bit values were scaled to 12-bit values as described in Section 2.3.3.1 for comparison with the Combination Imager and a paired 2-tailed t-test was used to compare calibration curve values. It was hypothesized that the new imager would produce statistically similar results to the Kodak imager.

4.4.4.5. Luminescence Limit of Detection and Sensitivity Imager Comparison

The sensitivity and limit of detection of the Combination Imager's ability to detect L-012 luminescence was compared to the R4 imager and the Kodak. A l-012 calibration curve was constructed and quantified according to the protocol in Study 2.4.2.2 with 3-fold serial dilutions of H_2O_2 (150, 50, 16.7. 5.6, 1.85, 0.617, and 0.206, 0 mM H_2O_2). Sensitivity and limit of detection were compared across the imaging devices. To determine if the new imaging device could produce a statistically comparable curve to the Kodak imager, the Kodak's 16-bit values were scaled to 12-bit values as described in Section 2.3.3.1 for comparison with the Combination Imager and a paired 2-tailed t-test was used to compare

calibration curve values. It was hypothesized that the new imager would produce statistically similar results to the Kodak imager.

4.4. Results

4.4.1. Device Characterization: R4

4.4.1.1. Light Source Intensity

With the large-format LED rings used in Revision 4, intensities of up to 20 mW are possible – four times the maximum of the LED ring and several times higher than the Kodak machine's maximum. A comparison of these intensities for the 625 nm wavelength setting for each device is shown below in Figure 4.26.

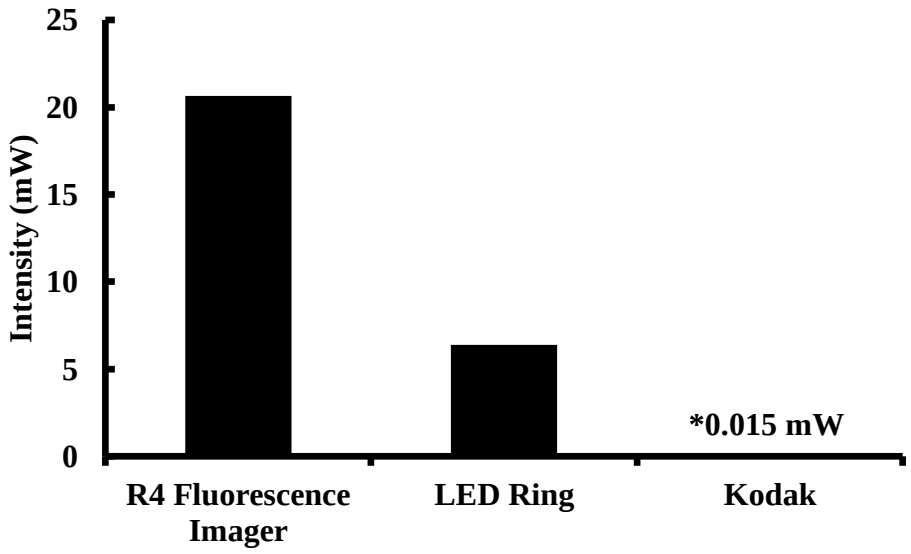

Figure 4.26. A comparison of maximum light intensities produced by different light sources at 625 nm. The final matrix design achieves intensities of almost 20 mW.

This allows for much shorter exposure times, which is especially critical for *in vivo* studies in a laboratory or clinical imaging scenario.

4.4.1.2. Beam Uniformity

The power produced by the LED matrices at different distances (15.5, 17.5, 19.5, 21.5, and 23.5 cm) from the objective was measured at increasing radial distances from the center of the field of view with a thermal power meter. The homogeneous field of view, defined as the largest continuous area where the intensity does not drop lower than 90% of the maximum, was observed for each distance. The results for the 640 nm matrix are shown in Figure 4.27.

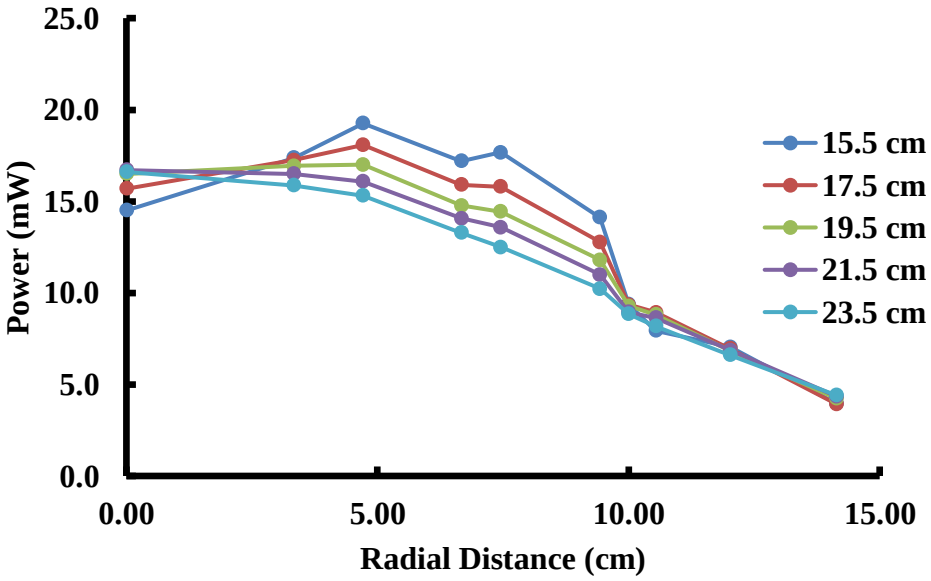

Figure 4.27. The homogeneity of the light source was observed at different distances. Based on the thermal intensity distribution, it was determined that 21.5 cm was the optimal working distance of the device.

At distances below 19.5 cm, the intensity in the center of the field of view was observed to be lower than the intensity at the edges. The field of view was seen to be most homogeneous at 21.5 cm, with a field of illumination greater than 90% of approximately 10 x 10 cm.

This study was repeated for 730 and 470 nm wavelengths at this distance (Figure 4.28).

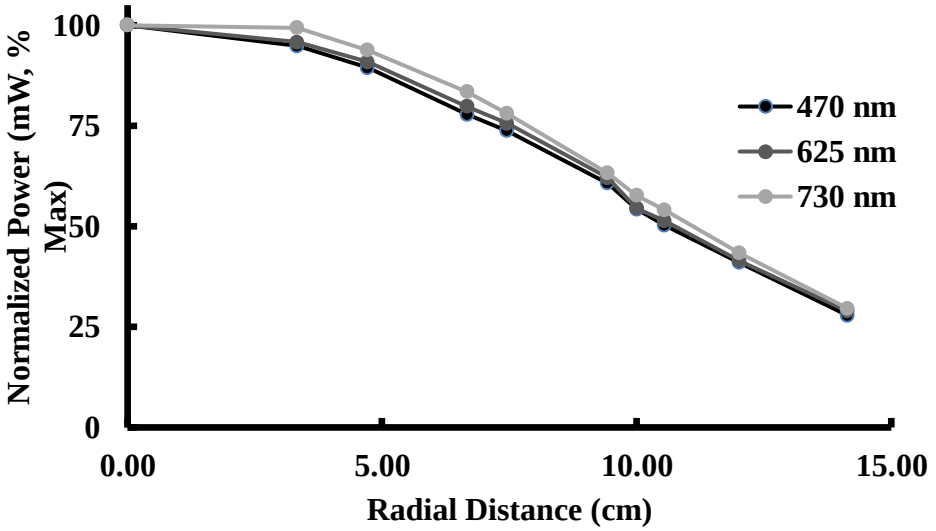

Figure 4.28. Normalized power for LED matrices of different wavelengths. A uniform area of approximately 10 x 10 cm was observed with a thermal power meter for all models.

The R4 imager was found to produce the widest homogeneous field of view at a distance of a maximum field of view with greater than 90% uniformity of approximately 10 x 10 cm at the optimal working distance of 21.5 cm for each wavelength. This represented a significant improvement to the 2 x 2 cm homogeneous view area of the R1 imager. This distance was used in all further fluorescence studies with the R4 imager.

4.4.1.3. Camera Sensor Format

The effect of using a camera with a different sensor format was investigated using a NIR Cy5 calibration curve (Figure 4.29).

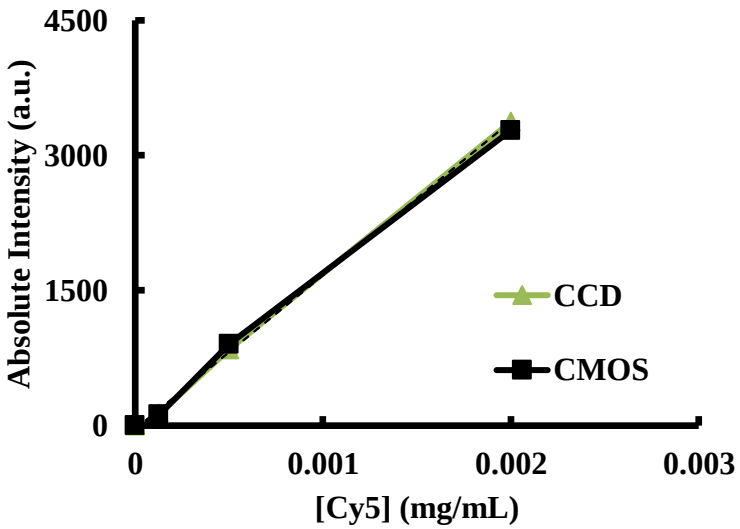

Figure 4.29. The ability of the CCD to quantify fluorescent signals was compared with a CMOS camera. It was determined that the CMOS camera produced equivalent results and was used in further fluorescence studies involving imager R4.

The CMOS camera was found to produce indistinguishable results from the CCD camera. The CMOS camera has several practical advantages, including a smaller size, reduced cost, and onboard driver. The CMOS camera was not tested in luminescence studies due to its restriction in exposure time to 1 minute. Based on these results, the CMOS camera was used in further fluorescence studies conducted by the R4 imager.

4.4.1.4. Light isolation

The effect of ambient light on the ability of the R4 image to quantify fluorescent signals was studied to confirm the sufficiency of the fabric light shield (Figure 4.30).

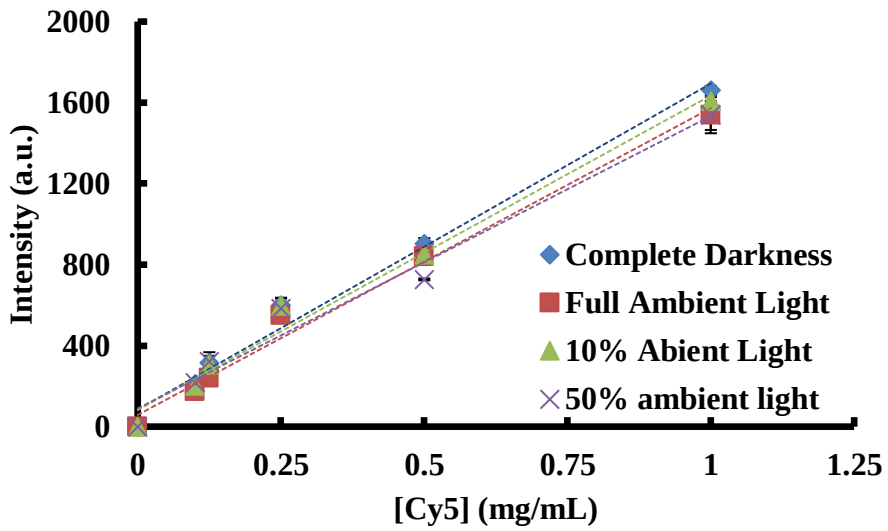

Figure 4.30. Ambient light was found to have no effect on the intensity values obtained on the sensitivity of a calibration curve of NIR Cy5 in a 96-well plate.

There was found to be no significant difference between calibration curves constructed with no ambient light versus with a blackout fabric light shield. In addition, even a lack of a light shield with full ambient light was not found to affect the signal. This is due to the high excitation light intensity and the relatively low percentage of near-infrared light in white light.

4.4.2. Device Characterization: Combined Luminescence/Fluorescence Imager

4.4.2.1. Light Source Intensity

The maximum intensity of the Combination Imager was quantified using a thermal power meter at 640 and 470 nm wavelengths. The results, compared with the R4 imager and the Kodak, are shown for 640 and 470 nm wavelengths in Figure 4.31 and Figure 4.32 respectively.

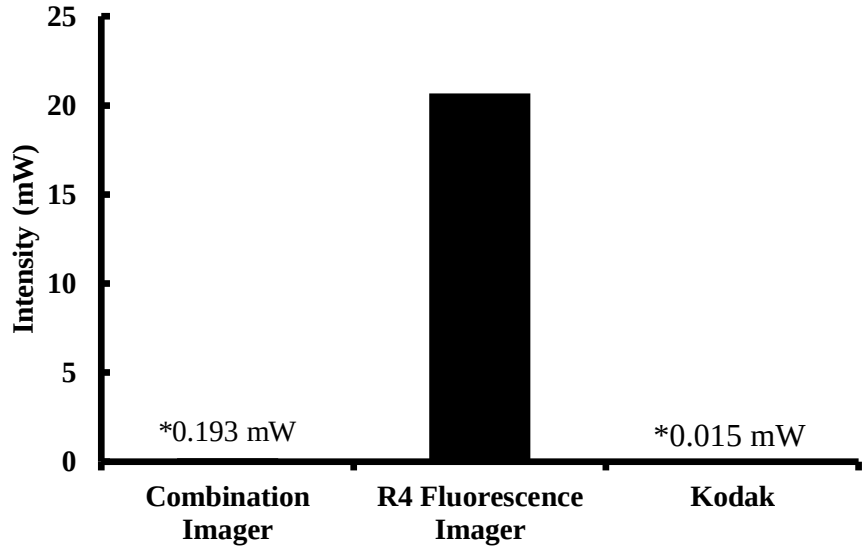

Figure 4.31. Maximum thermal intensity values for near-infrared 640 nm wavelength light settings are shown. While the R4 imager was found to have significantly higher intensity than the Combination Imager or Kodak, the Combination Imager produced a maximum intensity an order of magnitude higher than the Kodak.

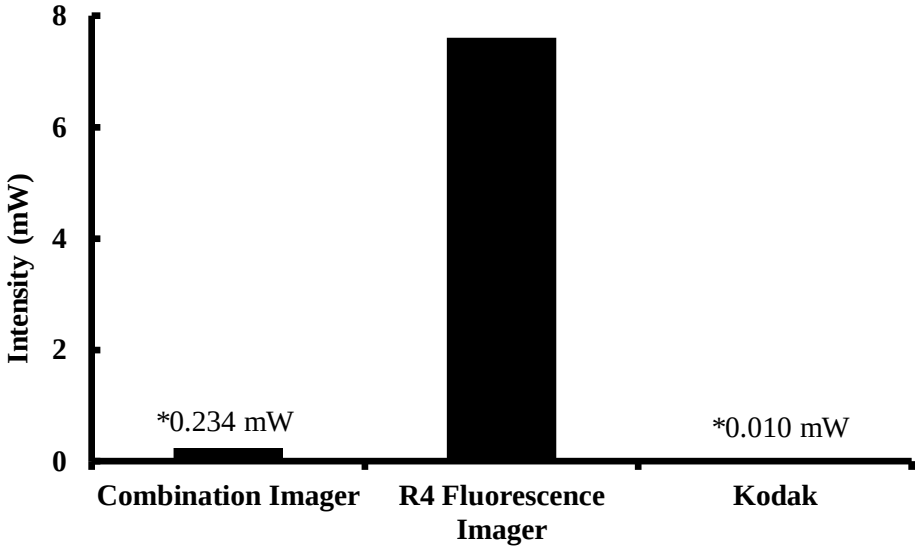

Figure 4.32. Maximum thermal intensity values for 470 nm wavelength light settings are shown. Similar to the 640 nm readings, the 470 nm light source of the R4 imager produced very high readings, with the Combination Imager producing intensities 20 times those of the Kodak.

The Combination Imager produced a significantly lower wavelength than the R4 imager. This is likely due to a combination of the addition of 2 more optical filters to the light path, which each reduce the light intensity. Because a primary goal of moving to an off-axis illumination method was to reduce bright spots in fluorescence images due to the bright, direct LEDs of the LED matrix, this outcome was expected. The device was still able to produce intensity 10-20 times higher than the Kodak. This level of excitation intensity was therefore found to be acceptable.

4.4.2.2. Fluorescence Background

The background produced by all imaging devices during common fluorescence imaging scenarios was analyzed. Results for NIR Cy5 are shown in Figure 4.33.

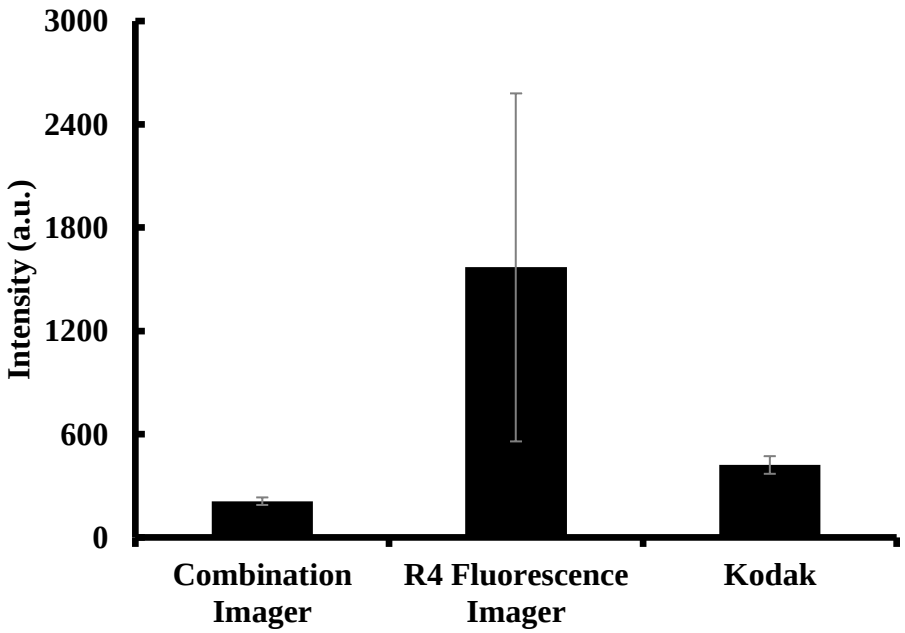

Figure 4.33. Average background intensity readings for Cy5 dye are shown. The Combination Imager was found to produce significantly lower background intensity than the R4 and Kodak imagers.

The average background intensity for the combination imager was found to be approximately 5 times lower than the R4 imager and statistically lower ($P = 0.047$). It was also found to produce background 1.5 times lower than the Kodak ($P = 0.0002$).

Background readings for the FITC calibration curve study are shown in Figure 4.34.

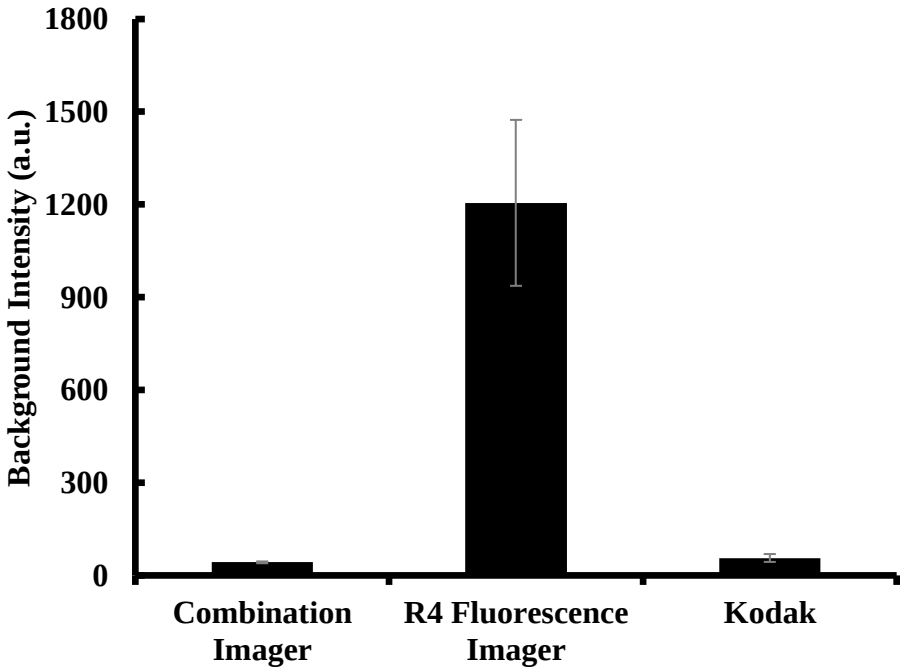

Figure 4.34. Average background intensity readings with an excitation wavelength of 470 nm and an emission wavelength of 540 nm are shown.

When compared to the R4 imager, the Combination Imager was found to produce 10 times less fluorescent background (P = 2.4e-7). When compared to the Kodak imager, the Combination Imager was found to produce slightly lower background readings (P = 0.01). Combining the results of these studies, it is clear that the design changes implemented in the Combination Imager were able to successfully reduce high fluorescence background observed in the R4 imager. This reduction also allowed the Combination Imager to produce background readings lower than the Kodak, showing that the new imager is capable of performing equivalently to or higher than the industry standard in this area.

4.4.2.3. White Light Resolution

The resolution of the portable imager's white light image setting was compared with the Kodak's by determining the smallest legible font size for each imaging device. The results are shown in Figure 4.35.

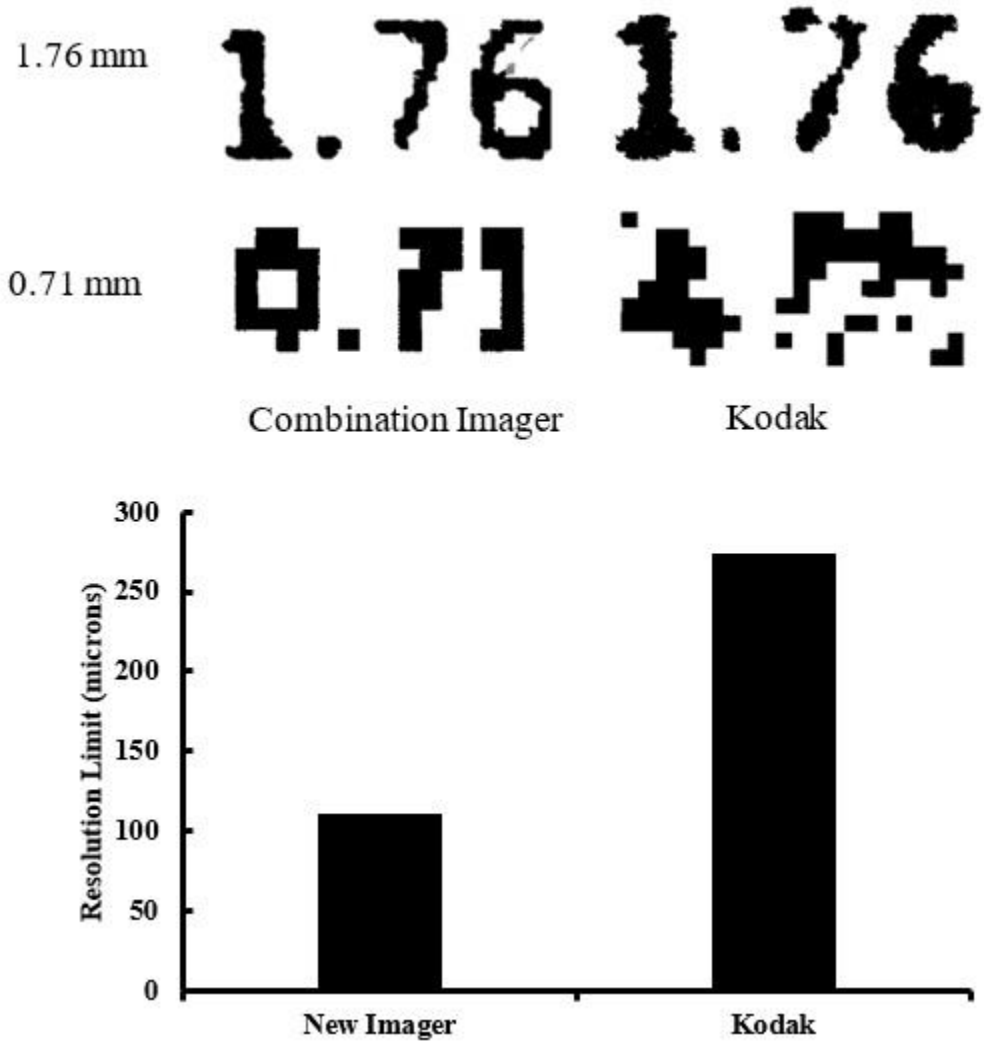

Figure 4.35. The portable imager was able to detect characters with a height of 110 microns legibly, compared to 274 microns for the Kodak. Samples of the smallest legible font size are shown above.

The portable imager was found to legibly image characters as small as 110 microns in height, almost 2.5 times lower a white light resolution limit than the Kodak. This is a symptom of the overall poor quality of the Kodak's white light images and highlights another practical imaging advantage of the Combination Imager.

4.4.2.4. Beam Uniformity

Beam uniformity, as well as the size of the field of view area, for the Combination Imager was analyzed at each distance setting for NIR Cy5 and fluorescent FITC wavelengths. The results for NIR Cy5 are shown below in Figure 4.36.

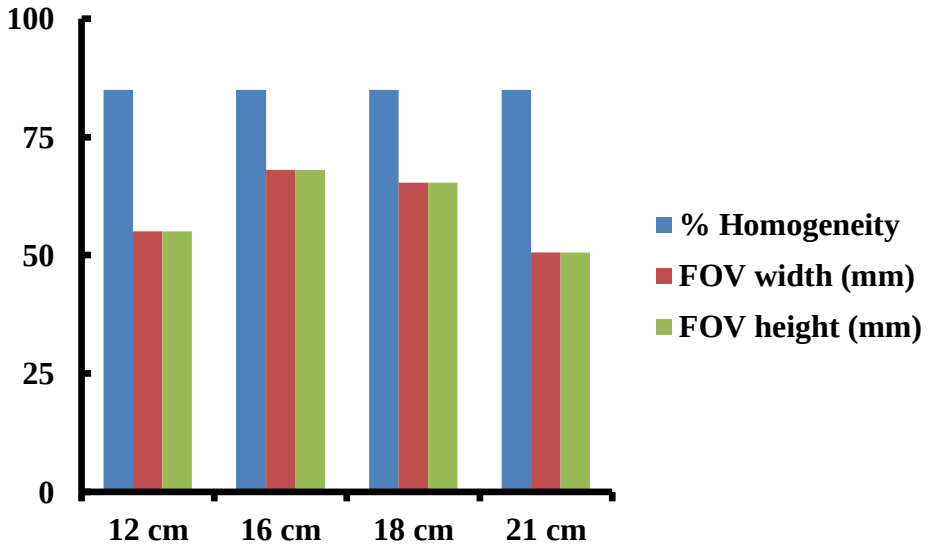

Figure 4.36. The Combination Imager was able to produce 85% homogeneous FOVs at each distance at a 640 nm excitation wavelength, with the 16 cm distance producing the widest FOV at almost 70 x 70 mm.

The Combination Imager was found to produce 85% homogeneous FOVs of over 50 x 50 mm at all distances. The 16 cm distance was found to produce the

largest FOV at almost 70 x 70 mm, representing almost double the view area of the R1 imager.

The FOV and homogeneity results for the FITC wavelength at different distances for the Combination Imager are given in Figure 4.37.

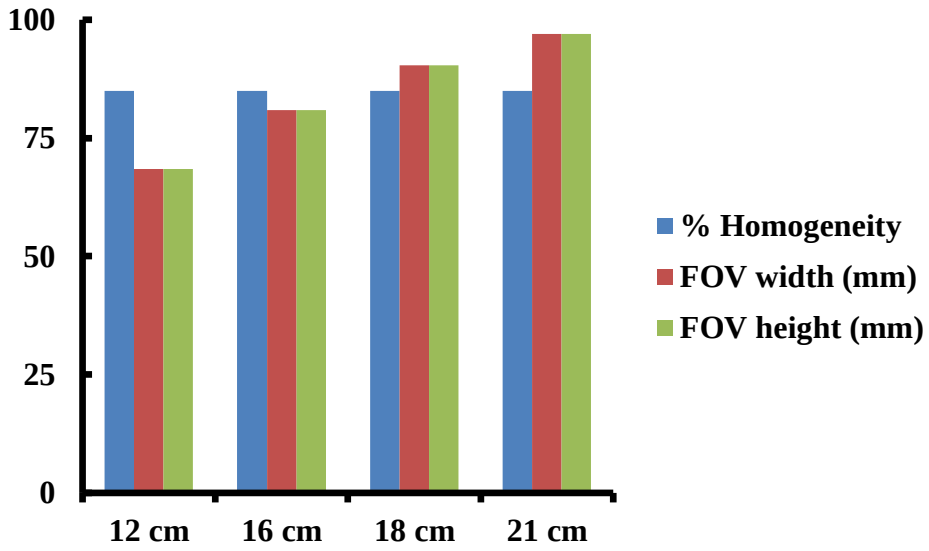

Figure 4.37. At a 470 nm excitation wavelength, the Combination Imager was able to produce 85% homogeneous FOVs at each distance, with the widest FOV at almost 100 x 100 mm observed at a distance of 21 cm.

Similar to the results obtained using NIR Cy5, all distances produced uniform FOVs of 85% homogeneity. Wider overall FOVs were observed for this wavelength, ranging from approximately 65 x 65 mm to almost 100 x 100 mm at 21 cm. This increase in homogeneity could be due to several factors, including improved homogeneity of the light source itself. These results indicate a significant improvement in homogeneous FOV from the initial R1 design.

4.4.2.5. Working Distance Optimization

It was necessary to determine the optimum distance of the Combination Imager for further studies. To do this, homogeneity results described above were integrated with differences in sensitivity and limit of detection between different distances for NIR Cy5 and fluorescent FITC wavelengths. Results for the NIR Cy5 calibration curve at different distances are shown in Figure 4.38, while FITC results are shown in Figure 4.39.

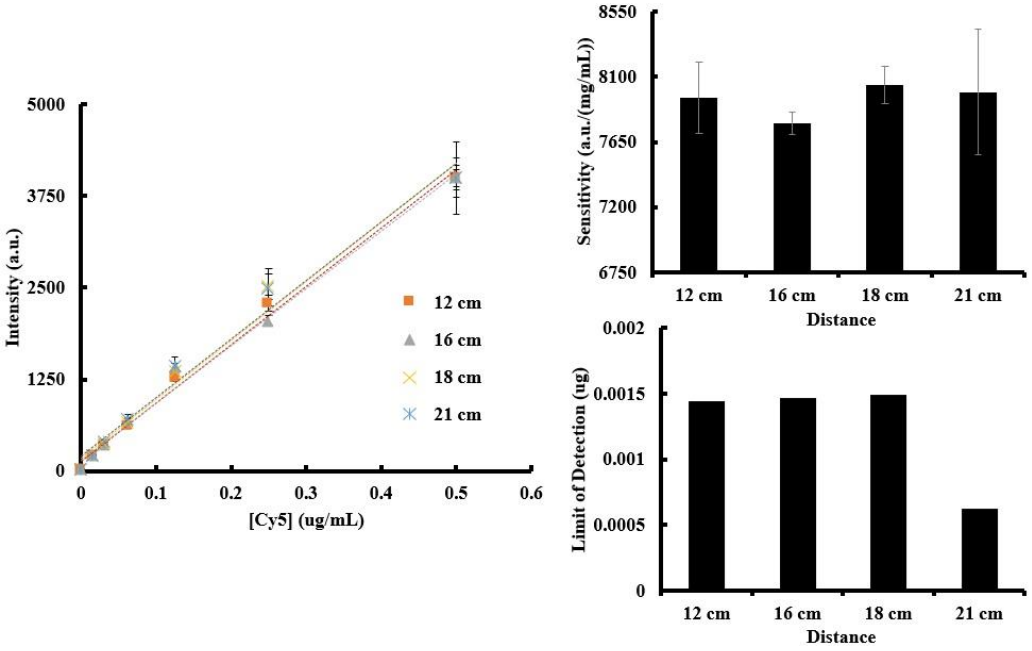

Figure 4.38. Sensitivity and limit of detection were not found to be strongly correlated with distance for NIR Cy5, with no large difference caused by a change in distance. The 18 cm was found to produce a good balance between high sensitivity, low limit of detection, and high homogeneous view area.

Imager distance was not found to have a strong effect on NIR Cy5 sensitivity or limit of detection. Eighteen cm was chosen as the optimal distance for this wavelength due to a combination of wide homogeneous field of view (65

x 65 cm), slightly higher sensitivity than other distances (8000 $\frac{a.u.}{ug/mL}$), and reasonable limit of detection (0.0015 ug/mL).

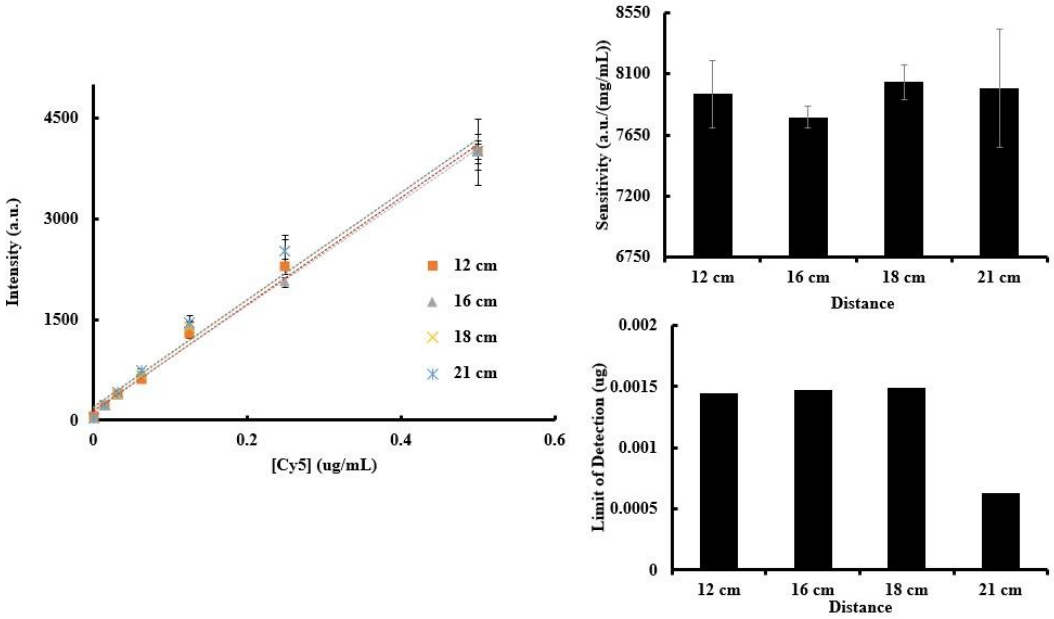

Figure 4.39. Sensitivity and limit of detection were observed to improve with decreased distance for FITC. Despite its relatively low homogeneous view area, 12 cm was chosen as the optimal distance for this wavelength due to its robust sensitivity and limit of detection.

In contrast to the trend observed with NIR Cy5, decreasing imager distance was found to improve FITC sensitivity and limit of detection. Although 12 cm has a relatively low homogeneous FOV (70 x 70 cm), it was chosen as the optimal distance for this wavelength because of its high sensitivity (12000 $\frac{a.u.}{mg/mL}$), and reasonable limit of detection (0.002 mg/mL). These distances were used in all subsequent studies.

4.4.2.6. Light Isolation

To prove the utility of the Combination Imager for luminescence imaging, it was necessary to confirm its ability to provide total light isolation. The results of light leakage testing are shown in Figure 4.40.

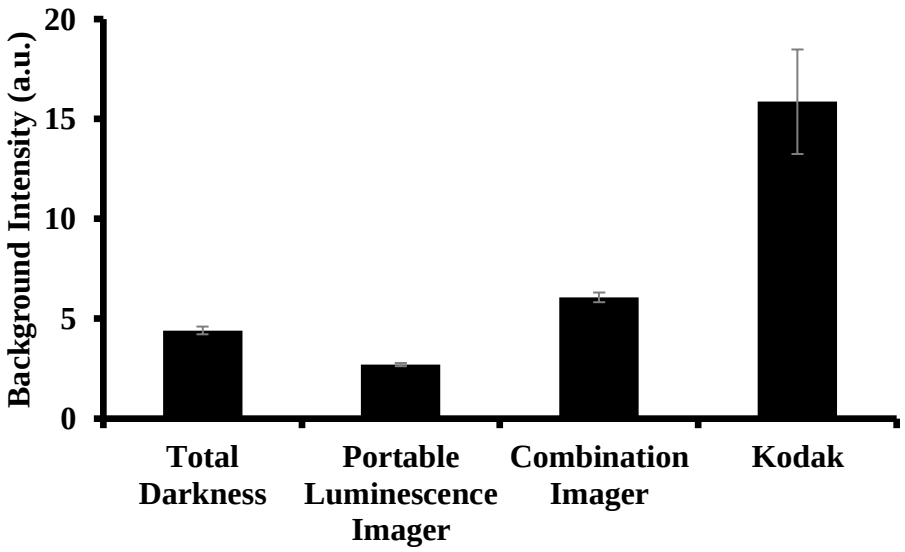

Figure 4.40. Imaging with the new luminescence imaging device was found to be statistically the same as imaging in total darkness, similar to the luminescence imager described in Chapter 3.

It was shown that the new Combination Imager is able to produce indistinguishable results from the dedicated luminescence imager, providing statistically identical results to imaging in darkness ($P = 0.17$). These results confirmed the utility of the Combination Imager for luminescence imaging studies.

4.4.3. In Vitro Studies

4.4.3.1. Beam Homogeneity Imager Comparison: 640 nm

The homogeneity and field of view of the Combination Imager at 18 cm was compared with the R4 imager and the Kodak at the 640 nm excitation wavelength. A continuous surface of NIR Cy5 dye solution was used. The results are shown in Figure 4.41.

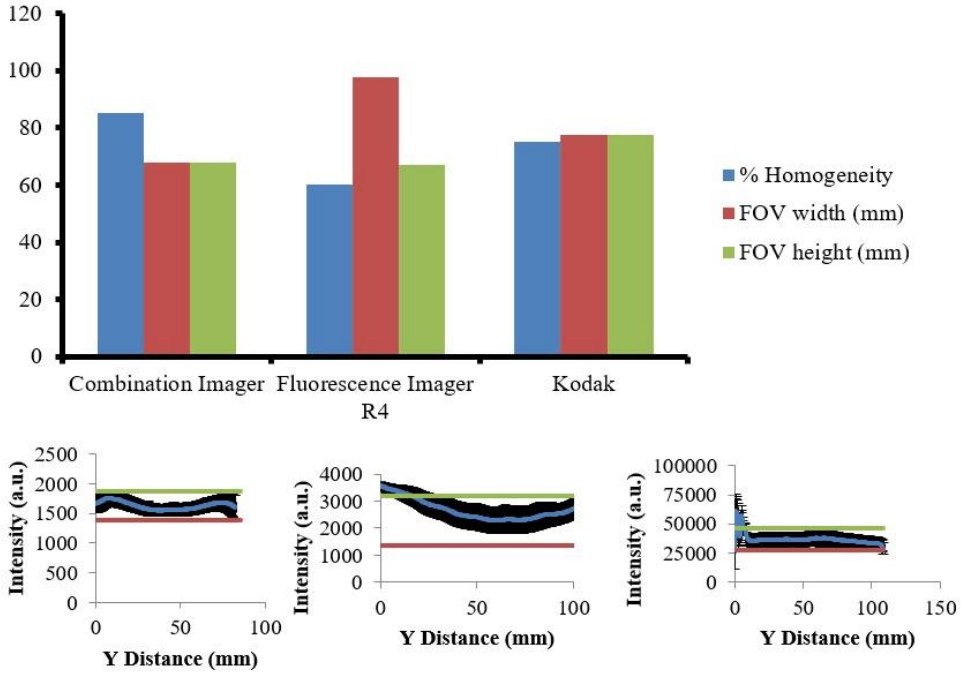

Figure 4.41. Field of view of the largest continuous area with the highest field of view for each imager is shown. Although the Kodak was found to have the highest homogeneous field of view, a homogeneity of only 75% could be achieved compared to the Combination Imager's 85%. The R4 imager was found to perform least favorably at only 60% homogeneity.

The Combination Imager was found to achieve the greatest homogeneity at 85% over a 70 x 70 mm FOV. Although the Kodak produced a wider homogeneous area of approximately 80 x 80 mm, it was only able to produce a

homogeneity of 75%. The R4 imager produced only 60% homogeneity in this study, contrasting with the results obtained with the power meter. This is likely due to the inability of the power meter to produce reliable continuous readings, due to hand placement and recording. This result displays the Combination Imager's high homogeneous view area at this wavelength, even compared to an industry standard imager.

4.4.3.2. Beam Homogeneity Imager Comparison: 470 nm

The homogeneity and field of view of the Combination Imager at 16 cm was compared with the R4 imager and the Kodak at 670 nm excitation (Figure 4.42).

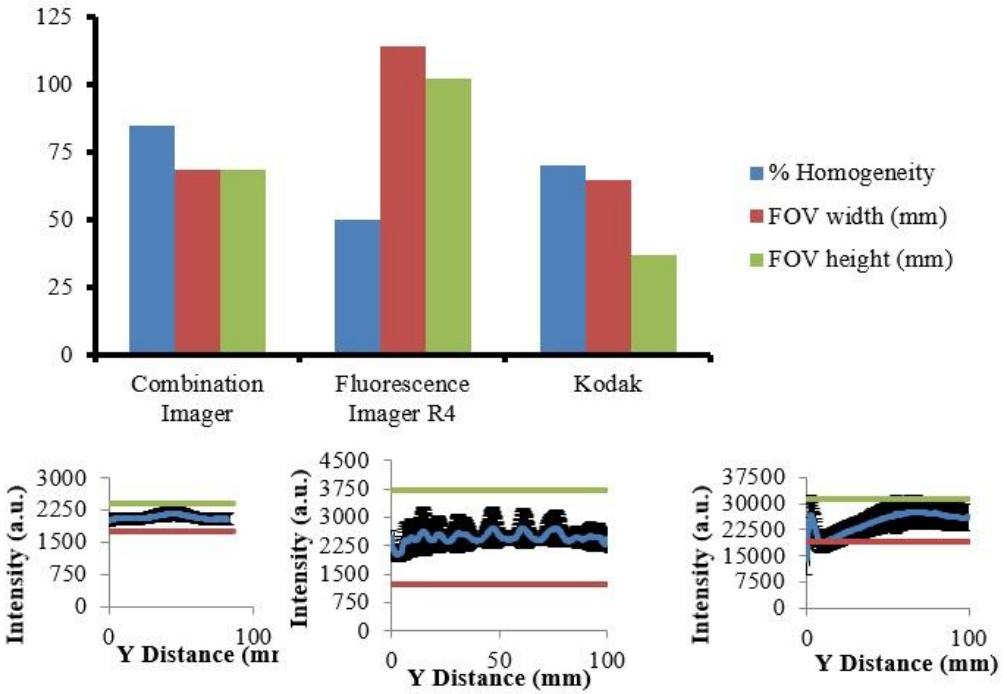

Figure 4.42. The largest with the highest homogeneity for each imager is shown. Although the R4 imager produced the highest homogeneous field of view, it was only 50% homogeneous compared to the Combination Imager's 85%. The Kodak produced a comparatively small field of view with a homogeneity of 70%.

For FITC as well as NIR Cy5, the Combination Imager displayed the highest homogeneity at 85% over a 70 x 70 mm FOV. Although the R4 imager produced a wider homogeneous area of approximately 120 x 110 mm, it was very inhomogeneous (50%) The intensity plot for this imager clearly shows the many peaks associated with hot-spot areas caused by direct LEDs. This is another reason for the false high reading of the power meter homogeneity study, as the detector of the power meter averages the intensity reading over several square mm and is less suited to detect small variations. The Kodak produced the smallest FOV of 60 x 40 mm at a homogeneity of 70%. Combined with the NIR Cy5 results from the previous study, it was concluded that the Combination Imager has impressive uniformity compared with the Kodak and R4 imagers.

4.4.3.3. Fluorescence Limit of Detection and Sensitivity Imager Comparison: Cy5

The sensitivity and limit of detection of the Combination Imager at 18 cm in a NIR Cy5 calibration curve study was compared to the R4 imager and Kodak. The results of this study are shown in Figure 4.43.

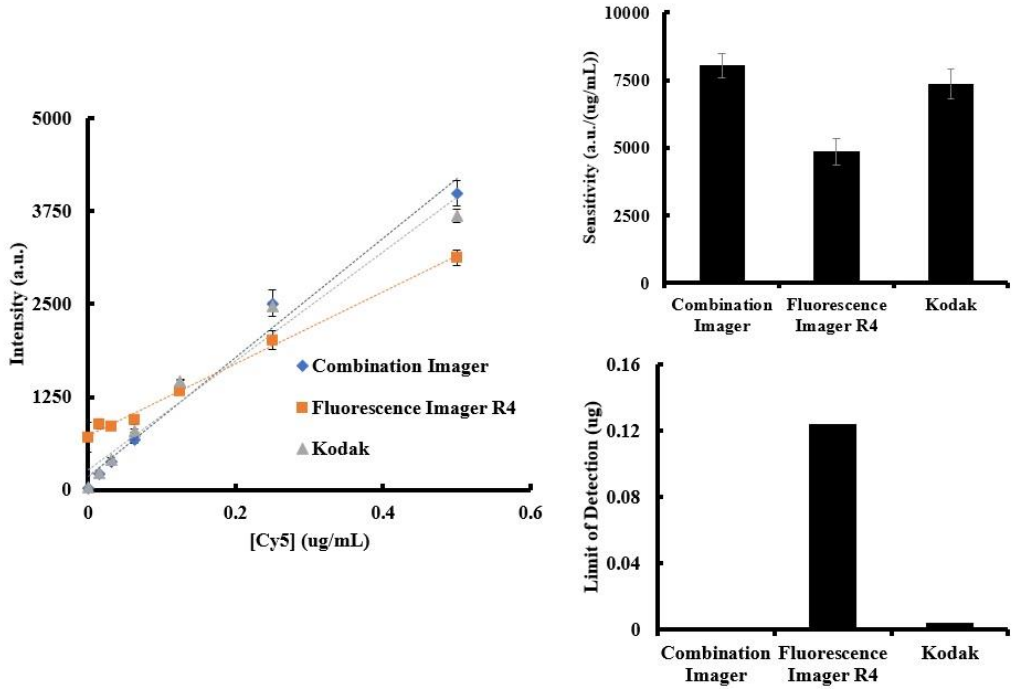

Figure 4.43. The sensitivity and limit of detection values in a NIR Cy5 calibration curve study were found to be statistically indistinguishable for the Combination Imager and the Kodak, with both devices outperforming the R4 imager.

With the Kodak scaled to 12-bit values, the sensitivities of the imagers were calculated as 8040.5 ± 91.3 $\frac{a.u.}{\mu g/_{mL}}$ for the Combination Imager, 4854.3 ± 351.4 $\frac{a.u.}{\mu g/_{mL}}$ for the R4 imager, and 7351.1 ± 228 $\frac{a.u.}{\mu g/_{mL}}$ for the Kodak. These results show that the Combination Imager can produce statistically equivalent sensitivity results *in vitro* to the Kodak for NIR Cy5 (P = 0.86) and higher sensitivity than the R4 imager.

The two devices were also found to have similar limits of detection, with the portable imager able to detect NIR Cy5 concentrations up to 0.0015 μM

compared to the Kodak's 0.0043 μM. These results support that both imagers are capable of measuring and quantifying fluorescent intensities *in vitro*.

4.4.3.4. Fluorescence Limit of Detection and Sensitivity Imager Comparison: FITC

The sensitivity and limit of detection of the Combination Imager at 18 cm in a NIR Cy5 calibration curve study was compared to the R4 imager and Kodak. The results of this study are shown in Figure 4.44.

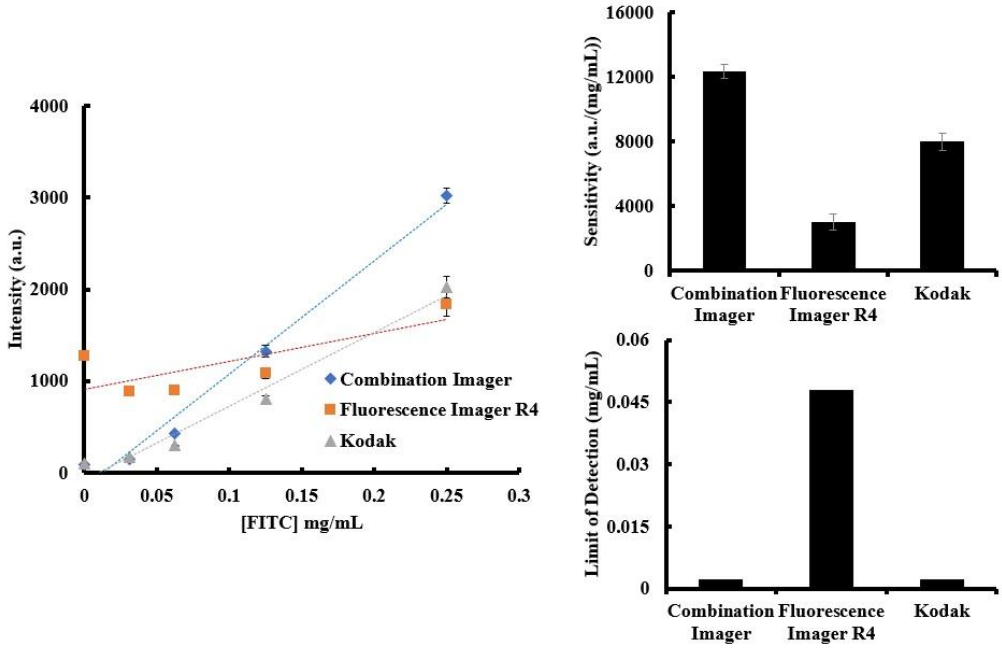

Figure 4.44. The sensitivity and limit of detection values in a FITC calibration curve study were found to be statistically indistinguishable for the Combination Imager and the Kodak, with both devices outperforming the R4 imager.

With the Kodak scaled to 12-bit values for comparison with the Combination and R4 imagers, the sensitivities of the imagers were determined to be 12337 ± 438.8 $\frac{a.u.}{mg/mL}$ for the Combination Imager, 4266.9 ± 502.4 $\frac{a.u.}{mg/mL}$ for

the R4 imager, and 7998.9 ± 541.35 $\frac{a.u.}{mg/mL}$ for the Kodak. These results display the ability of the Combination Imager to produce statistically equivalent sensitivity results *in vitro* to the Kodak for NIR Cy5 (P = 0.15) and higher sensitivity values than the R4 imager for this wavelength.

The two devices were also found to have similar limits of detection, with both imagers able to detect FITC concentrations as low as 0.0022 mg/mL FITC. These results support that both imagers are capable of measuring and quantifying fluorescent intensities at this wavelength *in vitro*.

4.3.3.5. Luminescence Limit of Detection and Sensitivity Imager Comparison

The sensitivity and limit of detection of the Combination Imager at 12 cm for a luminescent L-012 luminescence calibration curve was compared to the Kodak imager to determine the Combination Imager's suitability for luminescence studies. The results of this study are shown in Figure 4.45.

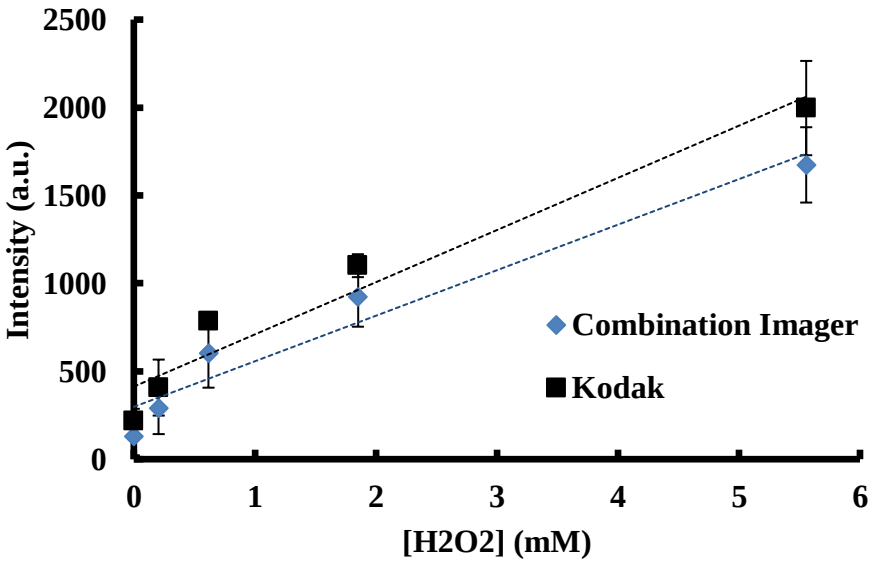

Figure 4.45. The sensitivity and limit of detection values in a luminescent L-012 luminescence calibration curve study were found to be statistically similar for the Combination Imager and the Kodak, with similar sensitivities and limits of detection.

With the Kodak scaled to 12-bit values for comparison with the Combination and R4 imagers, the sensitivities of the imagers were determined to be 259 ± 17.6 $\frac{a.u.}{mM}$ for the Combination Imager and 296 ± 26.9 $\frac{a.u.}{mM}$for the Kodak. These results show that the Combination Imager is able to produce statistically equivalent luminescent sensitivity results *in vitro* to the Kodak for NIR Cy5 (P = 0.072).

The two devices were also found to have similar limits of detection, with the limit of detection of the Combination Imager determined to be 1.2 mM compared to 0.47 mM ROS. These results support that both imagers are capable of measuring and quantifying luminescence.

4.5. Discussion

The work described here shows the development of the tabletop optical imager developed in Chapter 2 through several revisions into Revision 4, a device that adds significant functionality when compared with the initial revision. In the first revision (R2), increased z-axis adjustability was added. The excitation light source was also mounted to the exterior of the device to allow for dual-wavelength studies. The design was also made less restrictive by swapping the 4-legged design for a single stand. Finally, bulky drivers were incorporated under the imaging stage for enhanced portability. However, the retention of the LED ring used in R1 continued to limit the size of the field of uniform illumination as well as the working distance of the device. It was also desirable to overhaul the physical size of the device to make it more portable and conducive to large animal and human imaging.

The second revision (R3) made substantial optical improvements to the device. The LED ring was exchanged for a larger, more intense LED matrix, which increased the field of illumination. The filter wheel was also exchanged for a bandpass filter holder that held only one filter but interfaced directly with the LED matrix so excitation light sources and emission filters could be paired for ease of dual-wavelength excitation studies. However, this device featured a clunky LED matrix exchange mechanism and had limited z-axis adjustability.

Revision 4 of the fluorescence imaging device addressed many of the shortcomings of the previous imagers. Most notably, the device featured a more

robust LED matrix exchange mechanism. It was also designed to be mounted on an articulating arm to allow for full adjustability of position, which provided enhanced utility for large animal imaging scenarios. This revision of the device was also found to have significant room for improvement, however, as it was found to have high background during fluorescence studies. This limited both the sensitivity and limit of detection of the device. It was determined that a new excitation light strategy was necessary. Another imaging barrier inherent to this design was the lack of total light isolation to allow for luminescence imaging. To add this functionality, a total overhaul of the device was necessary.

The final imaging device developed in this work, the Combination Imager, successfully addressed these shortcomings and combined robust fluorescence and luminescence functionality. It utilized a complex system of optical filters mounted in a sophisticated imaging chamber. Swappable bases of different heights allow the distance between the camera and objective to be easily adjusted. A highly uniform, diffuse light source was mounted perpendicular to the imaging objective and reflected onto the sample using this filter system. Combined, these optical components successfully reduced the fluorescent background of the device to levels indistinguishable from the Kodak imager. In addition, light isolation strategies used to design the dedicated luminescence imager in Chapter 3 were applied to totally reduce light pollution by ambient light during the imaging process, allowing the device to be successfully utilized in luminescence imaging

studies. Most critically, the device has an open-bottomed design that opens the possibility of imaging in large animals and in clinical settings.

When compared with the Kodak imager, the Combination Imager shows equivalent performance in almost all areas. The light source of the Combination imager was determined to be 10-20 times more intense, allowing for shorter exposure times. This is especially critical in animal and clinical imaging. Animals can only be sedated for imaging for limited lengths of time. In human imaging scenarios, long immobilization sessions can be uncomfortably restrictive and small movements can impede image quality.

Beam uniformity for the Combination Imager was also found to rival that of the Kodak. The Combination Imager was found to produce beams of comparable size to the Kodak for all wavelengths with 10-15% higher uniformity.

Fluorescence and luminescence sensitivity were also significantly increased from the R1 design. When Kodak data was normalized from 16- to 12-bit, the Combination Imager performed statistically indistinguishably from the Kodak on these fronts in all wavelengths studied as well as in luminescence imaging scenarios.

Despite these encouraging results, the Kodak still holds several advantages that represent areas of improvement for the Combination Imager. One of the biggest advantages of the Kodak imager is its wide maximum field of view (up to 19 x 19 cm). Although the Kodak does not produce uniform light over this entire

area, it would be possible to scale the Combination Imager up to image areas that rival this surface area.

Additionally, the “turnkey” nature of the Kodak imager makes it an attractive system. Integrated software makes it easy for an operator with minimal training to select excitation and emission wavelengths automatically and acquire images. In the future, adding more of these automated features to the Combination Imager could increase its ease of use.

Finally, the use of a CCD capable of producing true 16-bit values also gives the Kodak an advantage due to the wider range of gray values that can be captured. Although data scaling used to compare the two devices displayed that they produce equivalent results when data is normalized to the Combination Imager’s 12-bit value range, it would be beneficial to acquire a camera with a similar bit depth for more direct comparison and even increased performance.

Taken together, the culmination of the work described in this chapter is a first-of-its-kind combination luminescence and fluorescence imaging device. Similar to the dedicated luminescence imager developed in Chapter 3, this imager has the capacity to collect new sets of biological data in large animal and potential clinical studies. The versatility and high optical performance of this device could make it useful both as a tool to gather preliminary information in large animal studies about various pathologies, including wound healing, infection, and cutaneous inflammation. In clinical applications, this device has potential

applications as a powerful diagnosis tool for these and additional disease states. Due to its high portability, versatile nature, and low cost, this device has especially strong potential in underserved imaging areas, including battlefield imaging and imaging in rural clinics.

Chapter 5. Future Directions

5.1. Summary of Work

Medical imaging is a broad field used to diagnose and monitor a wide range of pathologies in a clinical setting. Optical imaging is a particularly promising imaging modality, encompassing such techniques as fluorescence and luminescence imaging. These techniques have a number of important advantages applicable to clinical imaging applications, including their capacity to gather molecular-level information and collect data in real time.[101] These characteristics have the potential to improve patient quality of life and reduce treatment costs. A battery of fluorescent and luminescent probes capable of detecting markers of various disease states have also been developed to take advantage of these modalities.

Despite these advantages, fluorescence and luminescence imagers have seen limited application in clinical settings. There are several reasons for this, including several inherent challenges to applying these techniques in a clinical scenario. A critical barrier to clinical use of these modalities is a lack of robust, versatile imaging devices capable of imaging these signals in a clinical environment due to the unique requirements of these devices. Notable challenges include portability and isolation from ambient light.[102] Many devices are also restricted to a narrow range of wavelengths, narrowing their range of application to different probes.[101]

The work described here showcases the development of new optical imaging devices with the potential to overcome many of these challenges. The initial portion of this work focused on the development of a tabletop device capable of fluorescence and limited luminescence imaging. The utility of this device was measured through comparison with an industry-standard black box imager in a battery of *in vitro* studies. Its utility in *in vivo* imaging was also displayed in several small animal studies. Although the small field of view, inability to exchange wavelengths mid-study, and lack of light isolation limited its applicability to *in vitro* and small animal imaging, it was foundational to the devices developed later in this work.

The second device described here is a dedicated device for luminescence imaging. This versatile imager was designed specifically for imaging in large animal scenarios, with a variety of features tailored to this application. Unlike commercial black-box imaging devices that acquire luminescent signals by virtue of total enclosure of the subject, the luminescence imager has an open design that allows subjects of any size to be imaged without confinement. These included detachable bases for different view distances, as well as adjustable contours for imaging on organic surfaces of uneven heights. The device also featured an adjustable white light shutter to choose between white light and luminescence imaging settings. Most importantly, the device provided total isolation from ambient light during imaging, allowing even faint luminescent signals to be quantified even in lit procedure rooms. This imager was tested in a porcine wound

healing model and was able to gather new information about the relationship between wound healing, infection, vascularization, and ROS distribution. The results obtained with this device highlight the capability of the imagers here to gather new biomedical information in large animal models that has heretofore been inaccessible due to a lack of appropriate equipment and paved the way for the potential of future clinical trials.

The final device developed here was able to successfully combine the fluorescence and luminescence imaging functionality of the previous two devices into a robust combination fluorescence/luminescence imaging device capable of imaging both types of signals in large animal and potential human applications. The device combines the open design and full light isolation of the luminescence imager with all optical components necessary for fluorescence imaging with easy wavelength exchange. This device was validated in a wide range of critical functionality studies against a commercial *in vivo* imaging device, performing with comparable or improved performance in these areas. This device is the first described in literature capable of both multiwavelength fluorescence and luminescence imaging in large animals. Due to this, the work presented here represents the opportunity to apply a variety of fluorescent and luminescent probes in new large animal research applications as well as potential clinical uses.

5.2. Future Applications

The portable nature of the device developed here makes it a particularly good fit for several niche medical imaging applications. One notable application is

battlefield imaging. Many large imaging devices, such as MRI and CT devices, are impractical to maintain in field hospitals.[103] Due to this, any medical condition that requires imaging to diagnose must wait to be evaluated until the patient reaches a fully equipped medical facility, preventing the patient from receiving the best standard of care as early as possible. Several portable devices have been developed for different imaging modalities for this purpose. A handheld device has been developed for battlefield applications to diagnose and differentiate between hemorrhagic and ischemic stroke.[104] A subset of MRI imaging devices referred to as Ultra Low Field MRI (ULF-MRI) has recently been investigated due to its smaller size and increased safety when compared to conventional high-field MRI. Although the ULF-MRI has lower resolution than a traditional MRI, it has the capability to gather life-saving information about traumatic brain injury before a patient can reach a hospital. The portable imager developed in this work has the potential to fill this niche in medical imaging due to its portable nature, small size, ease of operation, and open, versatile design.

Medical imaging in rural areas is another area with the potential to benefit greatly from inexpensive, easy to use, portable imaging devices. Similar to the battlefield scenario described above, rural hospitals, especially those in third world countries, have limited access to the large and expensive imaging facilities common to a fully outfitted hospital. Unique solutions are in development to circumvent this and provide lifesaving diagnostic services. In rural India and China, retinopathy of prematurity (ROP) is a common cause of infant blindness.

When diagnosed promptly, ROP blindness is almost always preventable, but the lack of accessible ocular imaging screening services prevents diagnosis for many individuals. Telemedicine has been investigated as a way to combat this phenomenon, with teams of operators dispatched to at-risk communities in mobile treatment facilities.[105] Images are acquired and uploaded to a server for remote analysis by a physician. The device described in this work presents a strong fit for such a deployment scenario and could be used to acquire a wide range of biological information using fluorescence and luminescence.

5.3. Final Conclusions

In summary, there is an outstanding need for portable, versatile imaging devices to take advantage of promising new developments in the field of fluorescence and luminescence imaging. The work presented here describes the development and testing of a promising new optical imaging device with the ability to perform optical imaging using these techniques in large animal and clinical imaging scenarios. The first iteration of this device (Generation 1) was developed to perform tabletop imaging in *in vitro* and small animal *in vivo* studies. Its design included several key optical components, including a LED ring excitation light source, several emission filters contained in a rotatable filter wheel, and a CCD camera, integrated into a polycarbonate “black box” case. The design of this device considered several goals developed to differentiate this device from commercially available optical imaging devices. These goals included portability, an open and unenclosed design, both fluorescence and luminescence

functionality, and the ability to easily image at multiple wavelengths. This imaging device was found to perform competitively with a commercial *in vivo* imaging device in both fluorescence and luminescence *in vitro* studies. Additionally, the Generation 1 device was found to perform well in several small animal *in vivo* studies. However, it was determined that additional improvements to the device could add a wider range of functionality. First, the size and weight of the device needed to be reduced for easier handheld operation. Dual wavelength fluorescence functionality also needed to be enhanced due to the need to partially disassemble the device to change excitation wavelengths. Finally, the device required complete darkness to image luminescence. To allow the device to image luminescence in a realistic large animal or clinical scenario, the primary goal for the Generation 2 design was an open design combined with complete ambient light isolation.

The second version of this device was designed to image luminescence in large animal applications. This imager included a CCD and lens mounted on a complex imaging chamber. This 3D printed design included a manually switchable white light portal, modular bases that could be easily swapped for imaging at different distances and flat or contoured surfaces, and versatile mounting solutions to allow it to be operated by hand or attachment to an articulating arm. The inclusion of light-isolating foam gaskets at interfaces where light could enter the chamber also allowed the interior of the device to be completely free from ambient light, even when imaging in a lit procedure room.

This device was found to be capable of imaging luminescence in practical large animal imaging scenarios in *in vitro* studies simulating large animal use with curved imaging stages. In combination with a new luminescent ROS-sensing film, the device was also capable of characterizing luminescent signals in small animals. Finally, application of this device in a large animal luminescence imaging study allowed the collection of new information about wound healing and paved the way for future clinical applications. This device represented several improvements over both the Generation 1 design and commercial imagers, such as an open, portable design and the ability to quantify luminescent signals in large animals. However, fluorescence imaging capability was not integrated into this design. The final goal of this work was to combine the fluorescence functionality of the Generation 1 imaging device with the portability and large animal imaging capability of the luminescence imaging device.

The final imaging device developed here was a combination fluorescence and luminescence imaging device intended for use in large animal or clinical applications. This device combined key elements of the previous two designs with substantial improvements. Instead of including a LED ring as the excitation light source, a diffuse LED matrix was utilized. This matrix was mounted on the exterior of the device for easy exchange. Light from this matrix was focused onto the sample using a custom filter cube seating several excitation light filters at different angles as well as a bandpass emission filter. This filter cube design allowed wavelengths to be easily exchanged without adding additional bulk. The

light isolation strategy utilized in the luminescence imager was adapted for use with the final combination imager, including its light-isolating gaskets and detachable bases. Key components of the functionality of this device were validated and compared with a commercial device *in vitro*, such as light uniformity, optimal working distance, and fluorescence and luminescence sensitivity and limit of detection. The device was found to have competitive functionality in these tests, paving the way for future clinical applications.

In summary, the results of this work suggest that this device has the potential to collect new information about a wide range of pathologies in future work involving large animal and clinical applications.

References

1. Rasmussen JC, Aldrich MB, Tan IC, et al. Lymphatic transport in patients with chronic venous insufficiency and venous leg ulcers following sequential pneumatic compression. J Vasc Surg Venous Lymphat Disord. 2016;4(1):9-17.

2. Ntziachristos V, Bremer C, Weissleder R. Fluorescence imaging with near-infrared light: new technological advances that enable in vivo molecular imaging. Eur Radiol. 2003;13(1):195-208.

3. Ash C, Dubec M, Donne K, Bashford T. Effect of wavelength and beam width on penetration in light-tissue interaction using computational methods. Lasers Med Sci. 2017;32(8):1909-1918.

4. Shang Y, Zhao Y, Cheng R, Dong L, Irwin D, Yu G. Portable optical tissue flow oximeter based on diffuse correlation spectroscopy. Opt Lett. 2009;34(22):3556-3558.

5. Chinen AB, Guan CM, Ferrer JR, Barnaby SN, Merkel TJ, Mirkin CA. Nanoparticle Probes for the Detection of Cancer Biomarkers, Cells, and Tissues by Fluorescence. Chem Rev. 2015;115(19):10530-10574.

6. Hu C, Yong X, Li C, et al. CXCL12/CXCR4 axis promotes mesenchymal stem cell mobilization to burn wounds and contributes to wound repair. J Surg Res. 2013;183(1):427-434.

7. Weingarten MS, Samuels JA, Neidrauer M, et al. Diffuse near-infrared spectroscopy prediction of healing in diabetic foot ulcers: A human study and cost analysis. Wound Repair Regen. 2012;20(6):911-917.

8. Godavarty A, Khandavilli Y, Jung Y-J, Rao PNS. Non-contact optical imaging of healing and non-healing diabetic foot ulcers. 2015;931802(March 2015):931802.

9. Liu WF, Ma M, Bratlie KM, Dang TT, Langer R, Anderson DG. Real-time in vivo detection of biomaterial-induced reactive oxygen species. Biomaterials. 2011;32(7):1796-1801.

10. Schäferling M, Grögel DBM, Schreml S. Luminescent probes for detection and imaging of hydrogen peroxide. Microchim Acta. 2011;174(1-2):1-18.

11. Tseng JC, Kung AL. In vivo imaging of inflammatory phagocytes. Chem Biol. 2012;19(9):1199-1209.

12. Zhou J, Tsai Y-T, Weng H, Tang L. Noninvasive assessment of localized inflammatory responses. Free Radic Biol Med. 2012;52(1):218–226.

13. Peng Z, Zhou J, Dacy A, et al. Design of a portable imager for near-infrared visualization of cutaneous wounds. J Biomed Opt. 2017;22(1):016010.

14. Song C, Ye Z, Wang G, Yuan J, Guan Y. A lanthanide-complex-based ratiometric luminescent probe specific for peroxynitrite. Chem - A Eur J.

2010;16(22):6464-6472.

15. Schreml S, Meier RJ, Wolfbeis OS, Landthaler M, Szeimies R. 2D luminescence imaging of pH in vivo. Pnas. 2010;108(6):2432-2437.

16. Kielland A, Blom T, Nandakumar KS, Holmdahl R, Blomhoff R, Carlsen H. In vivo imaging of reactive oxygen and nitrogen species in inflammation using the luminescent probe L-012. Free Radic Biol Med. 2009;47(6):760-766.

17. Oh EJ, Lee HW, Kalimuthu S, et al. In vivo migration of mesenchymal stem cells to burn injury sites and their therapeutic effects in a living mouse model. J Control Release. 2018;279(April):79-88.

18. Meier RJ, Schreml S, Wang XD, Landthaler M, Babilas P, Wolfbeis OS. Simultaneous photographing of oxygen and pH in vivo using sensor films. Angew Chemie - Int Ed. 2011;50(46):10893-10896.

19. Zhou J, Tsai YT, Weng H, et al. Real-time detection of implant-associated neutrophil responses using a formyl peptide receptor-targeting NIR nanoprobe. Int J Nanomedicine. 2012;7:2057-2068.

20. Schreml S, Meier RJ, Wolfbeis OS, et al. 2D luminescence imaging of physiological wound oxygenation. Exp Dermatol. 2011;20(7):550-554.

21. Jawhara S, Mordon S. Monitoring of bactericidal action of laser by in vivo imaging of bioluminescent E. coli in a cutaneous wound infection. Lasers

Med Sci. 2006;21(3):153-159.

22. Papazoglou ES, Zubkov L, Mao X, Neidrauer M, Rannou N, Weingarten MS. Image analysis of chronic wounds for determining the surface area. Wound Repair Regen. 2010;18(4):349-358.

23. Galiano RD, Michaels V J, Dobryansky M, Levine JP, Gurtner GC. Quantitative and reproducible murine model of excisional wound healing. Wound Repair Regen. 2004;12(4):485-492.

24. Dunnill C, Patton T, Brennan J, et al. Reactive oxygen species (ROS) and wound healing: the functional role of ROS and emerging ROS-modulating technologies for augmentation of the healing process. Int Wound J. 2017;14(1):89-96.

25. Parks WC, Wilson CL, López-Boado YS. Matrix metalloproteinases as modulators of inflammation and innate immunity. Nat Rev Immunol. 2004;4(8):617-629.

26. Saito O, Furuhata H. Improving uniformity of intensity distribution of ultrasound passing through a human-skull fragment by random modulation. Int J Clin Neurosci Ment Heal. 2014.

27. Peng Z, Zhou J, Dacy A, et al. Design of a portable imager for near-infrared visualization of cutaneous wounds. J Biomed Opt. 2017;22(1):016010.

28. Dacy A, Nowmi H, Davis K, Hu W, Tang L. Design and Evaluation of an Imager for Assessing Wound Inflammatory Responses and Bioburden in a Pig Model. J Biomed Opt. 2019 (In Revision).

29. Sen CK, Gordillo GM, Roy S, et al. Human Skin Wounds: A Major Snoballing Threat to Public Health and Economy. Wound Repair Regen. 2010;17(6):763-771.

30. Brem H, Stojadinovic O, Diegelmann RF, et al. Cholinergic Anti-Inflammatory Pathway Activity and High High Mobility Group Box-1 (HMGB1) Serum Levels in Patients with Rheumatoid Arthritis. Mol Med. 2007;13(9):30-39.

31. Schäfer M, Werner S. Oxidative stress in normal and impaired wound repair. Pharmacol Res. 2008;58(2):165-171.

32. Kurahashi T, Fujii J. Roles of Antioxidative Enzymes in Wound Healing. J Dev Biol. 2015;3(2):57-70.

33. Roy S, Khanna S, Nallu K, Hunt T, Sen C. Dermal wound healing is subject to redox control. Mol Ther. 2006;13(1):211–220.

34. Mukherjee R, Tewary S, Routray A. Diagnostic and Prognostic Utility of Non-Invasive Multimodal Imaging in Chronic Wound Monitoring: a Systematic Review. J Med Syst. 2017;41(3).

35. Albouy B, Lucas Y, Treuillet S. 3D Modeling from uncalibrated color

images for a complete wound assessment tool. Annu Int Conf IEEE Eng Med Biol - Proc. 2007;29(1):3323-3326.

36. Christian LM, Graham E, Padgett DA. Stress and Wound Healing. Neuroimmunomodulation. 2007;13(1):337-346.

37. Davis K, Bills J, Barker J, Kim P, Lavery L. Simultaneous irrigation and negative pressure wound therapy enhances wound healing and reduces wound bioburden in a porcine model. Wound Repair Regen. 2013;21(6):869-875.

38. Serena TE, Hanft JR, Facfas DPM, Snyder R. Examination in the Diagnosis of Wound Infection : Preliminary Communication. Int J Low Extrem Wounds. 2008;7(1):32-35.

39. Pal A, Goswami D, Cuellar HE, Castro B, Kuang S, Martinez R V. Early detection and monitoring of chronic wounds using low-cost, omniphobic paper-based smart bandages. Biosens Bioelectron. 2018;117(July):696-705.

40. Dargaville TR, Farrugia BL, Broadbent JA, Pace S, Upton Z, Voelcker NH. Sensors and imaging for wound healing: A review. Biosens Bioelectron. 2013;41(1):30-42.

41. Treuillet S, Albouy B, Lucas Y. Three-dimensional assessment of skin wounds using a standard digital camera. IEEE Trans Med Imaging. 2009;28(5):752-762.

42. Barone S, Paoli A, Razionale A V. Assessment of chronic wounds by three-dimensional optical imaging based on integrating geometrical, chromatic, and thermal data. Proc Inst Mech Eng Part H J Eng Med. 2011;225(2):181-193.

43. Hoeksema H, Van de Sijpe K, Tondu T, et al. Accuracy of early burn depth assessment by laser Doppler imaging on different days post burn. Burns. 2009;35(1):36-45.

44. Yu CO-L, Leung K-S, Fung K-P, et al. The characterization of a full-thickness excision open foot wound model in n5-streptozotocin (STZ)-induced type 2 diabetic rats that mimics diabetic foot ulcer in terms of reduced blood circulation, higher C-reactive protein, elevated inflammation, and re. Exp Anim. 2017;66(3):259-269.

45. Wahabzada M, Besser M, Khosravani M, et al. Monitoring wound healing in a 3D wound model by hyperspectral imaging and efficient clustering. PLoS One. 2017;12(12):1-14.

46. Nouvong A, Hoogwerf B, Mohler E, Davis B, Tajaddini A, Medenilla E. Evaluation of Diabetic Foot Ulcer Healing With Hyperspectral Imaging of Oxyhemoglobin and Deoxyhemoglobin. Diabetes Care. 2009;32(11).

47. Yudovsky D, Nouvong A, Pilon L. Hyperspectral imaging in diabetic foot wound care. J diabetes Sci Technol. 2010;4(5):1099-1113.

48. Smith LE, Bonesi M, Smallwood R, Matcher SJ, MacNeil S. Using swept-source optical coherence tomography to monitor the formation of neo-epidermis in tissue-engineered skin. J Tissue Eng Regen Med. 2010.

49. Zhong H, Zeng C, Guo Z, et al. Using Optical Coherence Tomography to Monitor Process of Wound Healing: a Preliminary Study. 2006 Int Symp Biophotonics, Nanophotonics Metamaterials. 2006:84-87.

50. Ramane D, Shaligram A. Optimization of multi-element LED source for uniform illumination of plane surface. Opt Express. 2011;19(S4):A639.

51. Miyajima K, Kon H, Arakawa T, Shiba K, Mitsubayashi K. Fluoroimmunoassay System for Fiber-Optic Measurement of House Dust Mite Allergen (Der f1). Sensors Mater. 2015;27(9):871-880.

52. Qiao Z, Zhang H, Wang KW, Zhang Y. A highly sensitive and responsive fluorescent probe based on 6-azide-chroman dye for detection and imaging of hydrogen sulfide in cells. Talanta. 2019;195(November 2018):850-856.

53. Qiu B, Guo L, Wang W, Chen G. Synthesis of a novel fluorescent probe useful for DNA detection. Biosens Bioelectron. 2007;22(11):2629-2635.

54. Long W, Lu YJ, Zhang K, et al. Boosting the turn-on fluorescent signaling ability of thiazole orange dyes: The effectiveness of structural modification site and its unusual interaction behavior with nucleic acids. Dye Pigment. 2018;159(July):449-456.

55. Vidakovic B. Statistics for Bioengineering Sciences. 2011.

56. Melcher RLJ, Moerschbacher BM. An improved microtiter plate assay to monitor the oxidative burst in monocot and dicot plant cell suspension cultures. Plant Methods. 2016;12(1):1-11.

57. Kearney V, Huang Y, Mao W, Yuan B, Tang L. Canny edge-based deformable image registration. Phys Med Biol. 2017;62(3):966-985.

58. Lachin JM. Introduction to sample size determination and power analysis for clinical trials. Control Clin Trials. 1981;2(2):93-113.

59. Tanaka A, Yamane Y, Matsuda H. Mast cell MMP-9 production enhanced by bacterial lipopolysaccharide. J Vet Med Sci. 2001;63(7):811.

60. Xie B, Dong Z, Fidler IJ. Regulatory mechanisms for the expression of type IV collagenases/gelatinases in murine macrophages. J Immunol. 1994;152(7):3637-3644.

61. Nauta A, Seidel C, Deveza L, et al. Adipose-derived stromal cells overexpressing vascular endothelial growth factor accelerate mouse excisional wound healing. Mol Ther. 2013;21(2):445-455.

62. Zhou J, Weng H, Huang Y, Gu Y, Tang L, Hu W. Ratiometric reactive oxygen species nanoprobe for noninvasive in vivo imaging of subcutaneous inflammation/infection. J Biomed Nanotechnol. 2017;12(8):1679-1687.

63. Galli SJ, Maurer M, Lantz CS. Mast cells as sentinels of innate immunity. Curr Opin Immunol. 1999;11(1):53-59.

64. Zhou J, Tsai Y-T, Weng H, Baker D, Tang L. Real time monitoring of biomaterial-mediated inflammatory responses via macrophage-targeting NIR nanoprobes Jun. 2011;32(35):9383–9390.

65. Tang E, Nair A, Baker D, Hu W, Zhou J. In Vivo Imaging of Infection Using a Bacteria-Targeting Optical Nanoprobe. J Biomed Nanotechnol. 2014;10(5):856–863.

66. Schreml S, Meier RJ, Wolfbeis OS, Landthaler M, Szeimies R-M, Babilas P. 2D luminescence imaging of pH in vivo. Proc Natl Acad Sci U S A. 2011;108(6):2432-2437.

67. Madajewski B, Judy BF, Mouchli A, et al. Intraoperative near-infrared imaging of surgical wounds after tumor resections can detect residual disease. Clin Cancer Res. 2012;18(20):5741-5751.

68. Demaria M, Ohtani N, Youssef S, et al. An Essential Role for Senescent Cells in Optimal Wound Healing through Secretion of PDGF-AA. Dev Cell. 2015;31(6):722-733.

69. Godwin ZR, Bockhold JC, Webster L, Falwell S, Bomze L, Tran NK. Development of novel smart device based application for serial wound imaging and management. Burns. 2013;39(7):1395-1402.

70. Hofmann J, Meier RJ, Mahnke A, et al. Ratiometric luminescence 2D in vivo imaging and monitoring of mouse skin oxygenation. Methods Appl Fluoresc. 2013;1(4).

71. DaCosta RS, Kulbatski I, Lindvere-Teene L, et al. Point-of-care autofluorescence imaging for real-time sampling and treatment guidance of bioburden in chronic wounds: First-in-human results. PLoS One. 2015;10(3).

72. Autréaux BD, Toledano MB. ROS as signalling molecules: mechanisms that generate specificity in ROS homeostasis. Nat Rev. 2007;8(1).

73. Stone J, Collins T. The role of hydrogen peroxide in endothelial proliferative responses. Endothelium. 2002;9(4):231.

74. Murrell GAC, Martin J, Bromley L. Modulation of fibroblast proliferation by free radicals. Biochem J. 1990;265(1):659-665.

75. Benson BL, Li L, Myers JT, et al. Biomimetic post-capillary venule expansions for leukocyte adhesion studies. Sci Rep. 2018;8(1):1-15.

76. Robson MC, Steed DL, Franz MG. Wound healing: Biologic features and approaches to maximize healing trajectories. Curr Probl Surg. 2001;38(2):A1.

77. Halliwell B. Reactive oxygen species in living systems: Source, biochemistry, and role in human disease. Am J Med. 1991;91(3C):14S-

22S.

78. Soneja A, Drews M, Malinski T. Role of nitric oxide, nitroxidative and oxidative stress in wound healing. Pharmacol Reports. 2005;57:108-119.

79. Diegelmann RF. Wound healing: an overview of acute, fibrotic and delayed healing. Front Biosci. 2004;9(1-3):283.

80. Dovi J V. Accelerated wound closure in neutrophil-depleted mice. J Leukoc Biol. 2003;73(4):448-455.

81. Frykberg RG, Banks J. Challenges in the Treatment of Chronic Wounds. Adv Wound Care. 2015;4(9):560-582.

82. Dhall S, Do DC, Garcia M, et al. Generating and reversing chronic wounds in diabetic mice by manipulating wound redox parameters. J Diabetes Res. 2014;2014:18.

83. Sen CK, Khanna S, Babior BM, Hunt TK, Christopher Ellison E, Roy S. Oxidant-induced vascular endothelial growth factor expression in human keratinocytes and cutaneous wound healing. J Biol Chem. 2002;277(36):33284-33290.

84. Taniyama Y, Griendling KK. Reactive Oxygen Species in the Vasculature: Molecular and Cellular Mechanisms. Hypertension. 2003;42:1075-1081.

85. Ushio-Fukai M, Nakamura Y. Reactive oxygen species and angiogenesis: NADPH oxidase as target for cancer therapy. Cancer Lett. 2008;266(1):37-

52.

86. Kim M-H, Liu W, Borjesson DL, et al. Dynamics of Neutrophil Infiltration during Cutaneous Wound Healing and Infection Using Fluorescence Imaging. J Invest Dermatol. 2008;128(7):1812-1820.

87. Velnar T, Bailey T, Smrkolj V. The wound healing process: an overview of the cellular and molecular mechanisms. J Int Med Res. 2009;37(5):1528-1542.

88. Peng Z, Zhou J, Dacy A, et al. Design of a portable imager for near-infrared visualization of cutaneous wounds. J Biomed Opt. 2017;22(1).

89. Zielonka J, Lambeth JD, Kalyanaraman B, Lambeth D, Kalyanaraman B. On the use of L-012, a luminol-based chemiluminescent probe, for detecting superoxide and identifying inhibitors of NADPH oxidase: A reevaluation. Free Radic Biol Med. 2013;65:1310-1314.

90. Singer AJ, McClain SA. Development of a porcine excisional wound model. Acad Emerg Med. 2003;10(10):1029-1033.

91. Wang JF, Olson ME, Reno CR, Wright JB, Hart DA. The pig as a model for excisional skin wound healing: characterization of the molecular and cellular biology, and bacteriology of the healing process. Comp Med. 2001;51(4):341-348.

92. Seaton M, Hocking A, Gibran NS. Porcine models of cutaneous wound

healing. ILAR J. 2015;56(1):127-138.

93. Whitlock MC. Combining probability from independent tests: The weighted Z-method is superior to Fisher's approach. J Evol Biol. 2005;18(5):1368-1373.

94. Li W, Dong K, Wang H, et al. Remote and reversible control of in vivo bacteria clustering by NIR-driven multivalent upconverting nanosystems. Biomaterials. 2019.

95. Razzell W, Evans IR, Martin P, Wood W. Calcium flashes orchestrate the wound inflammatory response through duox activation and hydrogen peroxide release. Curr Biol. 2013;23(5):424-429.

96. Kirketerp-Møller K, Jensen P, Fazli M, et al. Distribution, organization, and ecology of bacteria in chronic wounds. J Clin Microbiol. 2008;46(8):2717-2722.

97. Zielonka J, Lambeth JD, Kalyanaraman B. On the use of L-012, a luminol-based chemiluminescent probe, for detecting superoxide and identifying inhibitors of NADPH oxidase: A reevaluation. Free Radic Biol Med. 2013;65:1310-1314.

98. Zhu TC, Liu B, Penjweini R. Study of tissue oxygen supply rate in a macroscopic photodynamic therapy singlet oxygen model. J Biomed Opt. 2015;20(3):038001.

99. Magnan P. Detection of visible photons in CCD and CMOS: A comparative view. Nucl Instruments Methods Phys Res Sect A Accel Spectrometers, Detect Assoc Equip. 2003;504(1-3):199-212.

100. Murari K, Etienne-Cummings R, Thakor N V., Cauwenberghs G. A CMOS in-pixel CTIA high-sensitivity fluorescence imager. IEEE Trans Biomed Circuits Syst. 2011;5(5):449-458.

101. DSouza A V., Lin H, Henderson ER, Samkoe KS, Pogue BW. Review of fluorescence guided surgery systems: identification of key performance capabilities beyond indocyanine green imaging. J Biomed Opt. 2016;21(8):080901.

102. van Leeuwen FWB, Hardwick JCH, van Erkel AR. Luminescence-based Imaging Approaches in the Field of Interventional Molecular Imaging. Radiology. 2015;276(1):12-29.

103. Eadie LH. New technology and potential for telemedicine in battlefield brain injury diagnostics. Concussion. 2016;1(4):CNC22.

104. Persson M, Fhager A, Trefna HD, et al. Microwave-based stroke diagnosis making global prehospital thrombolytic treatment possible. IEEE Trans Biomed Eng. 2014;61(11):2806-2817.

105. Vinekar A, Jayadev C, Mangalesh S, Shetty B, Vidyasagar D. Role of tele-medicine in retinopathy of prematurity screening in rural outreach centers

in India - a report of 20,214 imaging sessions in the KIDROP program. Semin Fetal Neonatal Med. 2015;20(5):335-345.

Biographical Information

Ashley Christine Dacy received her bachelor's degree in chemical engineering from The University of Notre Dame in Fall of 2014. She enrolled directly in the BS-to-PhD program at The University of Texas at Arlington in the lab of Dr. Liping Tang. Working with this lab's talented team of scientists, Ashley performed research in several areas of tissue engineering and medical imaging. These projects included the development of a new drug eluting particle-based treatment for post-traumatic osteoarthritis, the design and manufacture of a subcutaneously implantable cancer trapping combination device, and the prototyping and testing of several new medical imaging devices for translational applications in wound healing and other pathologies. In a pre-clinical model of wound healing in swine, this device revealed new information about the relationship between reactive oxygen species, vascularization, and infection in wound healing, bringing to light several potential new markers clinicians could use to differentiate between infected and uninfected wounds. Ashley is relocating to San Antonio, TX after graduation and plans to pursue employment in industry as a research and development engineer designing and testing new medical devices.